HARP targets pion production cross section and yield measurements: Implications for MiniBooNE neutrino flux

A Dissertation Submitted to the

Graduate School

of the University of Cincinnati

in partial fulfillment of the

requirements for the degree of

Doctor of Philosophy

in the Department of Physic

of the College of Arts and Sciences

July 2015

by

Don Athula Abeyarathna Wickremasinghe

M.Sc., University of Cincinnati, 2011

M.Sc., Norwegian University of Science and Technology (NTNU), 2008

B.Sc., University of Peradeniya, 2002

Committee Chair: Professor Randy A. Johnson

HARP targets pion production cross section and yield measurements: Implications for MiniBooNE neutrino flux

Don Athula Abeyarathna Wickremasinghe

Abstract

The prediction of the muon neutrino flux from a 71.0 cm long beryllium target for the MiniBooNE experiment is based on a measured pion production cross section which was taken from a short beryllium target (2.0 cm thick - 5% nuclear interaction length) in the Hadron Production (HARP) experiment at CERN. To verify the extrapolation to our longer target, HARP also measured the pion production from 20.0 cm and 40.0 cm beryllium targets. The measured production yields, $d^2N^{\pi^\pm}(p,\theta)/dpd\Omega$, on targets of 50% and 100% nuclear interaction lengths in the kinematic rage of momentum from 0.75 GeV/c to 6.5 GeV/c and the range of angle from 30 mrad to 210 mrad are presented along with an update of the short target cross sections. The best fitted extended Sanford-Wang (SW) model parameterization for updated short beryllium target π^+ production cross section is presented. Yield measurements for all three targets are also compared with that from the Monte Carlo predictions in the MiniBooNE experiment for different SW parameterization. The comparisons of ν_μ flux predictions for updated SW model is presented.

Acknowledgement

I was very fortunate to have a wonderful advisor, Professor Randy Johnson, who showed me not only the way of scientific thinking but also the way of scientific writing. I appreciate your kind cooperation on my entire research project. Your great ideas and suggestions were very helpful for me to complete this HARP targets analysis. Thanks a lot for giving me this challenging HARP long target analysis problem as my Ph.D. research. I am proud to be one of your Ph.D. students. I appreciate your friendly and pleasant way of discussing research problems. I still remember the first day that I went to Fermilab with you. That was a wonderful excited day for me. Thank you for showing me all around the Fermilab site including buffalo (Bison) which is the famous attraction in the Fermilab. Thank you so much for showing me the right direction to complete this research project and also for correcting my entire thesis (except this section) with your kind patience on my bad mistakes. Truly, I am more than grateful to you for everything you provided me to succeed this thesis work.

I am very happy to thank Richard Van De Water, Rex Tayloe and all other MiniBooNE collaborators for your great encouragements, comments and ideas on my research project. I would like to thanks to David W. Schmitz (Dave) who gave me the first impressive introduction about the research work and also the countless training about HARP data analysis. Your suggestions and ideas on HARP data analysis were very beneficial to complete this thesis. Thank you again Dave!

I am very grateful to Zarko Pavlovic for his countless helps on MiniBooNE Monte Carlo simulation. Thank you so much for given me a very good knowledge about the function of beam Monte Carlo. I really appreciate your kind responds and great helps

on solving problems that I faced while accessing MiniBooNE machines, storing data and submitting condor jobs. Thank you so much Zarko for your friendly encouragements and impressive comments on my entire HARP analysis.

I cannot forget my Fermilab days that I worked with Denis Perevalov on CCQE proton fitter. You gave me a very impressive series of discussions on CCQE proton fitter. I am very lucky to meet you as a postdoc! I learnt a lot from you about fitting algorithms in FORTRAN that helped me to improve my programing skills a lot. I would like to thank you for given me all encouragements and advises on everything as a good friend. I cannot forget about the "Spike" problem in our proton fitter :)

It was great pleasure meeting Ranjan Dharmapalan, Joe Grange, Teppei Katori and Sam Zeller on the 10th floor at Fermilab. Thank you very much for keeping a nice friendship with me and for helping me on some sort of CCQE problems. Hey Ranjan thanks a lot for introducing me to other friends and also giving me a place to sit and work during my Fermilab visits. I enjoyed a lot having nice discussions with you all.

I cannot forget my beautiful Cincinnati and all my physics department professors who taught me physics to become a physicist. I would especially thanks to my research committee professors, Rohana Wijewardhana, Brian Meadows and Young Kim, for encouraging me to complete my thesis and also for keeping in touch with my research progress. I would like to extend my thanks to all Cincinnati Sri Lankan community especially UC grads who helped us a lot during our difficult times. We had a very nice companionship and that made us unforgettable memories during past six years.

I still remember my wonderful undergraduate days at the University of Peradeniya, Sri Lanaka. I am very grateful to all physics department teachers in the university of Peradeniya who taught me undergraduate physics to improve my academic career. I am not here to complete my Ph.D. thesis without having your kind cooperation. Thank you so much for everything !!! I would like to express my sincere gratitude to Dr. Upali Karunasiri who inspired all undergraduate students to apply for higher studies to achieve their own goals.

I would also like to thank my M.Sc. thesis advisor at NTNU, Prof. Kåre Olaussen,

who taught me the foundation of the theoretical physics. I was fortunate to learn from you the way that you approach to research problems as a theoretical physicist.

Finally, I would like extend my warm thanks and appreciations to Niranjala's mother and father for their kind and countless helps that supported directly and indirectly to succeed my thesis. It's a great pleasure to have such a wonderful time during their stays with us. I would like to thank my mother and my late father who gave me everything for my life in many many ways. I miss you so much in my life. And last, but not least, I am very much thankful to my wife Niranjala Wickremasinghe for encouraging me and helping me with a great mutual understanding to archive this thesis goal.

Contents

List of Figures

List of Tables

Part I

Introduction

Chapter 1

Overview of Neutrinos

1.1 A brief history of neutrinos

Insight into the mystery surrounding the neutral particle named “neutrino” began after the discovery of the radioactivity. In the year 1896, Henri Becquerel discovered the radioactivity from uranium salt. Then Pierre and Marie Curie discovered polonium and radium which is more radioactive than pure uranium. In 1899, Rutherford discovered that there were two types of emitting radiations, α and β. In 1900 Villard discovered the third type of radiation emitting from radium which he named as γ-rays. Later experiments on radioactivity showed that three types of radiations, α, β and γ could be recognized as ^{4}He, electron and photons respectively.

In 1914, James Chadwick showed that the energy spectrum of β is continuous and not discrete as the spectra of α and γ radiation. This surprising measurement led to postulate the existing of a new particle to conserve the energy of the process. In the year 1930, Wolfgang Pauli proposed [1] the existing of a neutral and weakly interacting fermion which is emited in the β decay process from the radioactive element. This proposed particle was named as “neutron" at first and then it was re-named as “neutrino” after discovering todays “neutron” by J.Chadwick in 1932. With the help of Pauli’s proposed particle, in 1934, Enrico Fermi proposed a theory for the β decay

process now called "Fermi Theory". This was the first theoretical description of weak interactions.

The possibility of detecting a neutrino was calculated by H. Bethe and R. Peierls [2] by using Fermi theory and the rate of of the beta decay in 1934. Since the calculated neutrino-matter interaction cross section, $\sigma < 10^{-44}$ cm^2, was very small, they claimed that neutrinos might never be observed. In 1936, the muon was discovered [3] by Seth Neddermeyer and Carl Anderson during the studies of cosmic particles at Caltech. In 1937, the existence of muon was further confirmed by J. C. Street and E. C. Stevenson in a cloud chamber experiment. In addition to that, the discovery of muon was helpful to extend the Fermi's weak interaction theory further. In 1935, H. Yukawa had theoretically predicted the existence of intermediate "mesons" as carrier particles which is responsible for nuclear strong forces. Initially, the muon was suggested as the Yukawa's predicted intermediate meson but later experiments showed that the muon was not involved for strong nuclear interactions. In 1947, the charged pion, the first meson, was discovered by the collaboration of C. Powell, C. Lattes, G Occhialini *et al.*, at the University of Bristol, England. In 1946, Pontecorvo suggested a radiochemical process to detect neutrino-matter interactions which is based on hitting a Chlorine nucleus with a neutrino. In this process, the Chlorine nucleus turns into an Argon nucleus by emitting an electron as,

$$\nu_e + {}^{37}\mathrm{Cl} \rightarrow {}^{37}\mathrm{Ar} + \mathrm{e}^-. \tag{1.1}$$

In 1956, Frederick Reines, Clyde Cowan and collaborators were able to show the first experimental observation [4] of neutrino[1]-matter interaction at the Savannah River Plant in South Carolina. This process was the inverse β decay process that turns a proton into a neutron as:

$$\bar{\nu}_e + p \rightarrow n + \mathrm{e}^+. \tag{1.2}$$

[1]Nuclear reactor has produced antineutrinos from the beta decay.

The first idea of neutrino mixing and oscillation was proposed by B. Pontecorvo [5] in 1957, soon after the discovery of the parity violation in β-decay (Wu, *et al.* [6]). His phenomenological idea was based on $K^0 \rightleftarrows \bar{K}^0$ oscillation. Since there were only one type of known neutrino (ν_e) in 1950s, he proposed the possibility of $\nu_e \rightleftarrows \bar{\nu}_e$ transition in vacuum. A few decades after the discovery of muon, in 1962, Leon M. Lederman, Melvin Schwartz and Jack Steinberger at Brookhaven National Laboratory (BNL) discovered [7] the second type of neutrino named as "muon neutrino", ν_μ. After discovering ν_μ, a new model of neutrino flavor mixing was proposed by Maki, Nakagawa and Sakata [8] in the same year. In 1968, Ray Davis [9] was able to detect solar neutrinos by using Pontecorvo suggested radiochemical process (Cl-Ar process) at Homestake Gold Mine in Lead, South Dakota. This measurement of the total number of solar neutrinos was only about 1/3 of the number predicted by Standard Solar Model (SSM) of J. Bahcall [10]. That discrepancy was called as "Solar Neutrino Problem". This discrepancy was confirmed by several high energy and low energy solar neutrino experiments.

After discovering tau (τ^-) particle [11], a third charged lepton, in 1975 by Martin Lewis Perl with his colleagues in the SLAC-LBL group, the existence of the another neutrino that associates with τ^- lepton was assumed. This third neutrino, ν_τ, was discovered [12] by the collaboration of DONUT (Direct Observation of NU Tau) experiment at Fermi National Accelerator Laboratory (FNAL) in 2000. The "Solar Neutrino Problem" has been resolved after discovering three flavor neutrinos and also understanding their propagation through the space. A theoretical framework to explain this problem was developed by Mikheyev-Smirnov-Wolfenstein known as "MSW effect" [13, 14, 15] which takes account the propagation of neutrinos through the dense solar matter.

1.2 Neutrinos in the Standard Model

1.2.1 Standard Model overview

The Standard Model (SM) [16, 17, 18] describes the fundamental building blocks of known matter. Their interactions governed by forces: the strong, the electromagnetic (EM) or the weak. The mathematical framework for the SM is provided by Quantum Field Theory (QFT).

According to the Standard Model, the fundamental building blocks can be divided into two types of elementary fermions (spin 1/2): quarks and leptons. This model contains six types of known flavor quarks, six types of leptons and four types of force carrier bosons (spin = 1) as shown in the Fig. 1.1. In the SM model, u,c and t quarks

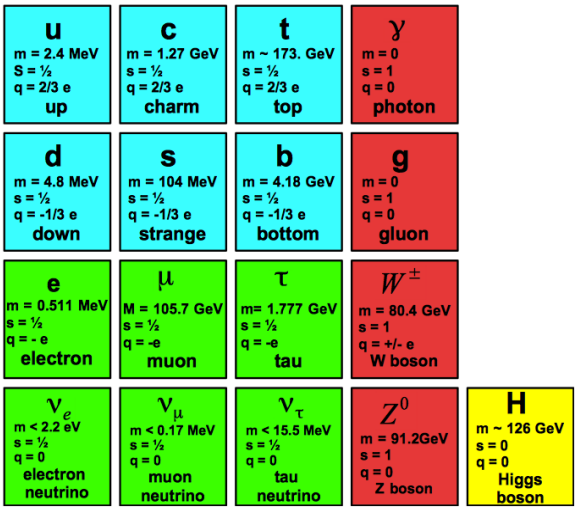

Figure 1.1: Standard model.

have $+2/3$ of electric charge (e) and d,s and b quarks have -1/3 of e. All charged leptons have $-e$ charge and all neutrinos are neutral and massless particles. These elementary particles have a corresponding anti-particle partner in the SM.

Force carrier bosons are called "gauge bosons" in the SM. They are the gluons, g, in the strong interactions, virtual photons, γ, in EM interactions and weak bosons, $W^{\pm}$ and Z^0, involved in weak interactions. The Higgs boson, H, was confirmed as a

fundamental particle in the SM after the discoveries [19, 20] reported by CMS [21] and ATLAS [22] experiments at LHC (Large Hadron Collider), CERN.

The SM is a gauge theory based on the local symmetry group $SU(3)_C \times SU(2)_L \times U(1)_Y$ where $SU(3)_C$ represents eight color charged gluons involves in strong interactions, $SU(2)_L$ corresponds to three vector bosons ($W^{\pm}$ and Z^0) of weak interactions and the $U(1)_Y$ represents the massless photon in the electromagnetic interactions. In addition to that, the subscripts C, L and Y represent color charge, left-handed chirality and weakly hypercharge respectively. This weak hypercharge operator is related to the electric charge, Q, and the third component (z-component) of weak isospin, I_3, as in the Gell-Man-Nishijima relation:

$$Q = I_3 + \frac{Y}{2} \tag{1.3}$$

This implies the unification of electromagnetic and weak interactions. In SM, the gauge symmetry group $SU(2)_L \times U(1)_Y$ represents the electroweak interactions.

1.2.2 Weakly interacting neutrinos

The spontaneous symmetry breaking of the gauge group $SU(2)_L \times U(1)_Y$ in SM describes the weak and electromagnetic interactions. Since neutrinos do not carry color or electromagnetic charge, they are interacting weakly by exchanging intermediate vector bosons, $W^{\pm}$ and Z^0. The weak interactions are described by the theory of electroweak interaction (called GWS model) which was formulated by Sheldon Lee Glashow, Abdus Salam and Steven Weinberg in between 1961-1967 [16, 17, 18].

The helicity, H, of a particle is defined as the projection of a spin vector, $\vec{S}$ along the momentum, $\vec{p}$ as $H = \vec{p} \cdot \vec{S}/|\vec{p}|$. According to the Dirac field theory, $\mathcal{L}_D = \bar{\psi}(i\gamma^\mu \partial_\mu - m)\psi$, of fermions with ψ ($\bar{\psi} = \psi^\dagger \gamma^0$) spinor field and 4×4 γ^μ-matrices[2], the chirality operator is defined by $\gamma^5 = i\gamma^0\gamma^1\gamma^2\gamma^3$ matrix. The γ^5 is

[2]where $\mu = 0, 1, 2, 3$ and $\gamma^0 = \begin{bmatrix} 1 & 0 \\ 0 & -1 \end{bmatrix}$ and $\gamma^i = \begin{bmatrix} 0 & \sigma^i \\ -\sigma i & 0 \end{bmatrix}$ with Pauli matrices $\sigma^i (i = 1, 2, 3)$

a pseudoscalar Hermitian operator with the eigenvalues of ± 1 which denoted the eigenfunctions of ψ_L and ψ_R as:

$$\gamma^5 \psi_L = +\psi_L \text{ and } \gamma^5 \psi_R = -\psi_R. \tag{1.4}$$

Now the representation of the spinor field ψ can be written as:

$$\psi = \psi_L + \psi_R. \tag{1.5}$$

Therefore the *chirality projection operators* P_L (left-handed) and P_R (right-handed) can be defined as:

$$\begin{aligned} \psi_L &= \frac{1-\gamma^5}{2}\psi = P_L \psi \\ \psi_R &= \frac{1+\gamma^5}{2}\psi = P_R \psi. \end{aligned} \tag{1.6}$$

The spin direction of neutrinos are parallel to their momentum while that for anti-neutrinos are opposite to the momentum (antiparallel to the momentum). Therefore, the helicity of neutrinos is given as left-handed ($H = -1$) and that for anti-neutrinos is given as right-handed ($H = +1$). The observation of the maximal parity violation of β-decay weak charged current interactions (exchange $W^{\pm}$ bosons) led to formulate the $V - A$ theory [23, 24, 25] where V stands for "vector" and A stands for "vector axial" as the field operator: $\gamma^\mu - \gamma^\mu \gamma^5 = \gamma^\mu (1 - \gamma^5)$.

1.3 Neutrino oscillations in vacuum

The neutrino oscillation describes the transition of one neutrino flavor into another flavor after propagating through space. According to SM, neutrinos are massless and therefore cannot oscillate into another flavor. The observations of neutrino oscillation imply that neutrinos have mass. The phenomenon of neutrino flavor oscillation can be described by quantum mechanics.

1.3.1 General formalism

A general theory for neutrino oscillation can be developed by introducing n number of flavor eigenstates $|\nu_\alpha\rangle$ (where $\alpha = e, \mu, \tau$) which are combinations of the orthonormal mass eigenstates of $|\nu_i\rangle$ where $i = 1, 2, 3$. Introducing a $n \times n$ unitary mixing matrix of U, one can write any α flavor eigenstate as a superposition of mass eigenstates:

$$|\nu_\alpha\rangle = \sum_i U^*_{\alpha i}|\nu_i\rangle. \tag{1.7}$$

This unitary matrix satisfies the property $UU^\dagger = 1$ and also the orthonormal eigenstates satisfy $\langle\nu_\alpha|\nu_\beta\rangle = \delta_{\alpha\beta}$ and $\langle\nu_i|\nu_j\rangle = \delta_{ij}$. Furthermore, any i^{th} mass eigenstate can be written as a combination of flavor states as:

$$|\nu_i\rangle = \sum_\alpha (U^*_{\alpha i})^\dagger|\nu_\alpha\rangle = \sum_\alpha U_{\alpha i}|\nu_\alpha\rangle \tag{1.8}$$

The massive neutrino state $|\nu_i(t)\rangle$ at time t is an eigenstate of Hamiltonian operator, $\mathcal{H}$, with a definite mass m_i and a definite energy E_i as:

$$i\frac{\partial}{\partial t}|\nu_i(t)\rangle = \mathcal{H}|\nu_i(t)\rangle = E_i|\nu_i(t)\rangle, \tag{1.9}$$

where natural units $c = \hbar = 1$ are used.
Therefore the time evolved mass eigenstate can be written as:

$$|\nu_i(t)\rangle = e^{-iE_it}|\nu_i(t=0)\rangle = e^{-iE_it}|\nu_i\rangle \tag{1.10}$$

Now the time evolved flavor eigenstate can be written as a combination of all flavor states by replacing mass eigenstates as:

$$|\nu_\alpha(t)\rangle = \sum_i U^*_{\alpha i}e^{-iE_it}|\nu_i\rangle = \sum_\beta \left(\sum_i U^*_{\alpha i}e^{-iE_it}U_{\beta i}\right)|\nu_\beta\rangle. \tag{1.11}$$

Eq. 1.11 implied the α flavor state at $t > 0$ is a superposition of all flavor states after propagation despite being created as pure α state at $t = 0$.

The probability of finding β flavor neutrino after time t time can be obtained by taking the square of the inner product of $\langle\nu_\beta|\nu_\alpha(t)\rangle$ which is the probability of the transition $\nu_\alpha \to \nu_\beta$,

$$P_{\nu_\alpha\to\nu_\beta}(t) = |\langle\nu_\beta|\nu_\alpha(t)\rangle|^2 = \sum_i \sum_j U^*_{\alpha i} U_{\beta i} U_{\alpha j} U^*_{\beta j} e^{-i(E_i - E_j)t}. \tag{1.12}$$

Since neutrinos are relativistic (the momentum $p >> m_i$), the energy E_i can be simplified by,

$$E_i = \sqrt{p_i^2 + m_i^2} \simeq p_i + \frac{m_i^2}{2p_i} \simeq E + \frac{m_i^2}{2E} \Longrightarrow E_i - E_j = \frac{\Delta m_{ij}^2}{2E} \tag{1.13}$$

where $\Delta m_{ij}^2 = m_i^2 - m_j^2$. Taking account the travelled distance, L, of the neutrino from the birth to time $t \simeq L$, the transition probability 1.12 can be written as:

$$P_{\nu_\alpha\to\nu_\beta}(t) = \sum_i \sum_j U^*_{\alpha i} U_{\beta i} U_{\alpha j} U^*_{\beta j} \exp\left(-i\frac{\Delta m_{ij}^2 L}{2E}\right). \tag{1.14}$$

In addition to that, the standard version of the neutrino flavor oscillation from one flavor state to another flavor can be simplified by introducing trigonometric identities into Eq. 1.14 as:

$$\begin{aligned} P_{\nu_\alpha\to\nu_\beta} = \delta_{\alpha\beta} - 4\sum_{i>j} \Re[U^*_{\alpha i} U_{\alpha j} U_{\beta i} U^*_{\beta j}] \sin^2\left(\frac{\Delta m_{ij}^2 L}{4E}\right) \\ + 2\sum_{i>j} \Im[U^*_{\alpha i} U_{\alpha j} U_{\beta i} U^*_{\beta j}] \sin\left(\frac{\Delta m_{ij}^2 L}{2E}\right) \end{aligned} \tag{1.15}$$

The probability of finding the same neutrino flavor state after propagating L distance is given by,

$$P_{\nu_\alpha\to\nu_\alpha} = 1 - \sum_{\alpha\neq\beta} P_{\nu_\alpha\to\nu_\beta}. \tag{1.16}$$

The formalism of neutrino oscillation implies that the oscillation probability is depending on L/E and also implies that neutrino mass difference is a non-zero quantity if the oscillations are observed.

1.3.2 Two flavour neutrino oscillation

Defining the unitary matrix of neutrino mixing with the mixing angle, θ, analogous to the Cabibbo matrix [26], the eigenstates of two flavor neutrinos of ν_α and ν_β are with two mass eigenstates of ν_1 and ν_2 can be written as:

$$\begin{pmatrix} |\nu_\alpha\rangle \\ |\nu_\beta\rangle \end{pmatrix} = \begin{pmatrix} \cos\theta & \sin\theta \\ -\sin\theta & \cos\theta \end{pmatrix} \begin{pmatrix} |\nu_1\rangle \\ |\nu_2\rangle \end{pmatrix} \tag{1.17}$$

After simplifying Eq. 1.15 for two neutrino mixing matrix with including useful experimental units of E, L and Δm^2 and including the ignored factors of $\hbar$ and c, the oscillation probability of finding ν_β from ν_α after traveling L distance can be described by:

$$P_{\nu_\alpha \to \nu_\beta} = \sin^2 2\theta \sin^2 \left(1.267 \frac{\Delta m^2[\mathrm{eV}^2] L[\mathrm{m}]}{E[\mathrm{MeV}]} \right), \tag{1.18}$$

and the probability of finding same ν_α after L distance is given by,

$$P_{\nu_\alpha \to \nu_\alpha} = 1 - \sin^2 2\theta \sin^2 \left(1.267 \frac{\Delta m^2 L}{E} \right). \tag{1.19}$$

The Eq. 1.18 and 1.19 have useful features for experiments making of neutrino oscillation measurements. The experimental observations of flavor oscillation can be divided into two type of experiments. The first type is the neutrino "appearance" experiments using Eq. 1.18. In this type, the experiment is observing the appearance of ν_β in the beam of ν_α. The next type is the "disappearance" experiments which probability corresponds to Eq. 1.19. The second type of experiments are looking for disappeared number of ν_α neutrinos in the ν_α beam.

The practical features of neutrino flavor oscillation equations 1.18 and 1.19:

- if the neutrino mixing angle $\theta = 0$, the then there is no flavor oscillation and that flavor eigenstates are identical to the mass eigenstates.
- the term $\Delta m^2 \neq 0$ should satisfy to observe a flavor neutrino oscillation. The neutrino oscillation can be happened only if neutrinos have different mass states with at least one neutrino mass needs to be non-zero.
- the parameter L/E let experimentalists to control their experiments. To construct an experiment with the maximal sensitivity for flavor oscillation, the last sin term should close to 1 as $\sin^2(1.267\Delta m^2 L/E) \sim 1 = \sin^2(\pi/2)$. Therefore $L/E \sim \pi/(2.54\Delta m^2)$ implies the flexibility to change the distance L or the beam energy E to observe maximal probability. However in solar neutrino experiments, the L/E has been fixed in the nature and the parameter space $(\Delta m^2, \theta)$ can be determined.

1.3.3 Evidences of neutrino oscillations

After Davis's first observations of oscillations from Homestake experiment, the solar neutrino oscillations have been observed in number of experiments such as Kamiokande [27], Super-Kamiokande (Super-K)[28], Soviet-American Gallium Experiment(SAGE) [29, 30], GALLium EXperiment (GALLEX) [31, 32], Sudbury Neutrino Observatory (SNO) [33] *etc.* The SNO experiment observed neutral current solar neutrino interactions and proved that the total neutrino flux was what was expected from theory. The absence of electron type neutrinos could then only be explained by oscillations.

The interactions of primary cosmic particles with the upper atmospheric nuclei produce secondary hadrons $\pi^{\pm}$ and $K^{\pm}$ that decay into neutrinos. These neutrinos are called atmospheric neutrinos. The evidence of atmospheric neutrino oscillations are observed by Kamiokande [27], Super-Kamiokande (Super-K)[34, 35] and IMB [36] detectors.

The neutrino flavor oscillations have been confirmed by using accelerator based neutrino experiments. The neutrino beam is created by colliding protons with a fixed

target to produce secondary charged mesons which decay into neutrinos. The flavor oscillation observations from the accelerator based long baseline neutrino experiments of MINOS (Main Injector Neutrino Oscillation Search) [37], T2K (Tokai to Kamioka) [38, 39] and K2K (KEK to Kamioka) [40] are consistence with Super-K atmospheric neutrino oscillation results.

According to Particle Data Group 2014 edition, current values of the neutrino oscillation parameters are presented in the Tab. 1.1. The table 1.1 has the best fitted

Parameter	Best fit $\pm 1\sigma$
$\sin^2\theta_{12}$	0.308 ± 0.017
$\sin^2\theta_{23}$, $\Delta m^2 > 0$	$0.437^{+0.033}_{-0.023}$
$\sin^2\theta_{23}$, $\Delta m^2 < 0$	$0.455^{+0.039}_{-0.031}$
$\sin^2\theta_{13}$, $\Delta m^2 > 0$	$0.0234^{+0.0020}_{-0.0019}$
$\sin^2\theta_{13}$, $\Delta m^2 < 0$	$0.0240^{+0.0019}_{-0.0022}$
$\Delta m^2_{21}[eV^2]$	$7.54^{+0.26}_{-0.22} \times 10^{-5}$
$\lvert\Delta m^2\rvert[eV^2]$	$2.43 \pm 0.06 \times 10^{-3}$

Table 1.1: Current neutrino mixing parameters of $(\Delta m^2, \sin^2\theta)$ from the PDG data released in 2014. Here $\Delta m^2 = m_3^2 - (m_2^2 + m_1^2)/2$. Therefore, if $m_1 < m_2 < m_3$ then $\Delta m^2 > 0$ and if $m_3 < m_1 < m_2$ then $\Delta m^2 < 0$

3-neutrino oscillation parameters from the latest experimental data [41, 42] including the measurements from Daya Bay [43], RENO [44], MINOS [45, 46] and T2K [47, 48].

Chapter 2

MiniBooNE Experiment (E898)

The Mini Booster Neutrino Experiment (MiniBooNE) at the Fermi Accelerator Laboratory (FNAL) in Batavia, Illinois was designed to verify or to reject the observed signature of $\bar{\nu}_\mu \rightarrow \bar{\nu}_e$ oscillation ($\bar{\nu}_e$ appearance) [49] by the Liquid Scintillator Neutrino Detector (LSND) experiment at Los Alamos National Laboratory. In this chapter, we briefly describe the motivation of the MiniBooNE experiment and the experimental setup.

2.1 Overview of experiment

The LSND experiment observed evidence of $\bar{\nu}_\mu \rightarrow \bar{\nu}_e$ oscillation with the oscillation probability of $(0.264 \pm 0.067 \pm 0.045)\%$. The excess of $87.9 \pm 22.2 \pm 6.0$ $\bar{\nu}_e$ events in the $\bar{\nu}_\mu$ beam [1] was observed. This observed excess was fitted with the two neutrino flavor oscillation model in the parameters space of Δm^2 vs $\sin^2(2\theta)$. Figure 2.1 shows the LSND observed event distribution [49] in L/E parameter space.

In the three neutrino oscillation model, the square mass difference of three mass eigenstates should satisfy the relationship of $\Delta m^2_{12} + \Delta m^2_{23} + \Delta m^2_{31} = 0$, where $\Delta m^2_{ij} = m^2_i - m^2_j$. The best fitted square mass differences of the atmospheric neutrino, Δm^2_{atm} and the solar neutrino, Δm^2_{sol} are approximately fitted as $\Delta m^2_{atm} \approx 3 \times 10^{-3}$

[1] created from μ^+ decay

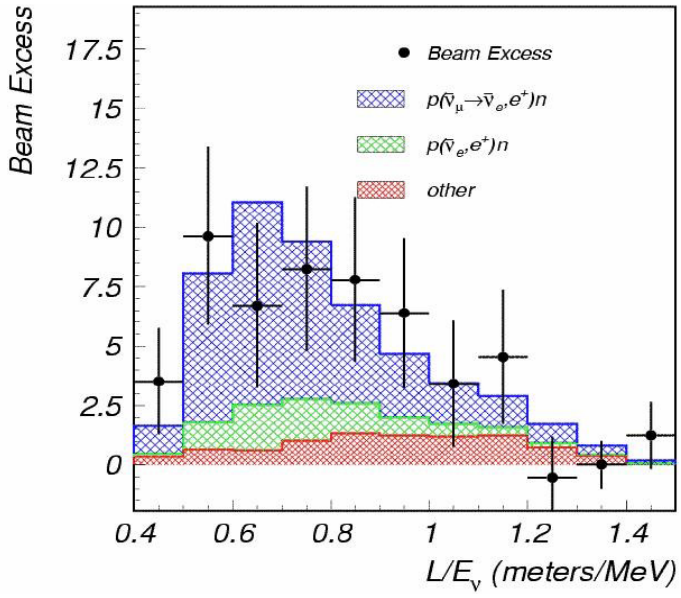

Figure 2.1: The LSND measured beam excess distribution in L/E parameter space. The plot shows the backgrounds and the expected neutrino oscillation.

eV^2 and $\Delta m^2_{sol} \approx 3 \times 10^{-5}$ eV^2 respectively. However, the LSND allowed region of the square mass difference, Δm^2_{LSND}(0.1 eV^2 to 10 eV^2), as shown in the Fig. 2.2 makes an inequality with the sum of $\Delta m^2_{LSND} \gg \Delta m^2_{atm} + \Delta m^2_{sol}$. That inequality indicates an existence of a fourth type of neutrino mass eigenstate to explain the LSND anomaly in the flavor oscillation model. Therefore this LSND anomaly motivated to design the MiniBooNE experiment with the same $L/E \sim 1$ m/MeV parameter space as LSND to verify the LSND observed signal.

2.2 Booster Neutrino Beamline at Fermilab

The Booster Neutrino Beamline (BNB) at Fermilab is the muon neutrino (ν_μ or $\bar{\nu}_\mu$) source with an average energy of $\sim$ 800 MeV for booster neutrino oscillation experiments such as MiniBooNE. The extracted accelerated protons from the booster ring with the kinetic energy of 8 GeV (8.9 GeV/c momentum) collide with beryllium target, which is placed inside the magnetic focusing horn. These collisions produce secondary mesons. These secondary mesons are focussed into a decay region by the toroidal magnetic field of the horn. The secondary mesons in the decay region decay in flight (DIF) to

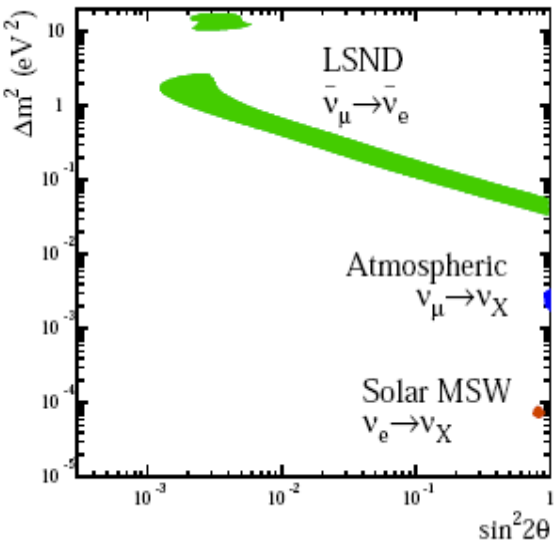

Figure 2.2: Allowed region of neutrino oscillation from the LSND results compared with the solar and atmospheric neutrino oscillation results.

give tertiary neutrinos and charged leptons. The remaining charged leptons (muons and electorns) and hadrons are absorbed by the absorber located at the end of the decay region. That process leaves only a beam of neutrinos for BNB experiments.

2.2.1 Booster proton beam

The Fermilab LINAC injects bunches of H^- ions with the kinetic energy of 400 MeV into the Booster synchrotron through the stripping foil placed between a series of dipole magnets. This foil strips electrons from the H^- ions and the resulting protons are accelerated up to the kinetic energy of 8 GeV through the Booster. The booster accelerated protons are extracted with the pulse width of 1.6 μs at the maximum rate of 5 Hz with 5×10^{12} protons per pulse. The extraction line of the booster accelerated protons for BNB at the Fermilab facility is shown in Fig. 2.3. These primary proton beam pulses are focused onto the beryllium target to produce secondary particles from the p-Be interactions.

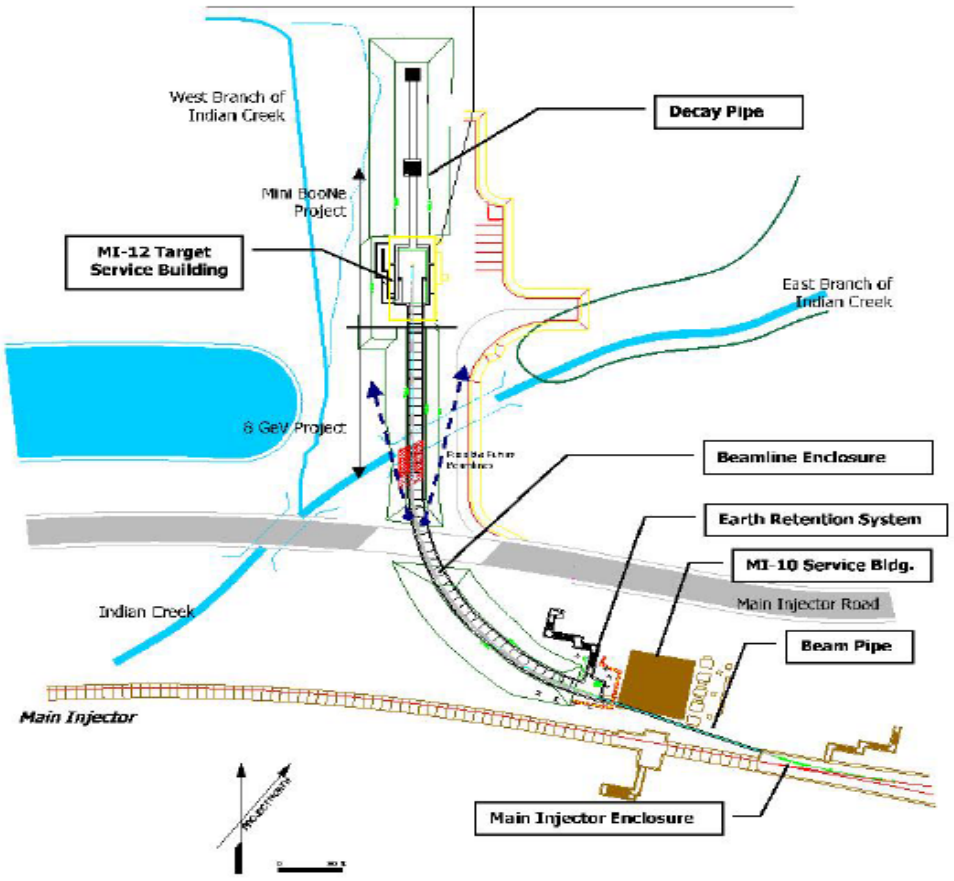

Figure 2.3: A schematic sketch of the Booster proton beam extraction.

2.2.2 Beryllium target

The 71.1 cm long beryllium target, which is placed inside the magnetic focusing horn, is comprised of seven cylindrical slugs each with 10.2 cm long and 0.48 cm radius. These cylindrical slugs are supported by three symmetrically attached beryllium "fins". In the Fig. 2.4 (Ref. [50]), the top figure shows a detail sketch of the target and the other components assembly as an "exploded" view and the bottom figure shows the assembled version of the components. Since the proton-Be interaction deposits ~ 600 W of heating power under the standard operating conditions, the target must be cooled. Therefore the entire target is cooled by circulating helium within the target with the help of the fins. The helium flow rate through the target length is 8×10^{-3} $m^3 s^{-1}$. The beryllium was chosen as the target material to minimize the radioactivity issues and the energy loss issues during the beamline in operations.

2.2.3 Magnetic focusing horn

The magnetic focusing horn is made of aluminum alloy. In Fig. 2.5 shows a schematic sketch of the focusing horn components. The horn is operated in the peak current of $\pm$170 kA with a 143 μs long pluses. The average pulse rate of the current is 5 Hz. The current flows through the inner conductor and back along the outer conductor (current flow direction depends on the selection of the electrical polarity) generating a toroidal magnetic field in the horn. The magnetic horn focuses secondary charged particles which have the desired electrical charge (+/-) into the decay region while defocusing the opposite electrical charge. Hence the running mode of the BNB (ν_μ beam or $\bar{\nu}_\mu$ beam) can be selected by choosing the direction of the current flow in the horn. In this magnetic focusing process, the neutrino flux is increased by six times more than the no focusing rate.

The azimuthal component of the magnetic field, B_ϕ, inside the horn is inversely proportional to the distance ($B_\phi \propto 1/R$), where R is the distance from the cylindrical symmetric axis of the horn. In Fig. 2.6 (from the reference [51]) shows that the

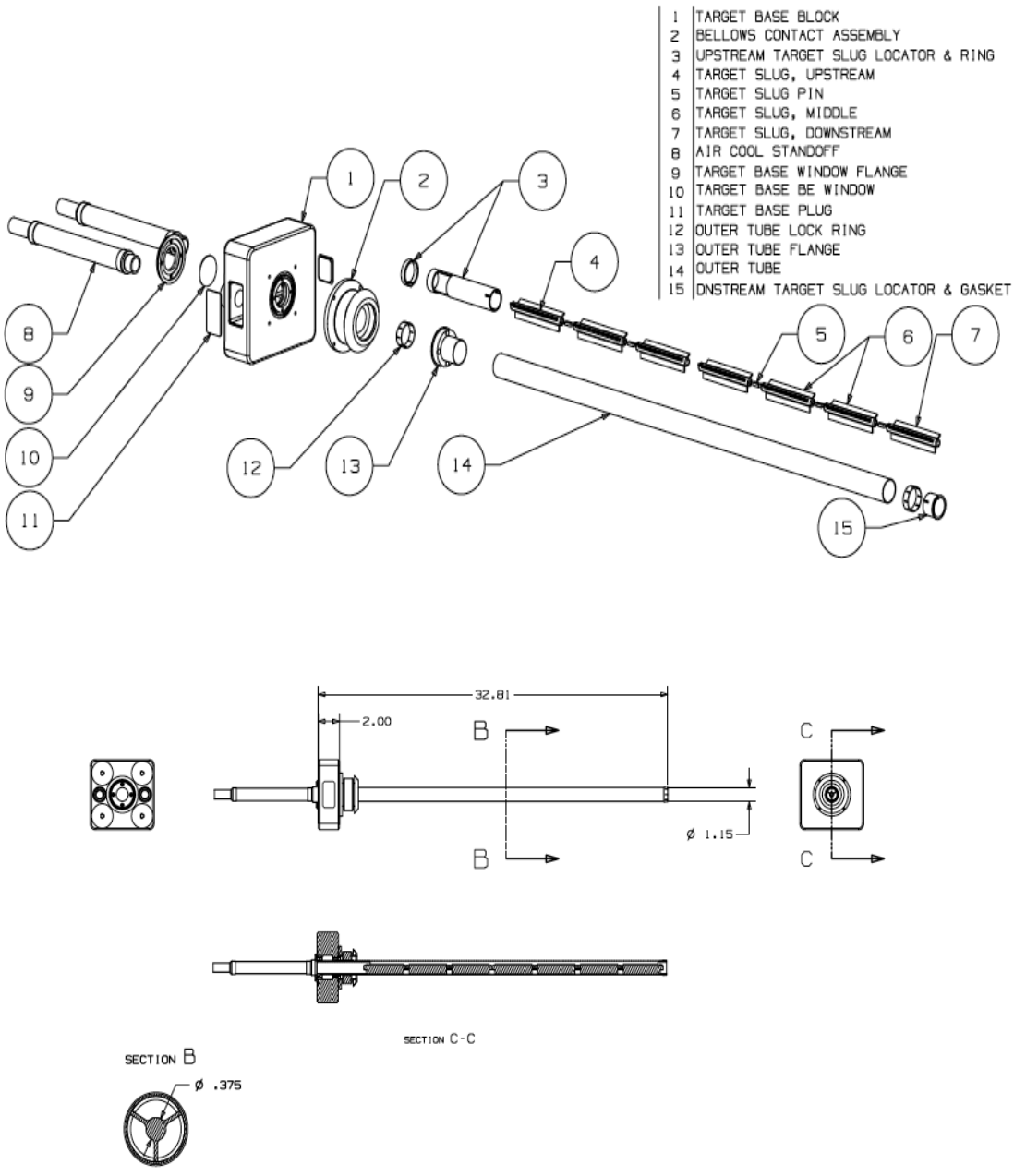

Figure 2.4: A schematic sketch of the target components take from [50].

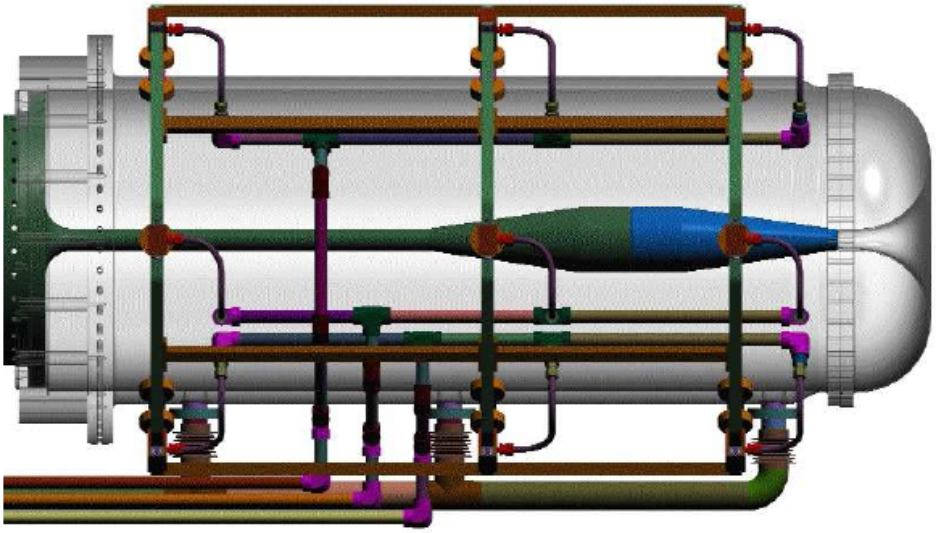

Figure 2.5: A schematic sketch of the magnetic focusing horn components.

measured azimuthal component of the magnetic field is consistent with the expected field of $\mu_0 I/2\pi R$. The horn is cooled by spraying water onto the inner conductor

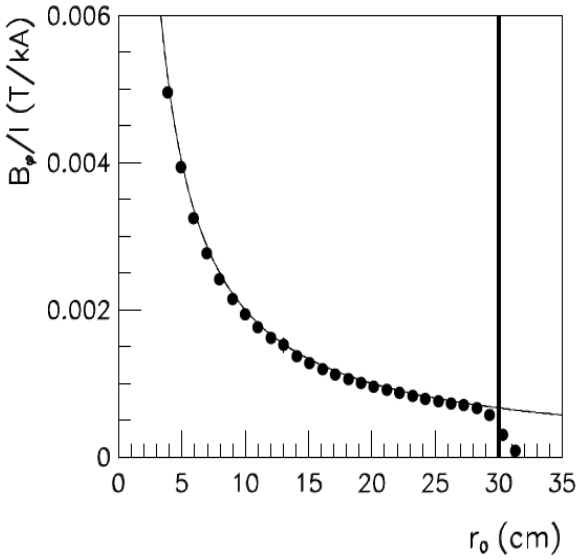

Figure 2.6: The behavior of the azimuthal magnetic field divided by the peak current in the horn. The points are represented as the measured magnetic field as a function of distance r from the horn axis and the dashed-line shows the expected $1/R$ behavior. The vertical line represents the inside edge of the outer conductor.

through the nozzles attached around the outer conductor.

2.2.4 Mesons decay region and tertiary neutrino beam

Secondary mesons focussed in the horn pass through a collimator, which located downstream of the horn. This collimator eliminates wide angle particles. The decay region is a 45 m long and 90 cm in radius air filled corrugated steel pipe surrounded by dolomite ($CaMg(CO_2)_3$). A steel and concrete wall located at the end of the decay region is used to absorb any charged leptons or hadrons left in the beamline.

This process results a pure neutrino beam for BNB detector volume. Several decay channels of mesons ($\pi^{\pm}, K^{\pm}$ and K^0_L) and charged leptons ($\mu^{\pm}$) are contribute for the final state neutrino beam. Most of them come from the pion decay. According to the branching ratios of the decay channels, some fraction of electron neutrinos (ν_e and $\bar{\nu}_e$) are contributed in both neutrino and antineutrino modes. The details of the flux being presented in chapter 3.

2.3 MiniBooNE setup overview

The MiniBooNE setup can be divided into two sections: the neutrino beam source and the MiniBooNE detector volume. A detailed description about the neutrino source for MiniBooNE experiment was discussed in chapter 2.2. In Fig. 2.7 shows the apparatus arrangement of neutrino beam production for MiniBooNE experiment. The MiniBooNE detector volume shown in Fig. 2.8 is located at 541 m downstream

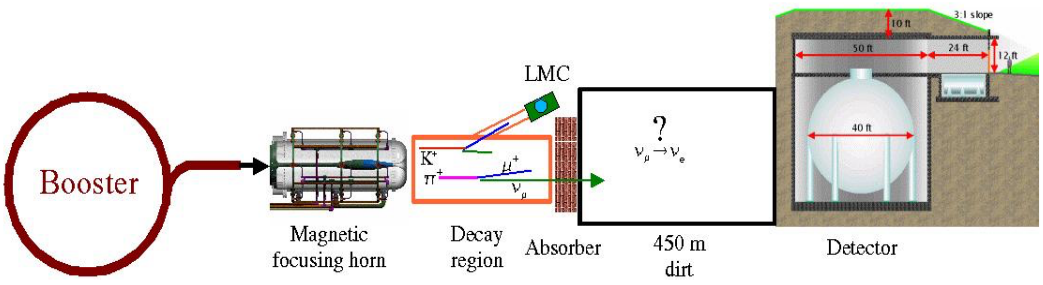

Figure 2.7: A schematic sketch of booster neutrino beamline for MiniBooNE experiment.

of the beryllium target as shown in Fig. 2.7 and also the detector has placed around

3 m underground to reduce the cosmic particle interactions. A detail description of the MiniBooNE detector can be found in [52]. The spherical MiniBooNE tank with the diameter of 12.2 m is made of carbon steel and the tank is filled with 800 tons of ExxonMobil Marcol 7 mineral oil. The oil serves both as the target for neutrino-matter interactions and as a scintillation and Cherenkov light producing medium for outgoing charged particles. The low density($\rho = 0.86 \mathrm{g/cm}^3$) and the high refractive index ($n = 1.47$ at $\lambda = 589.3$ nm and T = 20.0 ^{0}C) of mineral oil causes charged particles to produce a considerable amount of light.

The tank has been separated into two regions, an inner signal and outer veto region, by an optical barrier at the radius of 574.6 cm. The inner tank region has an array of 1280 8-inch photomultiplier tubes (PMTs) to detect light from the neutrino interaction within the fiducial volume. The outer veto region contains an array of 240 PMTs to collect light from background events, such as cosmic particle interactions.

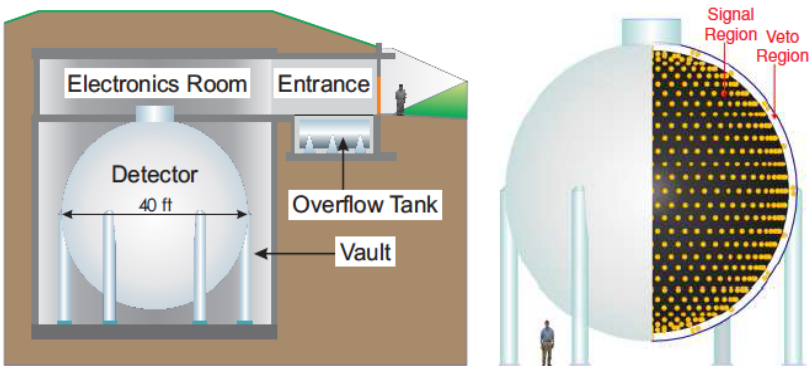

Figure 2.8: A schematic sketch of the MiniBooNE detector volume.

Chapter 3

Booster neutrino flux prediction

In this Chapter, the prediction of the neutrino beam fluxes for MiniBooNE experiment is briefly presented. The neutrino flux predictions are modeled using GEANT4 based Monte Carlo simulation [53]. The simulation uses incident proton beam profile, the beamline components geometry and materials information. A detail description of the neutrino flux prediction simulation can be found in the article [50].

3.1 Secondary particle production simulation

In the first place, the geometry and the material compositions of the beryllium target, aluminum horn and the components of the air filled decay volume including absorbers are defined in the GEANT4 simulation. In Fig. 3.1, taken from [51], shows a 3D geometrical view of the beamline components in the simulation.

3.1.1 Primary protons

In the simulation, the initial position and the initial kinematical variables of primary protons are defined to match the booster proton beam profile. The phase space profiles of the booster neutrino beam taken from beam optics measurements are listed in table 3.1.

In the GEANT4 simulation, the position, (x, y, z), of a primary proton with 8

$\bar{x}$	0.0 (mm)	$\bar{y}$	0.0 (mm)
σ_x	1.51 (mm)	σ_y	0.75 (mm)
$\bar{\theta}_x$	0.0 (mrad)	$\bar{\theta}_y$	0.0 (mrad)
σ_{θ_x}	0.66 (mrad)	σ_{θ_y}	0.40 (mrad)

Table 3.1: Primary proton beam profile parameters. These listed parameter limits are selected from the beam optics measurements. In the simulation, proton profiles are drawn using listed parameters and Gaussian distributions of mean 0 and width one.

GeV kinetic energy are randomly drawn by Gaussian distributions using the parameter limits listed in the table 3.1. Particularly, the initial coordinates are defined as:

$$\begin{aligned} x &= \bar{x} + \sigma_x \cdot r_1 \\ y &= \bar{y} + \sigma_y \cdot r_2 \\ z &= z_{in} \end{aligned} \tag{3.1}$$

where r_1 and r_2 are random numbers chosen from a Gaussian of mean zero and variance one and z_{in} is the user defined[1] initial longitudinal position of the proton.

The momentum space, (p_x, p_y, p_z), of the simulated proton is defined as:

$$\begin{aligned} p_x &= \sqrt{E_p^2 - m_p^2} \cdot (\bar{\theta}_x + \sigma_{\theta_x} \cdot r_3) \\ p_y &= \sqrt{E_p^2 - m_p^2} \cdot (\bar{\theta}_y + \sigma_{\theta_y} \cdot r_4) \\ p_z &= \sqrt{E_p^2 - m_p^2 - p_x^2 - p_y^2} \end{aligned} \tag{3.2}$$

where r_3 and r_4 are random numbers chosen from a Gaussian of mean zero and variance one, $E_p = K_p + m_p$ is the proton total energy where $K_p = 8.0$ GeV and m_p is the proton mass.

3.1.2 Secondary mesons

The secondary hadrons are produced by allowing randomly chosen protons to interact with beryllium nuclei. Every inelastic interaction has an ability to produce secondary

[1] In general, the longitudinal position is defined in terms of the target's initial position relative to the center plane ($z = 0$).

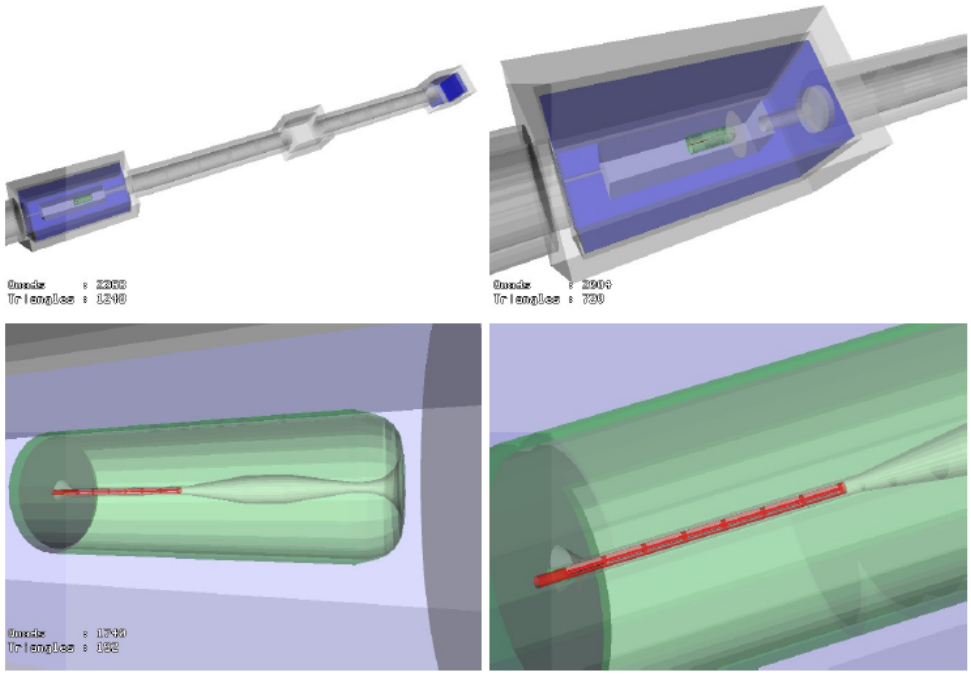

Figure 3.1: The geometrical view defined in the beamline simulation taken from Ref. [51].

hadrons. Therefore the simulation uses the double differential hadron production cross section measurements to predict the secondary mesons. The prediction of secondaries are determined by using several data fitted parameterizations of different models such as Sanford-Wang (SW) model and Feynman scaling model.

The experimental data taken from Hadron Production Experiment (HARP) at CERN [54] and BNL E910 [55] are used to predict $\pi^{\pm}$ productions in the simulation. A detail description of HARP experiment is given in Chapters 4. The HARP has measured $\pi^{\pm}$ data for the beam proton momentum, $p_B = 8.9$ GeV/c, and the BNL E910 has taken data for $p_B = 6.4, 12.3$ GeV/c [55] on a short beryllium target. The K^0 production simulation is based on E910 measured data for $p_B = 12.3, 17.6$ GeV/c and Abe, *et al.*, [56] at KEK experimental data for $p_B = 12.0$ GeV/c. These three particle ($\pi^{\pm}$ and K^0) productions are modeled with nine fitted parameters of Sanford-Wang model. The K^+ production simulation is based on data measured from eight production experiments and this simulation is modeled with seven fitted parameters

of a Feynman scaling model. The other type of possible hadrons could be produced from the inelastic interactions are protons, neutrons and K^-. Therefore p, n and K^- are modeled by using MARS15 Monte Carlo package [57, 58].

Sanford-Wang Model for $\pi^\pm$ and K^0

The measurements of double differential cross sections, $d^2\sigma/(dpd\Omega)$ for secondary meson production ($\pi^\pm$ and K^0) can be described by using a 9 parameterized (c_1 to c_9) Sanford-Wang (SW) model as:

$$\frac{d^2\sigma}{dpd\Omega} = c_1 p^{c2}\left(1 - \frac{p}{p_B - c_9}\right)\exp\left[-c_3\frac{p^{c_4}}{p_B^{c_5}} - c_6\theta(p - c_7 p_B\cos^{c_8}\theta)\right] \qquad (3.3)$$

where p and θ are the momentum and the angle of outgoing secondary mesons.

The fitted SW parameters for HARP and E910 measured data for $\pi^\pm$ and K^0 are shown in the Tab. 3.2. This list of parameter values are taken from the references of [50], [59] and [60]. A detailed description of SW fitting parameterization can be obtained by [51], [50] and [59].

Particle type	c_1	c_2	c_3	c_4	c_5	c_6	c_7	c_8	c_9
π^+	220.7	1.080	1	1.978	1.32	5.572	0.08678	9.686	1
π^-	213.7	0.9379	5.454	1.210	1.284	4.781	0.07338	8.329	1
K^0	15.13	1.975	4.084	0.9277	0.7306	4.362	0.04789	13.3	1.278

Table 3.2: Best fitted SW parameters for π^+, π^- and K^0 production data.

In the SW parameter fitting, c_9 has been fixed to 1.0 for pions and c_3 has been fixed to 1.0 for π^+ and to 5.454 for π^-. Fig. 3.2 and Fig. 3.3, taken from Ref. [59], show the production cross section measurements of π^+ and π^- secondaries from HARP short target data for the momentum range of (0.75 GeV/c - 6.5 GeV/c) and the angular range of (30 mrad - 210 mrd). The SW model fitted function with the K^0 production measurements is shown in the Fig. 3.4 (from Ref. [59]).

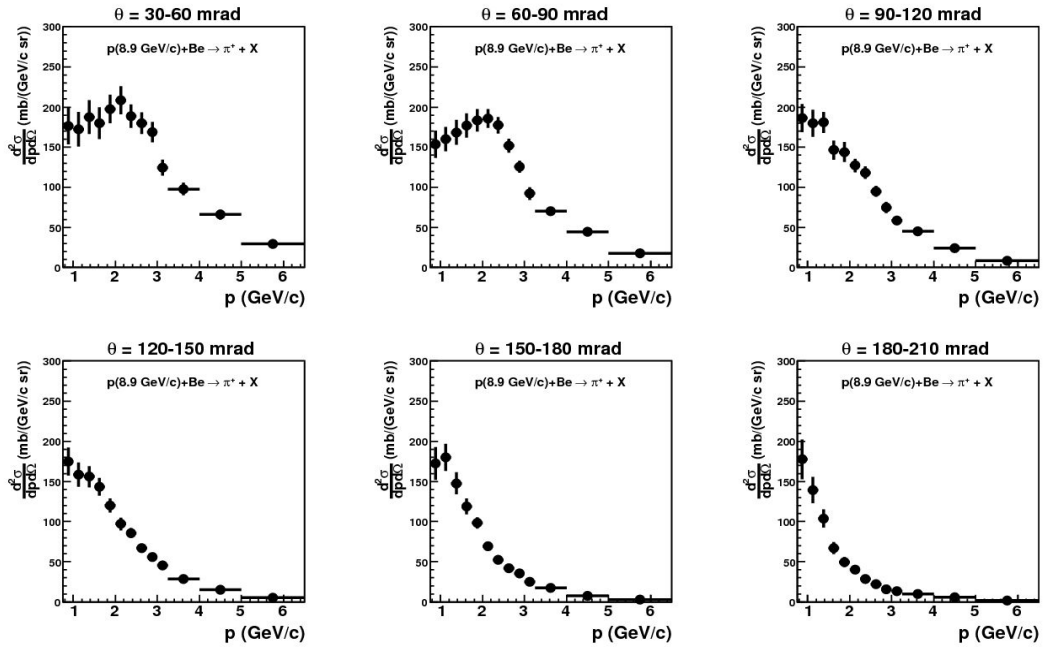

Figure 3.2: π^+ production cross section measurements from HARP short Be target data. This plot is taken from Ref. [59].

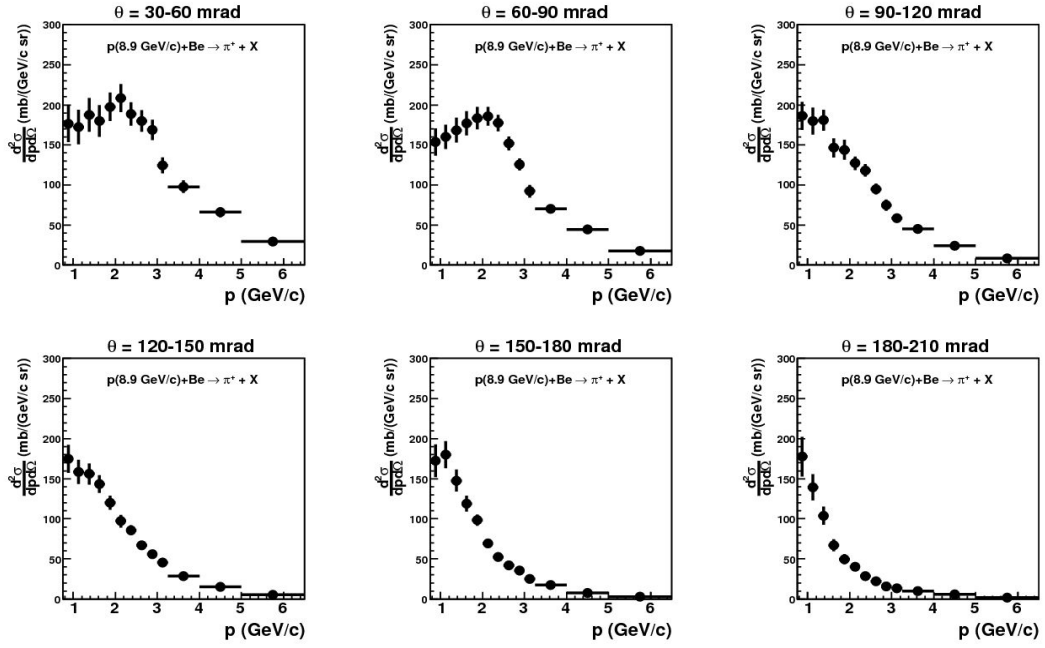

Figure 3.3: π^- production cross section measurements from HARP short Be target data. This plot is taken from Ref. [59].

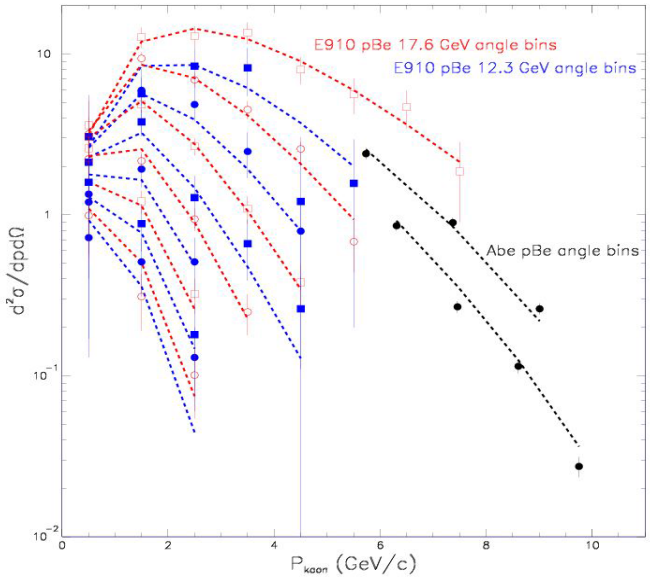

Figure 3.4: K^0 production data fitted with SW model from Ref. [59].

Feynman Scaling model for K^+

A Feynman Scaling (FS) model is used to describe the K^+ production data. It fits the data well to model secondary K^+ production in the BNB simulation. In Fig. 3.5 (Ref. [59]) shows fitted FS parameterization with K^+ data from 7 experiments. In the FS hypothesis, the model function depends only on the transverse momentum, p_T, and Feynman scaling factor, x_F, which is the ratio of the longitudinal momentum, p_L^{CM}, to the the maximum longitudinal momentum, $p_L^{CM(max)}$, in the center of mass frame.

$$x_F = \frac{p_L^{CM}}{p_L^{CM(max)}}. \tag{3.4}$$

According to the FS model the invariant cross section can be written as:

$$E\frac{d^3\sigma}{dp^3} = c_1(1-|x_F|)\exp[-c_2 p_T - c_3|x_F|^{c_4} - c_5 p_T^2 - c_7|p_T \cdot x_F|^{c_6}] \tag{3.5}$$

where E is the total energy. The invariant differential cross section term can be expanded as $Ed^3\sigma/dp^3 = Ed^2\sigma/(p^2 dpd\Omega)$. Units of p, p_T are expressed in GeV/c and E is expressed in GeV. Tab. 3.3 shows the best fitted FS parameterization for K^+

production data which is scaled to $p_B = 8.9$ GeV/c.

FS	c_1	c_2	c_3	c_4	c_5	c_6	c_7
K^+	11.70	0.88	4.77	1.51	2.21	2.17	1.51

Table 3.3: Best fitted Feynman scaling parameters for K^+ production data.

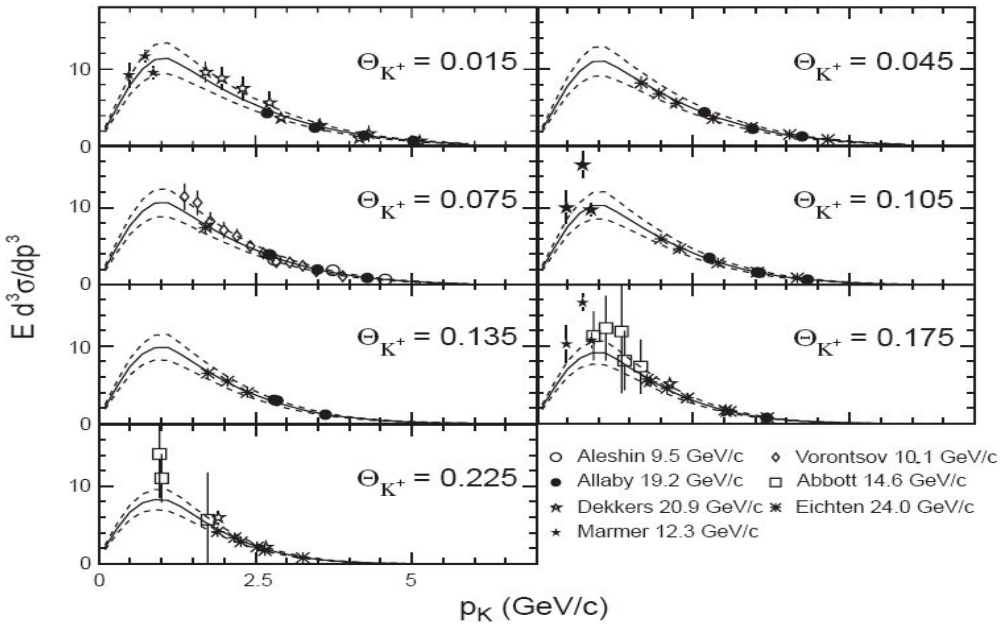

Figure 3.5: K^+ production data with the best fit of FS model (solid line) and the error limits from the covariance matrix (dashed-lines) taken from Ref. [59].

3.2 Neutrino Flux

The neutrino beam for MiniBooNE is a mix of $\nu_\mu, \bar{\nu}_\mu, \nu_e$ and $\bar{\nu}_e$ neutrinos from the decays of mesons and charge leptons of $\pi^\pm, K^0_L, K^\pm$ and $\mu^\pm$. The corresponding decays of positively charged parent are listed in the Tab. 3.4 with their branching ratios and lifetimes. Similarly, flux simulation has been modeled with negatively charged parent particle decays.

To model neutrino flux correctly, the simulation requires all secondary particles to propagate through the BNB components. Therefore inelastic/quasi-elastic interaction cross sections of $\pi^\pm$/K-Be/Al and p/n-Be/Al are taken account the particle interactions.

Parent particle	Lifetime (ns)	Decay mode	Branching ratio(%)
π^+	26.03	$\mu^+\nu_\mu$	99.9877
		$e^+\nu_e$	0.0123
K^+	12.385	$\mu^+\nu_\mu$	63.44
		$\pi^0 e^+\nu_e$	4.98
		$\pi^0\mu^+\nu_\mu$	3.32
K^0_L	51.6	$\pi^- e^+\nu_e$	20.333
		$\pi^+ e^-\bar{\nu}_e$	20.197
		$\pi^-\mu^+\nu_\mu$	13.551
		$\pi^+\mu^-\bar{\nu}_\mu$	13.469
μ^+	2197.03	$e^+\nu_e\bar{\nu}_\mu$	100.0

Table 3.4: Positively charged meson and leptons decay modes with their lifetimes and branching ratios to produce neutrinos.

The simulation of BNB was modeled using measured data (inelastic p+Be/Al), and with Glauber, Shadow and Geant4 default models. A detail description of the secondary particle propagation can be found in Ref. [59] and [50]

In the neutrino flux simulation, the neutrino kinematics are estimated by using kinematics of parent particles in four-momentum space. The neutrino energy in the lab frame is obtained by applying Lorentz boosts on neutrino energy calculated from the rest frame of parent particles.

The predicted total flux from the simulation for neutrino mode ($I_{\text{horn}} = +174$ kA) is shown in Fig. 3.6 and the contribution of parent particle decay modes for each neutrino meson decay is shown in Fig. 3.7. Similarly, the predicted total neutrino flux and the predicted neutrino channels from the parent decay modes for anti-neutrino mode ($I_{\text{horn}} = -174$ kA) are shown in Fig. 3.8 and Fig.3.9 respectively.

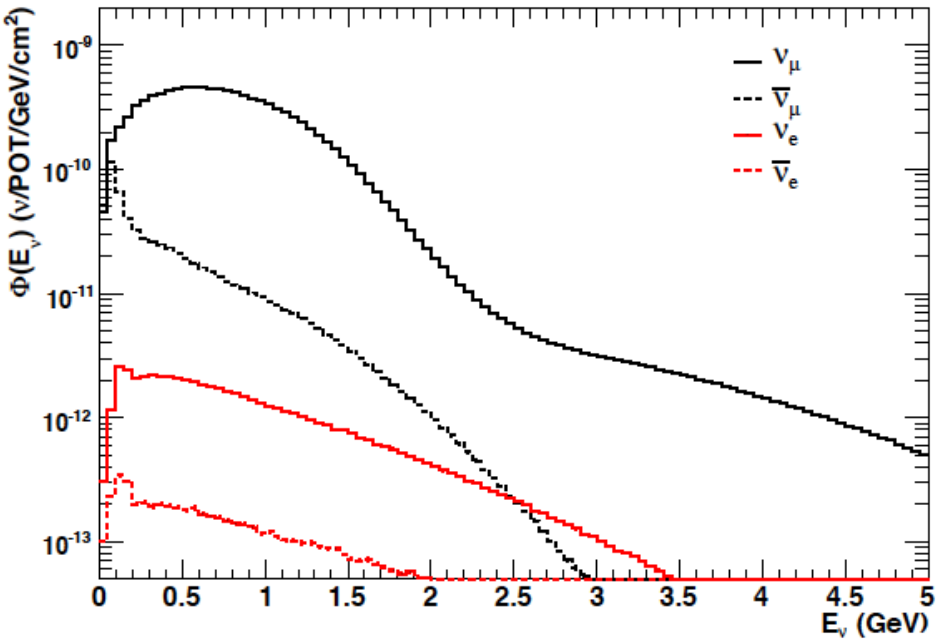

Figure 3.6: Total predicted neutrino flux for neutrino mode($I_{\text{horn}} = +174$ kA). Taken from Ref. [50].

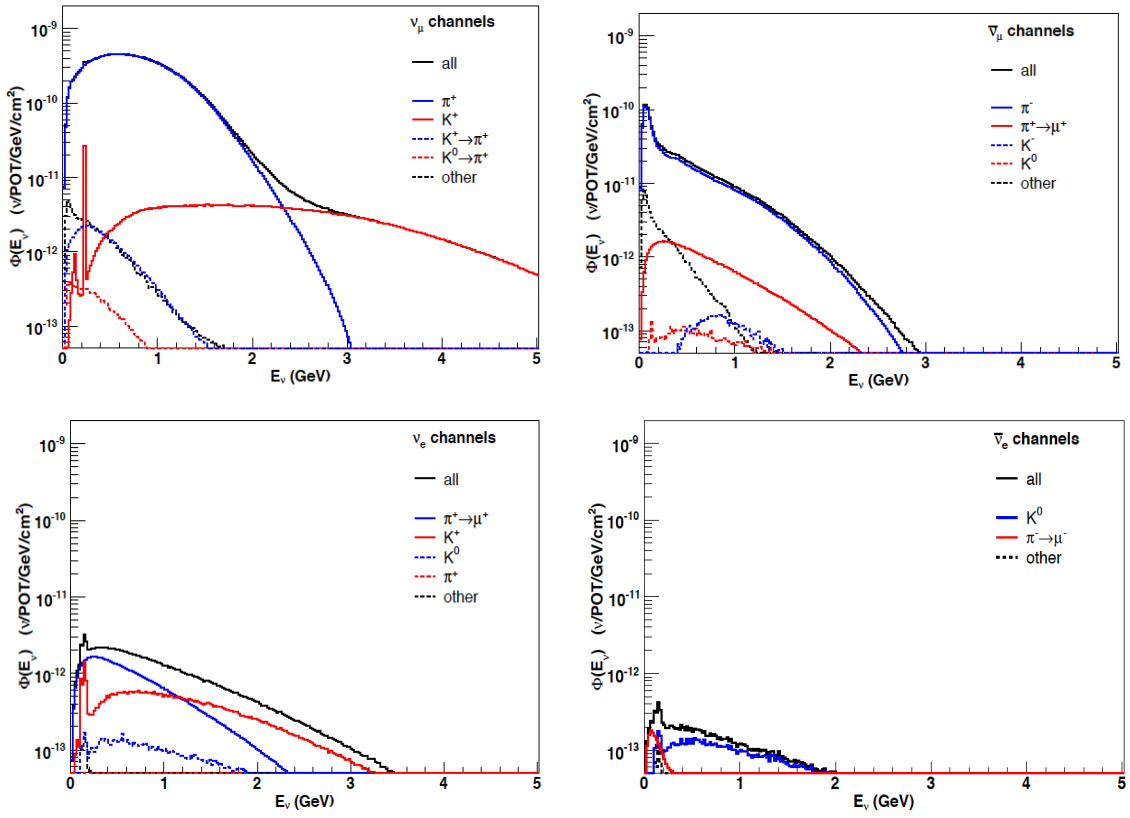

Figure 3.7: Predicted flavor neutrino channels in the neutrino mode. Here the distributions of ν_μ (top-left), $\bar{\nu}_\mu$(top-right), ν_{e} (bottom-left) and $\bar{\nu}_{\text{e}}$(bottom-right) are taken from Ref. [50].

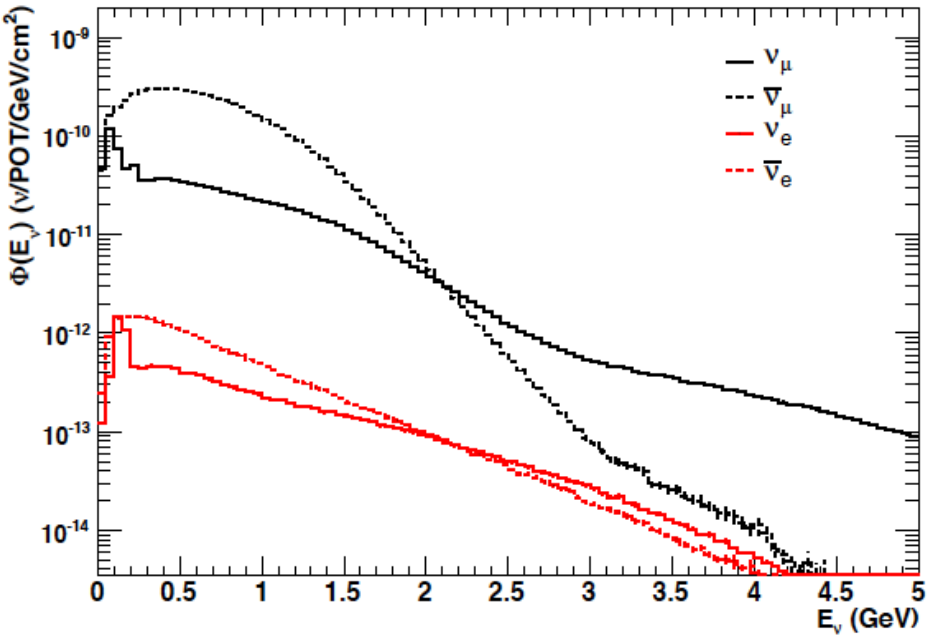

Figure 3.8: Total predicted neutrino flux for anti-neutrino mode($I_{\text{horn}} = -174$ kA). taken from Ref. [50].

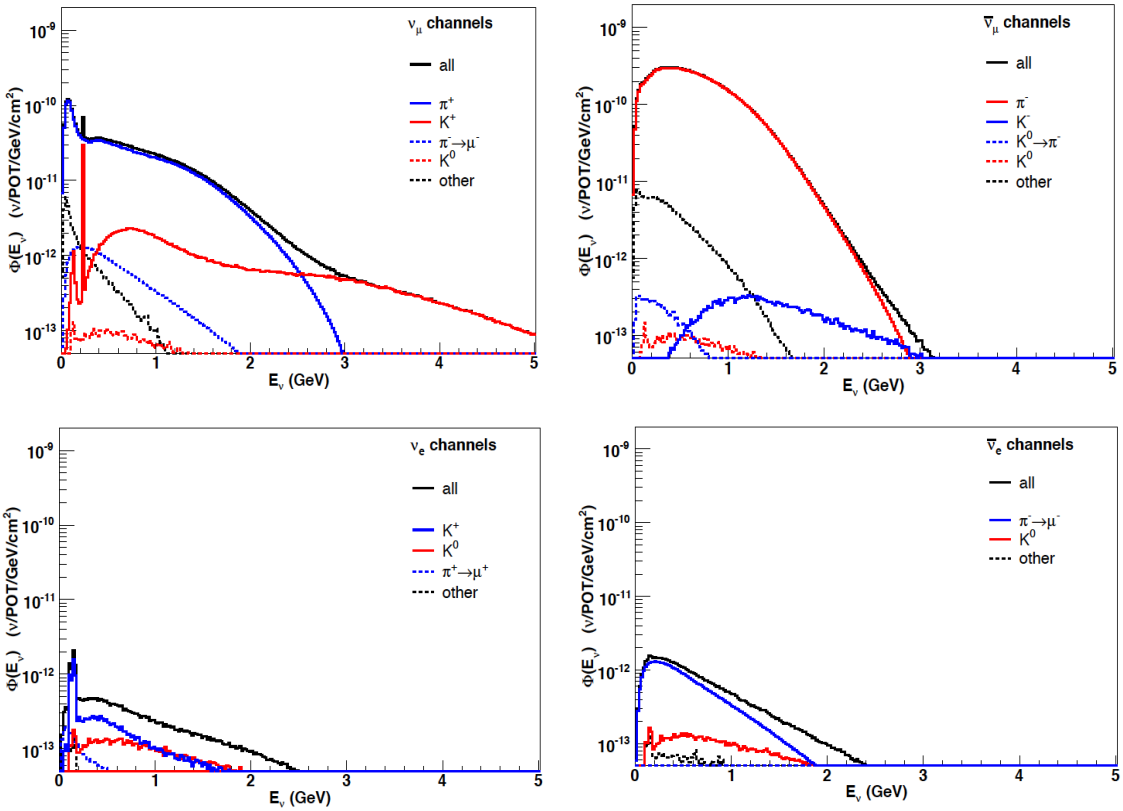

Figure 3.9: Predicted flavor neutrino channels in the anti-neutrino mode. Here the distributions of ν_μ (top-left), $\bar{\nu}_\mu$(top-right), ν_{e} (bottom-left) and $\bar{\nu}_{\text{e}}$(bottom-right) are taken from Ref. [50].

Part II

Analysis

Chapter 4

The Study of Hadron Production

The main objective of the study of charged pion production yield from the proton-Be interactions in long targets is to reduce the systematic errors on neutrino flux prediction for MiniBooNE experiment. That flux is predicted from a Sanford-Wang parameterized cross sections based on a 2.0 cm thick (5% λ_I) cylindrical beryllium target measurements. The prediction of $\pi^{\pm}$ production yield from the MiniBooNE Monte Carlo will be compared with the $\pi^{\pm}$ production yield of the long targets data (50% λ_I and 100% λ_I) at 8.9 GeV/c. This study on long targets data tests our extrapolation to the actual $\pi^{\pm}$ production from the 71 cm long beryllium target.

4.1 HARP experiment

The Hadron Production (HARP) experiment (PS214) at CERN [61] was designed to perform systematic and accurate measurements of production cross sections of secondary hadrons for low energy neutrino experiments. It was constructed to take secondary particle production data at the CERN Proton Synchroton (PS). It has been used to predict the neutrino flux for many low energy accelerator based neutrino experiments including K2K [62] at KEK, SciBooNE [63] and MiniBooNE [64] at FNAL. The incident beam, the CERN T9 beam, for HARP is extracted from the production

of secondaries by colliding the 28 GeV proton beam[1] (extracted from PS) with a fixed target at CERN. It produces a mixture of protons, pions, kaons, muons and electrons but the experiment chose to record data for pion and proton collisions. The momentum of the beam can be varied from 1.5 GeV/c to 15 GeV/c. HARP has a wide solid angular acceptance (4π acceptance) for particle detection.

4.2 HARP apparatus

This section gives a brief introduction to the HARP apparatus, the tracking system of incoming beam particles and the targets used for MiniBooNE experiment.

4.2.1 Overview

The HARP apparatus shown in Fig. 4.1 consists of three major detector systems:

- Upstream of the target chambers, Cherenkov counters and scintillation counters, which track the incoming beam and identify the particle type,
- A large angle spectrometer which tracks and momentum analyzes the outgoing large polar angle particles with a Time Projection Chamber (TPC), and
- A forward angle spectrometer which provides the particle trajectory and the particle type of outgoing particles covering the polar angle up to $\theta < 250$ mrad.

The target material is located inside the TPC volume. The solenoid magnet located around the TPC volume is used to bend the large-angle secondary tracks in the angular range $20° - 160°$ relative to the z-axis. A detail explanation about the large-angle spectrometer is given in [65]. However this large-angle measurements in the TPC volume are not used for the MiniBooNE targets data analysis.

The forward spectrometer is built around a dipole magnet used to measure the secondary particle momentum as shown in Fig. 4.1. Five drift chambers (NDC1-5) track the secondary particle trajectories. A Cherenkov detector (CHE), a time-of-flight wall (TOFW) and an electromagnetic calorimeter ECAL are used to identify the

[1]Proton beam is delivering a 400 ms long spill of 2×10^{11} protons in every 2.4 s.

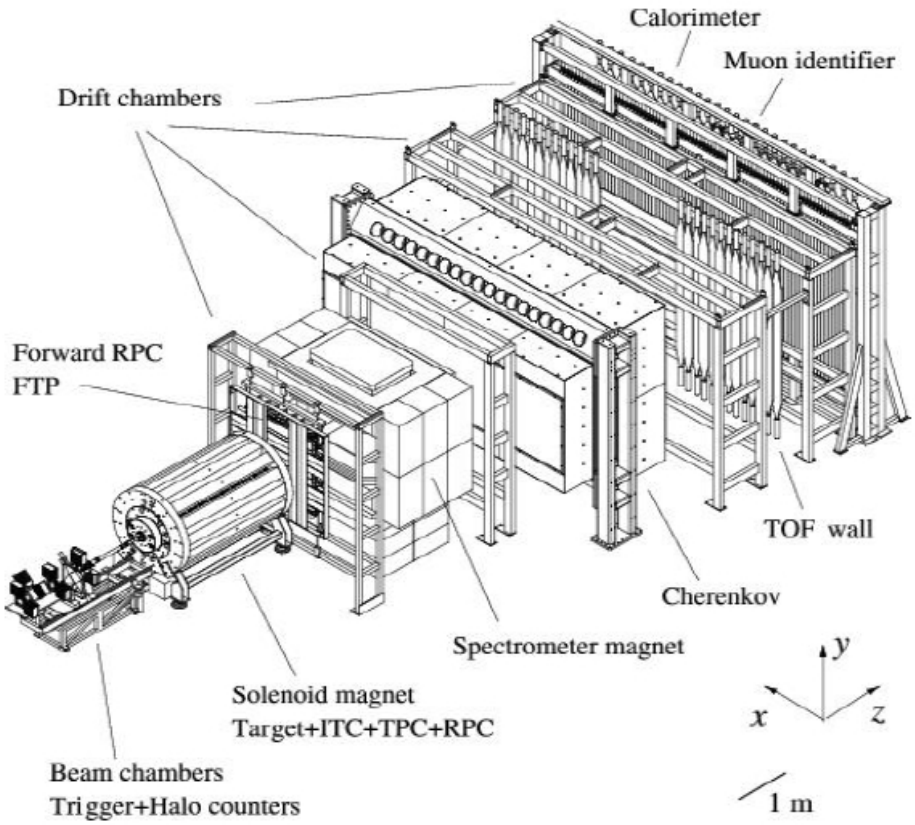

Figure 4.1: Schematic sketch of the HARP detector at CERN. The solenoid magnet apparatus which includes the target, time projection chamber (TPC) and the resistive plate chamber (RPC), Five drift chambers (NDC_{1-5}), the bending magnet, Cherenkov detector, Time of Flight (TOF) wall and electromagnetic calorimeter are shown.

particle type.

4.2.2 Tracking and identifying incident beam particles

The system upstream of the target used to track and identify the incoming particles is shown in Fig. 4.2. This upstream apparatus has two pressure adjustable nitrogen gas filled Cherenkov counters (BCA and BCB), two time-of-flight scintillator counters (TOFA and TOFB) and a circular disk of target-defining scintillator (TDS) which provides an extra timing information (combining the timing information from all three counters, provides enough accuracy to identify particles in the low momentum range). The Beam Scintillator (BS) provides a start for the event triggering. The

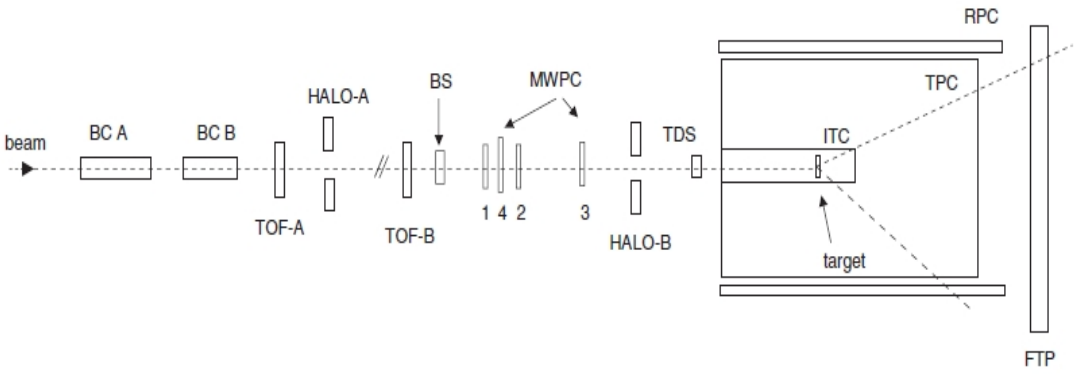

Figure 4.2: Schematic sketch of the upstream detector components of HARP setup to track the incoming particles. System consists of two Cherenkov counters (BCA and BCB), four triggering scintillator counters (BS, TOFA, TOFB and TDS), two HALO scintillator counters (HALO-A and HALO-B) and four multi wire proportional chambers (MWPC).

trajectory of an incident particle is tracked by four multiwire proportional chambers (MWPCs). Two HALO scintillation counters (HALO-A and HALO-B) with central holes are used to veto particles outside the beam axis. The accepted beam particles have no veto signal in HALO counters. The position and the direction of the incident particles are measured by the MWPCs with the accuracy of ~ 1.0 mm and ~ 0.2 mrad. The MWPC information is used to extrapolate the position of the incoming beam particles, (x_0, y_0), at the center plane ($z = 0$) of the target region and to measure

the angle of the incoming particles. Incident beam particle types are identified by using two Cherenkov counters (BCA and BCB) for higher momentum particles. The separation of identifying protons and pions through the Cherenkov counters BCA and BCB are shown in Fig. 4.3. The identity of lower momentum (< 3 GeV/c) particles is determined by the measurements of time-of-flight hits of two identical scintillators, TOFA and TOFB, and of TDS. This timing information of the beam particles is given by the time difference of particle traveling through 21.4 m distance between TOFA-TOFB scintillator counters and the time difference of traveling through 24.3 m distance between TOFA - TDS counters (see Fig. 4.2). The averaged arrival time, t_0, of the

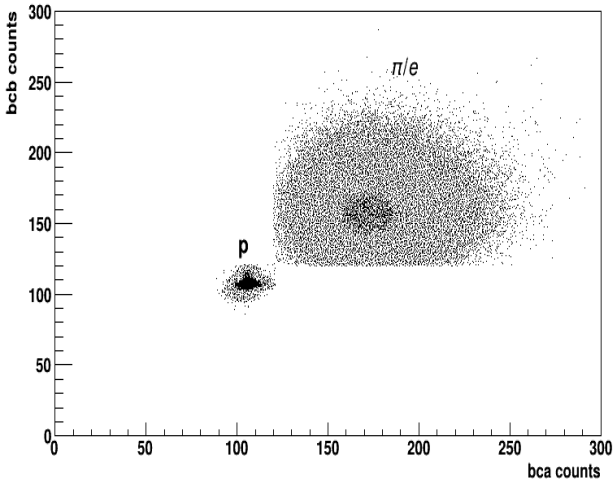

Figure 4.3: BCB vs BCA Cherenkov counts: The separation of the 8.9 GeV/c incoming beam pions and protons identification by Cherenkov counters BCA and BCB.

beam particles at the center plane is estimated by using the measured particle velocity (β), particle ID and the known momentum from the T9 beam. This t_0 is an important factor in measuring the time-of-flight of secondary particles to the TOF-wall in the forward spectrometer.

4.2.3 Targets for MiniBooNE

HARP has taken measurements on 2 cm ($5\%\lambda_I$) long beryllium target, Be5, which was used to analyze the secondary production cross sections as described in [59]. In order to check effects of the pion production on long targets, HARP also took data

on a one interaction length, 40 cm ($100\%\lambda_I$), long beryllium target of 0.48 cm radius named as MB100 and a half interaction length, 20 cm ($50\%\lambda_I$), long beryllium target named as MB50 with the same radius of 0.48 cm. The cross sections of MB100 and MB50 targets are the same as the actual MiniBooNE target. Fig. 4.4 shows the cross sectional geometries of MB100 and MB50 targets with their three cooling fins on it, and also the Be5 short target. To reduce the edge effects, we have made a radius cut

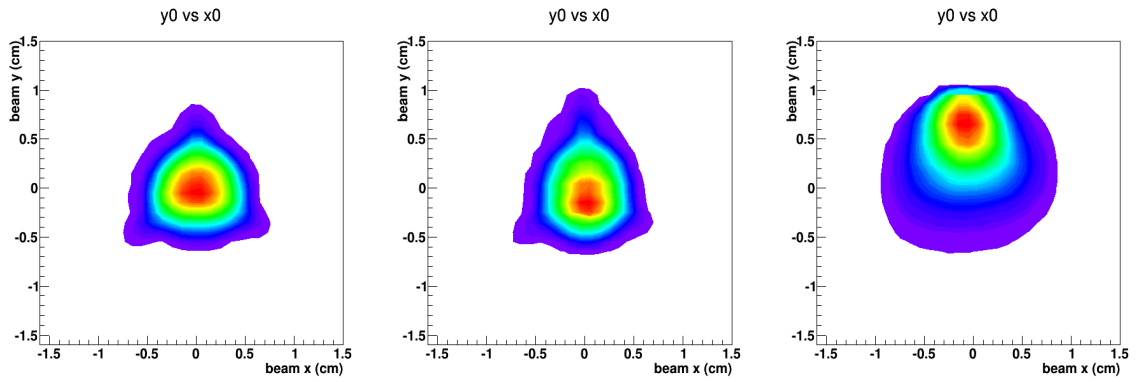

(a) (b) (c)

Figure 4.4: Cross sectional view of the extrapolated p-nuclei interaction points on (a) MB100 (b) MB50 and (c) Be5 (1cm radius cut) targets from MWPC measurements. MB100 and MB50 contains three fins on each as shown in the plots (a) and (b)

of 0.4 cm on the incident T9 beam for MB100 and MB50 targets. The geometries of the target and the radius cuts of the incident beam used for the analysis are shown in Table 4.1.

Target	Beam radius cut (cm)	thickness (cm)	target radius (cm)
Be5	1.0	2.0	1.5
MB100	0.4	40.0	0.48
MB50	0.4	20.0	0.48

Table 4.1: Geometries of three targets and the corresponding beam radius selections on each target.

4.3 Tracking secondary particles

The forward spectrometer has five drift chambers, NDC1-5, located as shown in Fig. 4.5. These measure the secondary particles trajectory through out the detector. The cross sectional dimension 3 m × 3 m of each NDC module provides a large solid angular coverage for secondaries. A detailed description of the properties of chambers can be found in Ref. [66]. The dipole magnet with the aperture size of

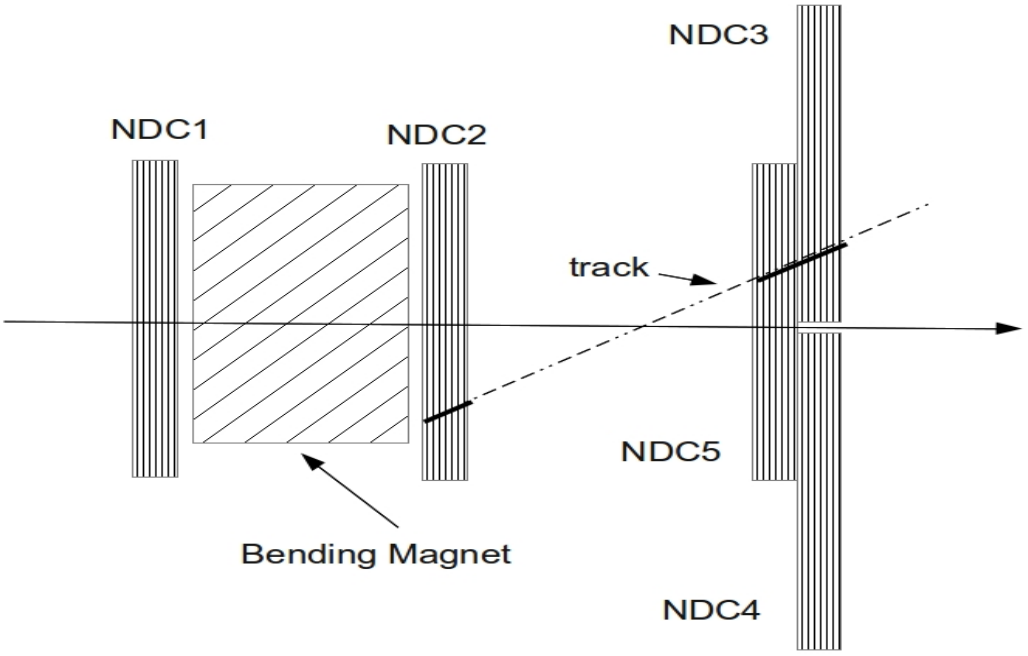

Figure 4.5: Schematic sketch of a NDC modules and the dipole magnet in the forward spectrometer.

($x \times y \times z = 2.41$ m × 0.88 m × 1.72 m) is located in between NDC1 and NDC2. The mapping of the B_y magnetic field is described in the reference [67]. The momentum of a secondary particle is reconstructed by matching reconstructed segments of tracks downstream of the magnet with either the center of the target (VERTEX2 algorithm) or with the track segment in NDC1 (VERTEX4 algorithm).

4.3.1 Track reconstruction algorithm

Secondary particles are tracked as they pass through the forward spectrometers as shown in Fig. 4.6. Every NDC chamber contains four modules each with three wire

planes $(-5°, 0°, +5°)$. All together, each NDC chamber has 12 wire planes. More details about wire plane modules in NDC chambers can be found in [67]. The momentum of the particle is determined by combining a track the downstream of the dipole magnet with the track in the upstream region. First, all particle track segments have to satisfy the plane 2D condition and the track 3D condition for each NDC chamber as described below:

- Plane (2D) segment : Needs at least three hits out of four in the same projection (u, x,or v) $(-5°, 0°, +5°)$ compatible with being aligned.
- Track (3D) segment : The intersection of two or three plane segments on different projections is defined as 3D straight line. If only two plane segments are found then an additional hit from the remaining projection is required to define the 3D straight line. Segment needs to have at least 7 hits out of 12 planes on the same NDC module.

After passing the above requirements in each individual module, that track segments can be combined with the other NDC module track segments to develop the extended long 3D track. Finally the momentum of the particle is measured by combining downstream long 3D track with either the 3D vertex point on the center plane ($z = 0$) of the target or the 3D segment of NDC1 module in the upstream of the dipole magnet. The former track is called "VERTEX2-tracks" and the estimated momentum is called "p_2 - momentum" and the later track is named "VERTEX4-tracks" and the reconstructed momentum is called "p_4 - momentum". The momentum of a VERTEX2 track is estimated by minimizing the matching χ^2_{v2} of the extrapolated target center position with the actual position measured with the beam spectrometer.

For VERTEX4 tracks, the momentum is estimated by minimizing the matching χ^2_{v4} of measured 3D NDC1 module segment with the extrapolated 3D coordinate at the NDC1 module by the 3D track segment of downstream. In Fig. 4.7 illustrates this two track reconstruction algorithms. All these procedures for momentum reconstruction are done by using a sophisticated HARP developed package named RecPack [68],

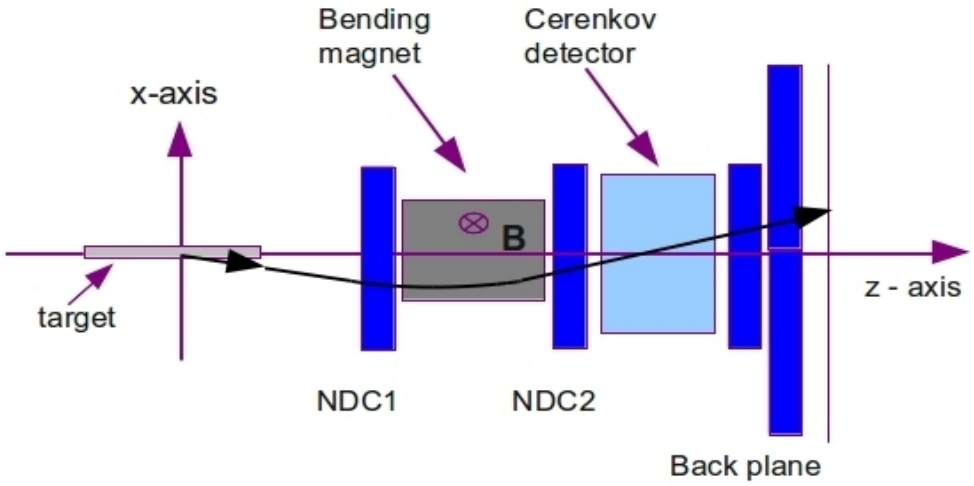

Figure 4.6: Schematic drawing of a positive track which is passing through NDC chambers, bending magnet, Cherenkov detector and back plane chambers.

which is based on the Kalman filter fitting technique [69].

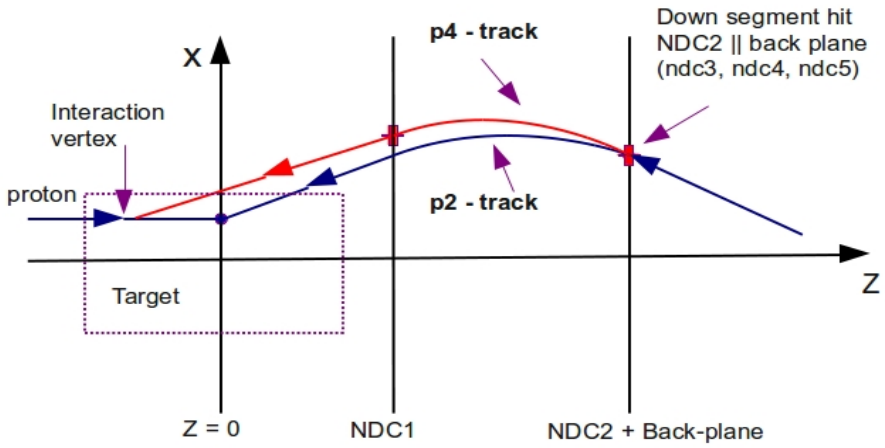

Figure 4.7: Sketch of the illustration of track reconstruction by VERTEX2 and VERTEX4 algorithms. Here the downstream track combine to the center plane coordinates to reconstruct the VERTEX2 type tracks and also the downstream tracks combine with NDC1 3D segments to reconstruct the VERTEX4 type tracks.

4.3.2 Resolution of p2 and p4 tracks

The performance of both track reconstruction algorithms can be compared by looking at the correlation between the reconstructed and the generated momentum (p_{true}) of the long target Monte Carlo data. Figure 4.8 compare reconstructed p_2 and p_4 momenta with the generated momentum (p_{true}); they are highly correlated in each case. The correlation of resolution of p_2 and p_4 momenta with the interaction vertex is also shown in Fig. 4.8.

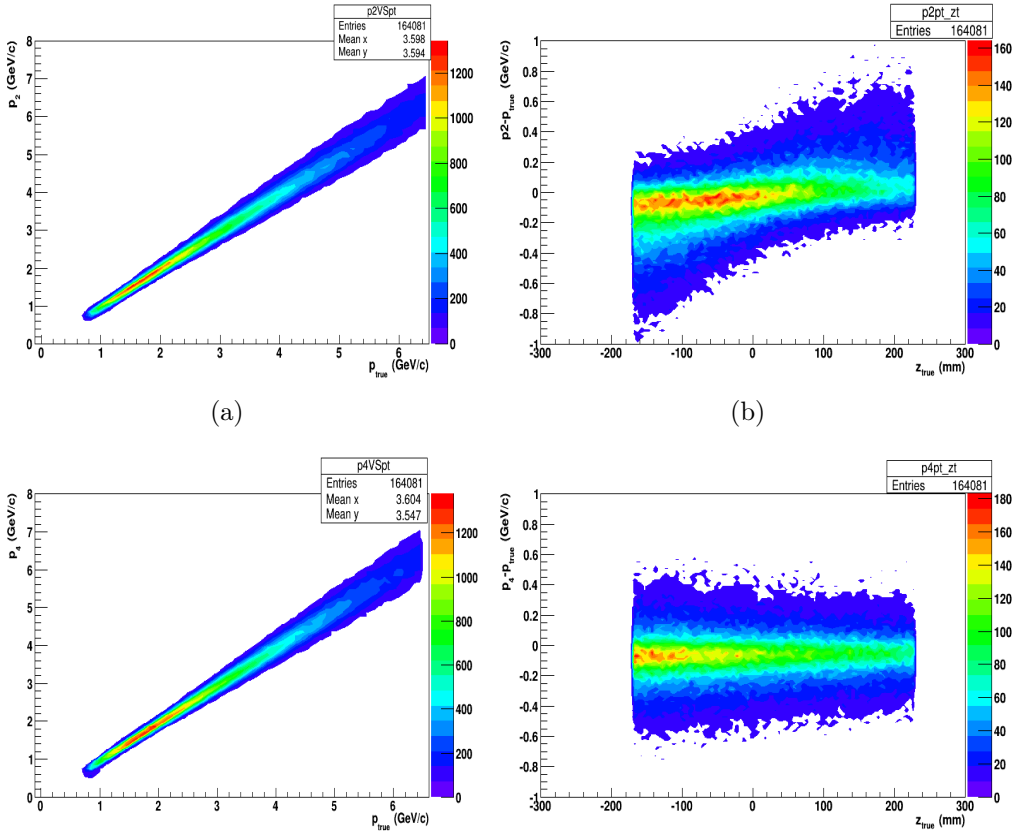

(a) (b)

(c) (d)

Figure 4.8: p_2 and p_4 correlations with the generated momentum and the interaction vertex for positive particles. This measurements are taken in the range of $-270 \leq \theta_x \leq 0$. (a) p_2 vs p_{true} (b) $p_2 - p_t$ vs interaction vertex-z (c) p_4 vs p_{true} (d) $p_4 - p_t$ vs true interaction vertex-z.

The VERTEX2 track reconstruction process assumes that the particle originated at the center plane ($z = 0$) of the target as described. The reconstructed p_2 momentum is lower than the actual momentum when they are produced in the upstream of the

target center ($z < 0$) as shown in Fig. 4.9. In the same way, the reconstructed p_2

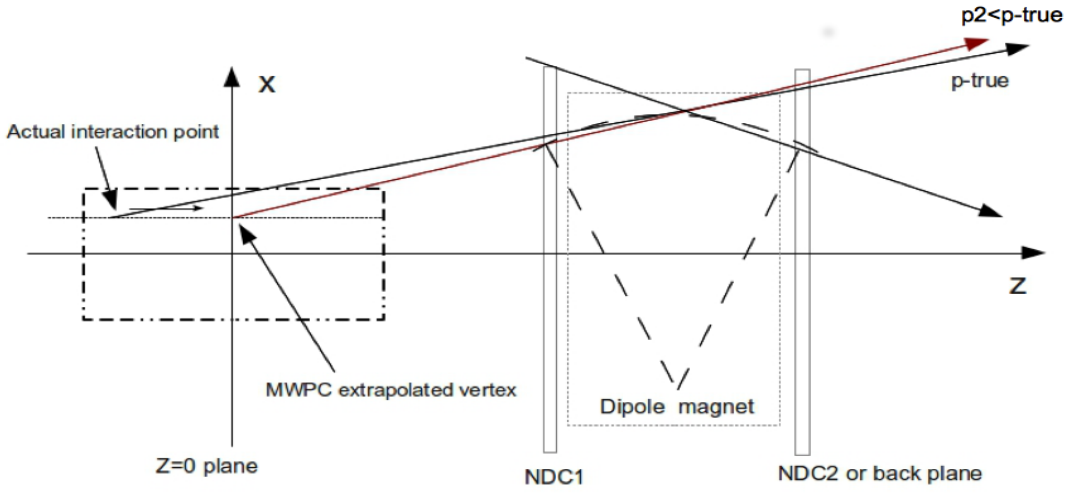

Figure 4.9: Schematic sketch of the p_2 track reconstruction process at the center plane ($z = 0$) by vertex2 algorithm. This shows the interaction vertex (x,y) coordinate have been constrained to be in the center plane during the extrapolation of MWPC.

momentum is higher than the actual when the particle is produced in the downstream ($z > 0$). The asymmetry of the p_2 momentum resolution through the interaction vertex measurements of secondary tracks[2] is seen very clearly in Fig. 4.8 (b). In Fig. 4.8 (d) shows a symmetric behavior of the reconstructed p_4 momentum along the interaction vertex for same event sample. As an example of the difference between VERTEX2 and VERTEX4 fitting algorithms, the resolution of reconstructed p_2 and p_4 with the truth momenta in the upstream on the target center ranging $-170 \leq z_{true} \leq -140$ mm is shown in Fig. 4.10. Figure 4.10 (a) clearly depicts an asymmetry for the p_2 tracks. This asymmetry is absent in the p_4 fits (Fig. 4.10 (b)) . To avoid the momentum asymmetry and the vertex position dependency we use VERTEX4 type tracks in this whole analysis.

4.3.3 Kinematical variables

Eventually, the production yield of the secondary particles will be reported in terms of momentum, p, and the angle with respect to the beam axis (z-axis), θ. However,

[2]Positive charged tracks that pass in the negative half of the x-z plane ($-270 \leq \theta_x \leq 0$ mrad) have been selected to see this correlation.

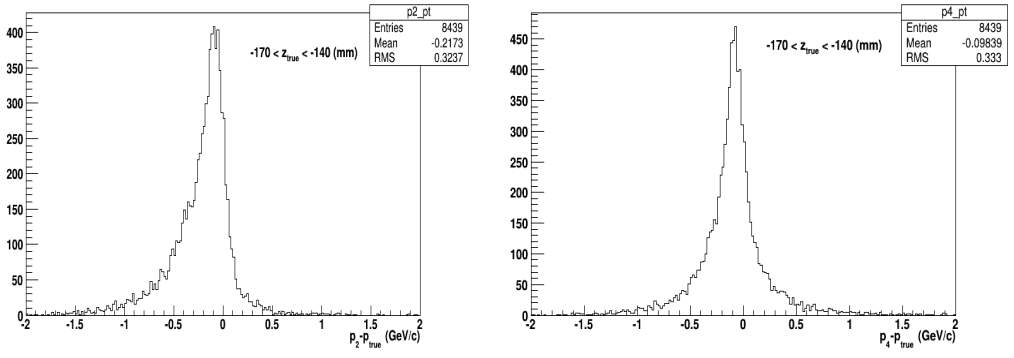

(a) (b)

Figure 4.10: The resolution of reconstructed momentum in the range of $-170 \leq z_{true} \leq -140$ and $-270 \leq \theta_x \leq 0$. (a) $p_2 - p_{true}$ and (b) $p_4 - p_{true}$.

because of the rectangular shaped geometry of the drift chambers and the Cherenkov detector volume, measurements are carried out on the 3D space of (p, θ_x, θ_y) as kinematical variables where $\theta_x = tan^{-1}(p_x/p_z)$ and $\theta_y = tan^{-1}(p_y/p_z)$. These are later summed into p, θ bins.

4.4 Particle identification

The particle identification algorithm uses the Cherenkov counters and the time of flight wall, TOFW. The Cherenkov detector located downstream of the magnet is filled perfluorobutane C_4F_{10} which has high refractive index. The Cherenkov detector has the cross section of 6 m $\times$ 3 m opening. The references [67, 59] provides more details about the Cherenkov detector. The TOFW detector covers the area of 6.5 m $\times$ 2.5 m with the approximated resolution of $\sigma \sim 250$ ps. It can separate pions from protons up to 3.5 GeV/c. A detailed description of TOFW counter is given in Ref. [70].

Combining Cherenkov and TOFW detector performances and defining a probability density function (PDF), the pions, proton and kaons are separated from each other. The secondary particle identification algorithm for long targets is similar to the short target Be5 analysis as described in [59]. Since the pion production cross section from the short target analysis is small above the 6.5 GeV/c, the upper bound of the long target analysis is set to 6.5 GeV/c, the same as the short target analysis.

The fractional contribution of kaons to the pion yield is a negligible factor in this momentum range.

The performance of the C_4F_{10} gas filled Cherenkov detector in the HARP setup has been studied by a 12.9 GeV/c pion beam on a short Aluminum target as described in the [59]. Figure 4.11 shows the number of photoelectrons as a function of momentum measured from MB100 target data. The pion Cherenkov threshold is clearly visible at 2.6 GeV/c. The Cherenkov thresholds for kaons and protons are 9.3 GeV/c and 17.6 GeV/c respectively. Therefore the pions are separated from protons and kaons by Cherenkov detector for the momentum $p > 2.6$ GeV/c. In addition to that, the Cherenkov detector response in momentum $p < 2.6$ GeV/c is used to veto electrons in the particle identification process. This electron events are clearly visible at number

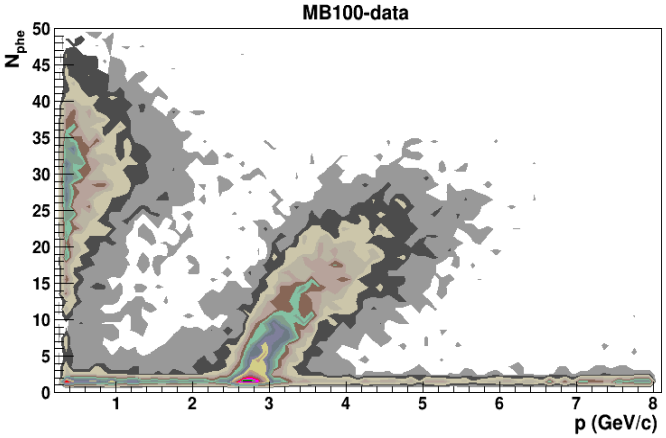

Figure 4.11: N_{phe} as a function of momentum for MB100. Pions are visible above $p >$ 2.6 GeV/c. Electron veto events are visible at below $p < 3$ GeV/c with $N_{phe} \sim 20 - 40$

of photoelectrons $N_{phe} \sim 20 - 40$ for events below the pions Cherenkov threshold. Therefore rejecting tracks in the momentum $p < 3$ GeV/c with $N_{phe} > 15$ (called e-veto cut) remove electrons from the data sample. Detailed analysis on electron veto cut and the Cherenkov detector response can be found in [71]. Combining beam time-of-flight system (TOFA, TOFB and TDS) and TOFW hits, the time-of-flight measurements of secondary tracks are used to estimate the velocity, β, for each track and to perform the separation of pions-kaon and pion-proton in the low momentum range up to 3.0 GeV/c. The resolution study of the β distribution separation on pions

from proton and kaons are described in the [59]. And also more detail description of the particle identification studies can be found in the reference [71].

4.4.1 Particle ID probabality

Combining the probability distribution of TOFW measurements and Cherenkov response, the particle ID probability is estimated by using Bayesian technique,

$$P_\alpha = P(\alpha \mid \beta, N_{phe}, p, \theta) = \frac{P(\beta, N_{phe} \mid \alpha, p, \theta) \cdot P(\alpha \mid p, \theta)}{P(\beta, N_{phe} \mid \pi, p, \theta) \cdot P(\pi \mid p, \theta) + P(\beta, N_{phe} \mid \mathrm{p}, p, \theta) \cdot P(\mathrm{p} \mid p, \theta)} \quad (4.1)$$

where $P(\beta, N_{phe} \mid \alpha, p, \theta) = P(\beta \mid \alpha, p, \theta) \cdot P(N_{phe} \mid \alpha, p, \theta)$ is the combination of TOFW-Cherenkov PDFs that contains the reconstructed velocity, β, and the number of associated photoelectrons, N_{phe}, for each α type track in the (p, θ) space. $P(\alpha \mid p, \theta)$ is the prior probability of the α type track in (p, θ) space. Assuming a no prior knowledge of the particle type, the prior probability of pions and protons is taken to be $P(\alpha \mid p, \theta) = 1$. After applying this simplifications on (4.1), the final particle ID estimator is written as a combination of TOFW probability, $P(\beta|\alpha, p, \theta)$, and the Cherenkov probability, $P(N_{phe}|\alpha, p, \theta)$, of α type track which are assigned to be independent,

$$P_\alpha = P(\alpha|\beta, N_{phe}, p, \theta) = \frac{P(\beta|\alpha, p, \theta) \cdot P(N_{phe}|\alpha, p, \theta)}{P(\beta|\pi, p, \theta) \cdot P(N_{phe}|\pi, p, \theta) + P(\beta|\mathrm{p}, p, \theta) \cdot P(N_{phe}|\mathrm{p}, p, \theta)} \quad (4.2)$$

This normalized probability (4.2) satisfy the condition of total probability $P_\pi + P_\mathrm{p} = 1$. The pions are selected by the cut $P_\pi > 0.6$ and the protons are selected by $P_\mathrm{p} > 0.6$ (or $P_\pi < 0.4$).

4.5 Interaction vertex reconstruction

The reconstruction of p-Be interaction is performed by taking account the projection of incoming beam and the outgoing particle tracks in x-z and y-z planes as shown in Fig. 4.12. As described in the Sec. 4.2.2 the MWPC is used to extrapolate the incoming

track to the center plane of the coordinate system. The outgoing track is determined from the downstream chambers. Fig. 4.12 shows the reconstructed positions and the angles of the incoming beam track and the outgoing secondary track while they pass through the center plane. General equations for x and y coordinates of the beam, (x_{beam}, y_{beam}), and x and y coordinates of the secondary track (x_{sec} , y_{sec}) are written as

$$x_{beam} = x_0 + z \cdot \tan(\theta_{x0}) \tag{4.3}$$

$$x_{sec} = x_4 + z \cdot \tan(\theta_{x4}), \tag{4.4}$$

and

$$y_{beam} = y_0 + z \cdot \tan(\theta_{y0}) \tag{4.5}$$

$$y_{sec} = y_4 + z \cdot \tan(\theta_{y4}). \tag{4.6}$$

where the various variables are defined in Fig. 4.12. In order to obtain the coordinates of the interaction vertex, we define the χ^2_{int} as a function of z as,

$$\chi^2_{int}(z) = \frac{(x_{beam} - x_{sec})^2}{\sigma^2_{sec-x}} + \frac{(y_{beam} - y_{sec})^2}{\sigma^2_{sec-y}}. \tag{4.7}$$

The best z coordinate of the interaction position, z_{int}, is obtained by minimizing $\chi^2_{int}(z)$. The comparison of reconstructed MC event vertices of 2.0 cm and 40.0 cm long targets with the generated vertices is shown in Fig. 4.13. The tails of the reconstructed distribution depend on the resolution of the reconstructed track. The correlation of the reconstructed and generated interaction vertices for MB100 MC events is shown in Fig .4.13. Fig. 4.14 shows the distributions of interaction vertices for real data of three targets: Be5 (2.0 cm target), MB50 and MB100.

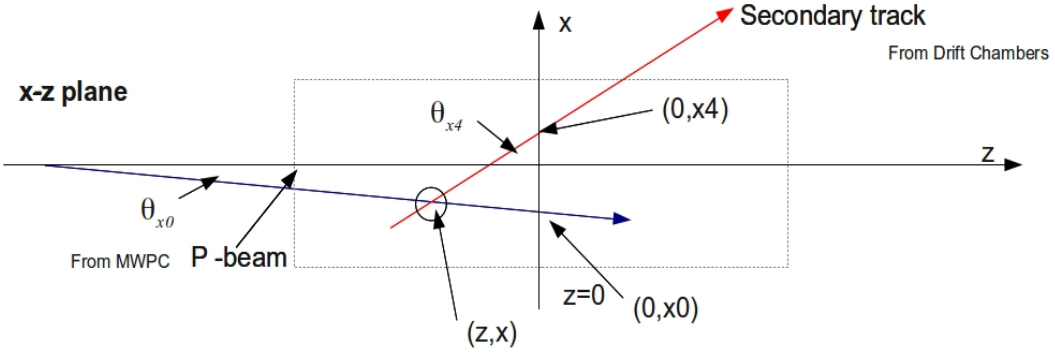

(a)

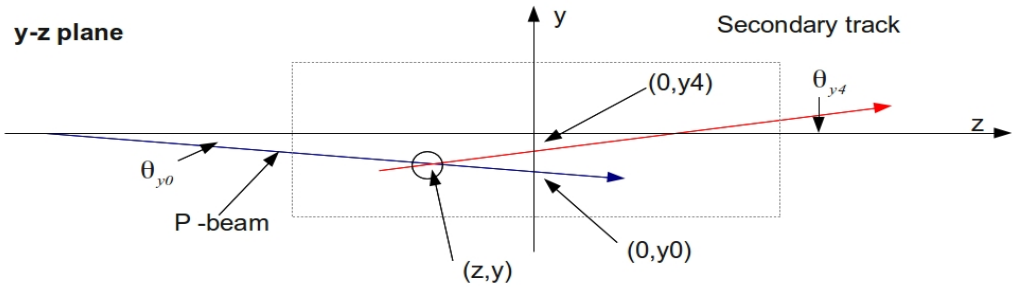

(b)

Figure 4.12: Schematic sketch of the reconstruction of interaction vertex of the event on (a) x-z and (b) y-z projection planes.

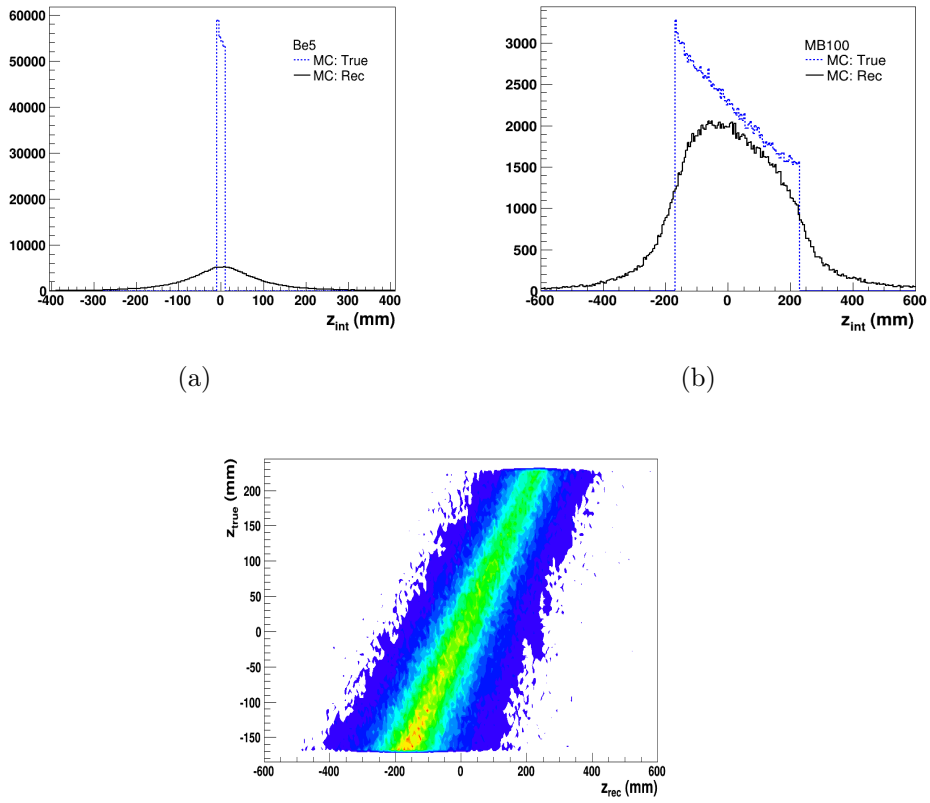

(a) (b)

(c)

Figure 4.13: The comparison of reconstructed interaction vertex (black solid lines) with the truth (blue dashed lines) for MC: Be5 (a) and MB100 (b). (c) The correlation of reconstructed vertex with truth vertex for MB100 MC.

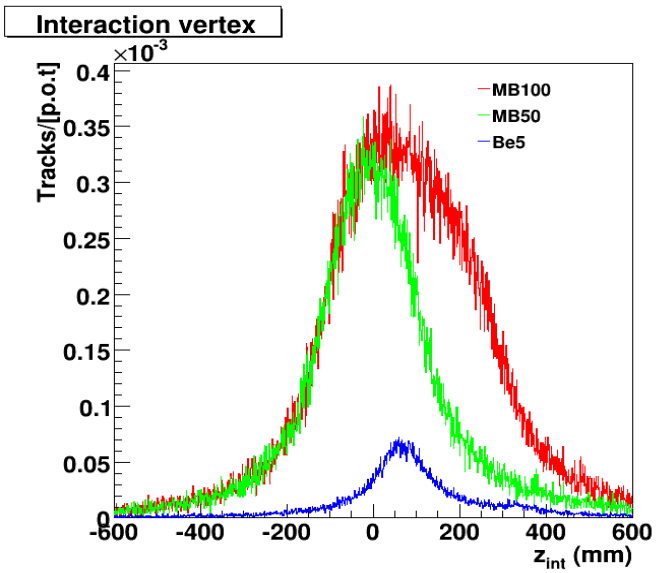

Figure 4.14: The reconstructed vertex from HARP data normalized to proton on target (POT): Red lines - MB100, green lines - MB50 and the blue lines - Be5.

Chapter 5

Particle production measurements

In this chapter, we describe the procedure used to measure secondary particle production cross section on short beryllium target (Be5) and the production yields of three targets (Be5, MB50 and MB100). The reconstructed variables of the VERTEX4 tracking algorithm are used for production measurements. The cross section measurements on short beryllium target (Be5) using VERTEX4 algorithm are compared with the cross section measured in VERTEX2 algorithm [59]. The results presented in the thesis on beryllium targets measurements are in the kinematic range (p $\in$[0.75,6.5] GeV/c and $\theta \in$[30,210] mrad) similar to the short target cross section analysis described in [59].

5.1 Unfolding production yield

The normalized double differential production yield, $N^{\alpha}(p,\theta)$, of secondary $\alpha = \pi^{\pm}, p$ type particles for MiniBooNE targets by 8.9 GeV/c incident protons is measured in the lab frame by using the expression:

$$\frac{d^2N^{\alpha}(p,\theta)}{dpd\Omega} = \frac{1}{\Delta p \cdot \Delta\Omega} \cdot \frac{1}{N_{POT}} \cdot M^{-1}_{p\theta\alpha\cdot p'\theta'\alpha'} \cdot N^{\alpha'}(p',\theta'), \tag{5.1}$$

where:

- $\Delta p = p_{i+1} - p_i$ and the $\Delta\Omega = 2\pi \cdot (\cos(\theta_j) - \cos(\theta_{j+1}))$ are the bin widths of i^{th} momentum bin and the solid angular width of the j^{th} angular bin respectively.
- N_{POT} is the number of protons on the target after the beam radius cuts.
- $M^{-1}_{p\theta\alpha\cdot p'\theta'\alpha'}$ is the correction matrix elements.
- $N^{\alpha'}(p', \theta')$ observed raw yield.

The non-interacted primary protons can interact with the material outside the target and can produce a background for the yield. Therefore to remove this effect we have subtracted the production yield measured from empty target data, $N^{\alpha'}_{E(norm)}$, which has been normalized[1] to the target P.O.T. This raw production yield can be written as $N^{\alpha'} = N^{\alpha'}_T - N^{\alpha'}_{E(norm)}$ after subtracting the normalized empty data from the target data, N_T. A details of the empty target data subtraction will be described in the Sec. 5.3. The empty target subtracted differential production yield in the lab frame can be written as,

$$\frac{d^2N^{\alpha}(p,\theta)}{dpd\Omega} = \frac{1}{\Delta p \cdot \Delta\Omega} \cdot \frac{1}{N_{POT}} \cdot M^{-1}_{p\theta\alpha\cdot p'\theta'\alpha'} \cdot \left[N^{\alpha'}_T(p', \theta') - N^{\alpha'}_{E(norm)}(p', \theta')\right]. \quad (5.2)$$

Here the true hadron yield $N^{\alpha}(p, \theta)$ in the lab frame is estimated by unfolding the observed yield $N^{\alpha'}(p', \theta')$ with the inverse correction matrix $M^{-1}_{p\theta\alpha\cdot p'\theta'\alpha'}$. This matrix can be split into a combination of several correction terms as follow:

$$\begin{aligned} M^{-1}_{p\theta\alpha.p'\theta'\alpha'} =& \frac{1}{\varepsilon^{e-veto}(p', \alpha')} \cdot \frac{1}{1 - \eta^{absorb}(p', \theta'_x, \theta'_y, \alpha')} \cdot M^{-1}_{p,p'}(\theta') \\ & \cdot (1 - \eta^{tert}(p', \theta'_x, \theta'_y, \alpha')) \cdot \frac{1}{\varepsilon^{acc}(\theta')} \cdot \frac{1}{\varepsilon^{rec}(p', \theta'_x, \theta'_y)} \cdot M^{-1}_{\alpha,\alpha'}(p). \end{aligned} \quad (5.3)$$

where these correction terms can be defined as:

- $\varepsilon^{e-veto}(p, \alpha)$: the efficiency of the electron veto cut which is used to remove electrons from the α-type tracks as described in the section 4.4;
- $\eta^{absorb}(p, \theta_x, \theta_y, \alpha)$: the fraction of the secondary α-type particles which are

[1] $N^{\alpha'}_{E(norm)} = N^{\alpha'}_E \cdot N^T_{POT}/N^E_{POT}$ where $N^{\alpha'}_E$ is the unnormalized empty target production.

absorption or decay before they hit the flight of time wall;

- $\eta^{tert}(p, \theta_x, \theta_y, \alpha)$: the fraction of tertiary particles generated from the re-interactions of α-type secondary particles[2];
- $M^{-1}_{p,p'}(\theta')$: momentum migration matrix which is used to correct for events that were generated in one momentum bin but reconstructed in another;
- $\varepsilon^{acc}(\theta')$: the geometric acceptance efficiency which is calculated analytically;
- $\varepsilon^{rec}(p', \theta'_x, \theta'_y)$: the total track reconstruction efficiency through out the chambers; and
- $M^{-1}_{\alpha,\alpha'}(p)$: the particle identification migration matrix.

The PID matrix for pion-proton migration can be written as,

$$M_{\alpha,\alpha'} = \begin{pmatrix} M_{\pi\pi} & M_{\pi p} \\ M_{p\pi} & M_{pp} \end{pmatrix}, \tag{5.4}$$

where $M_{\pi\pi}$ and M_{pp} are the pions and protons identification efficiencies respectively. $M_{\pi p}$ and $M_{p\pi}$ are the correction of the misidentification of pion as protons and the misidentification of proton as a pion respectively.
A detailed descriptions of each above correction terms will be discussed in the following subsections.

5.2 Unfolding cross section on Be5

The double differential production cross section of α-type secondary particles, $d^2\sigma^{\alpha}(p, \theta)/(dpd\Omega)$, for short target (Be5) by an incident proton beam of 8.9 GeV/c is obtained by multiplying the measured yield (Eq. 5.1) by a derived cross sectional factor for short target

[2]The re-interactions of secondaries with the matter outside the target volume is used for production rate measurements. The tertiary particle production from the target and the outside the target volume is used for production cross section measurements.

approximation as shown below:

$$\frac{d^2\sigma^{\alpha}(p,\theta)}{dpd\Omega} = \frac{A}{N_A \cdot \rho \cdot t} \cdot \frac{d^2N^{\alpha}(p,\theta)}{dpd\Omega}, \tag{5.5}$$

where:

- $A/(N_A.\rho)$ is the reciprocal of the number density of target nuclei ($\approx 1.2349 \times 10^{23}$ cm^{-3}), calculated from atomic mass of beryllium, $A = 9.012$ g/mole, of the target material, Avogadro's number, N_A, and the density of the target $\rho = 1.85$ $g \cdot cm^{-3}$.
- $t \approx 2.046$ cm is the thickness of the target along the beam axis.
- $d^2N^{\alpha}/(dpd\Omega)$ is the normalized differential secondary particle production yield as described in Eq. 5.2 except for the tertiary particle correction. The tertiary particle production from the target and the material outside the target volume is used to measure the production cross section measurements.

5.3 Empty target subtraction

The measurement of the interaction vertex in Be5 short target data shows a small peak at around 330 mm as shown in Fig. 5.1 (a). The locations of the apparatus material indicates that the small peak has been generated from the interaction of particles with the end plate of the inner field cage (see Fig. 5.2). Much more detail description of inner field cage could be obtained from the reference [67]. This end plate effect is clearly visible in the empty target run in Fig. 5.1 (b). Subtracting empty target data from the production can be eliminate this source of background data. Figure 5.1 (c) shows the distribution of the interaction vertex after subtracting empty target.

This empty target subtraction needs to perform with care. To perform the background subtraction correctly, first the empty target data needs to normalized to counted POT for the beam radius cuts used for each different targets. Next the proton attenuation through the target needs to be taken into account.

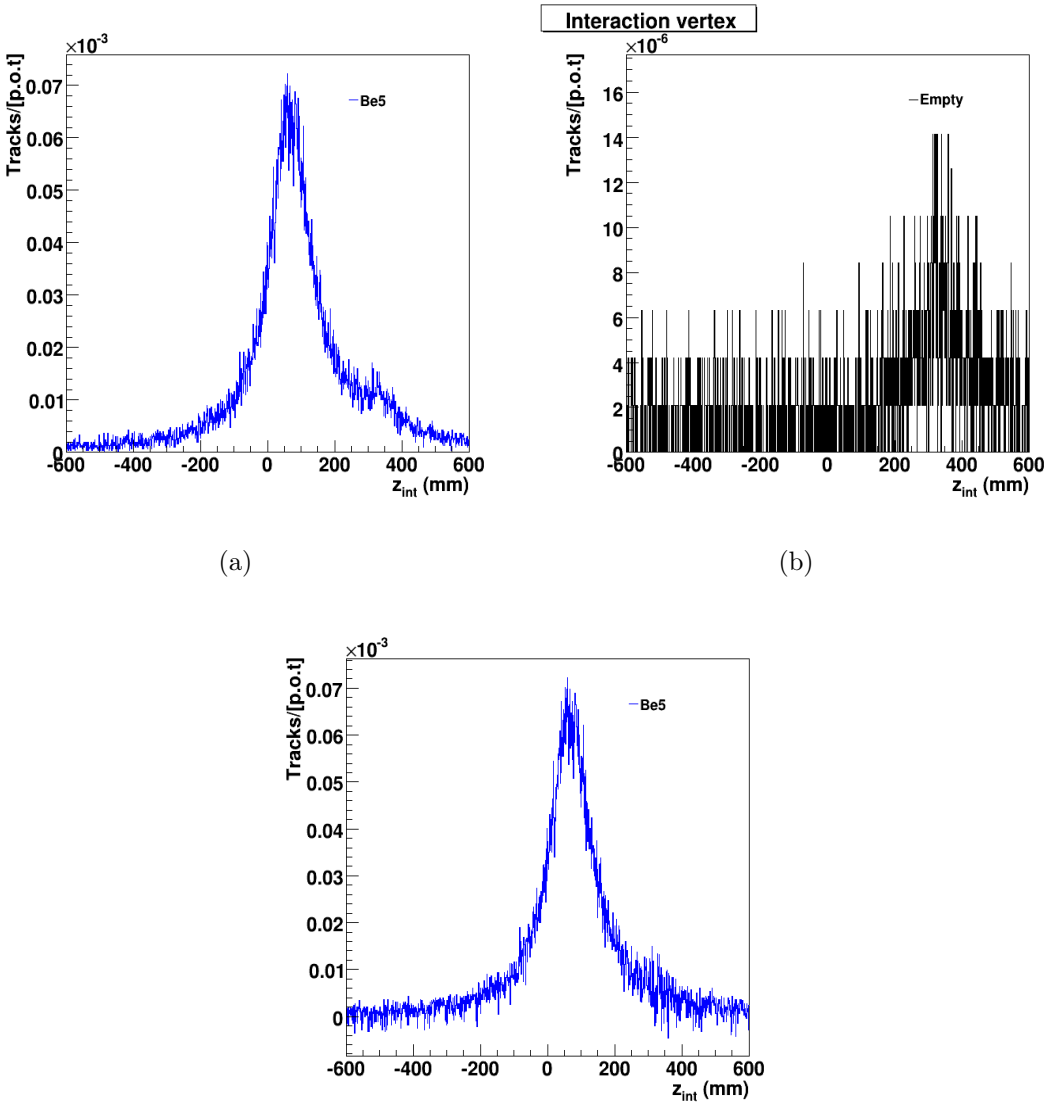

Figure 5.1: Reconstructed interaction vertex distributions of (a) Be5 data (b) empty target data and (c) Be5 data after subtracting empty measurements. The small peak at 330 mm is from the interactions of protons with the end plate of the inner field cage.

For 40.0 cm long (one interaction length) target, the fraction of the non interacted protons pass through the target is e^{-1}. Therefore 0.37 is used as the subtraction factor of the normalized empty data subtraction for MB100. In the same way we could estimate the subtraction factor for 20 cm long MB50 target by taking the proton attenuation as $e^{-0.5}$. The factor used for the subtraction of normalized empty data from the MB50 data analysis is 0.61. Since the short Be5 target has 2.0 cm (5%λ_I) thickness, the subtraction of the normalized empty data is performed without applying any fractional reduction. Figure 5.3 (a) and (b) distributions show the reconstructed interaction vertex of three beryllium targets before and after subtracting the empty target data.

5.4 Target shift

Comparing of the interaction vertex for real data with the MC shows a shift of the target position in data towards the forward spectrometer from the center plane ($z = 0$) as shown in Fig. 5.4. A set of MB100 MC events generated within the first half of the interaction vertex (-200.0 - 0.0 mm) is used for MB50 MC events. The precise measurements on this target shift is carried out by defining a $\chi^2(z_0)$ as in the Eq. (5.6) to match the shifted and normalized data distributions with MC distribution in each bin.

$$\chi^2(z_0) = \sum_j \frac{(DATA(z_j + z_0) - MC(z_j))^2}{\sigma_j^2(\text{DATA}) + \sigma_j^2(\text{MC})}, \tag{5.6}$$

where the σ_j^2(DATA) and σ_j^2(MC) are estimated by taking the sum of the squared errors in the bins.

To obtain the target shift, the $\chi^2(z_0)$ distribution is fitted using the equation:

$$F(z) = p_0 + p_2.(z - p_1)^2. \tag{5.7}$$

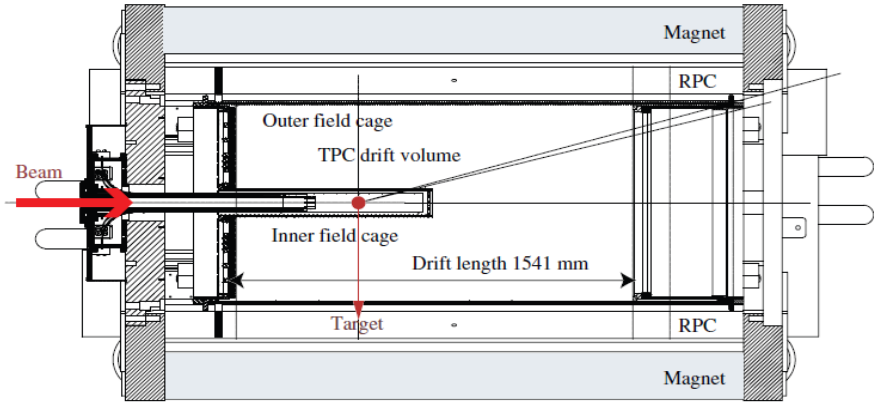

Figure 5.2: Schematic diagram of the inner field cage in the TPC drift volume.

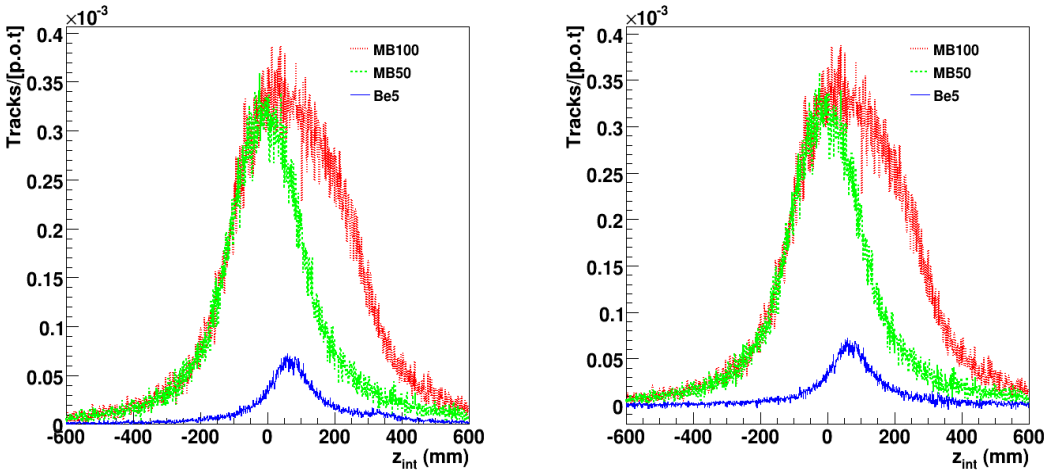

(a) (b)

Figure 5.3: Reconstructed interaction vertex distributions of three targets of MB100, MB50, and Be5 in dotted red, dashed green and solid blue colors respectively. (a) without subtracting empty data and (b) with subtracting empty data.

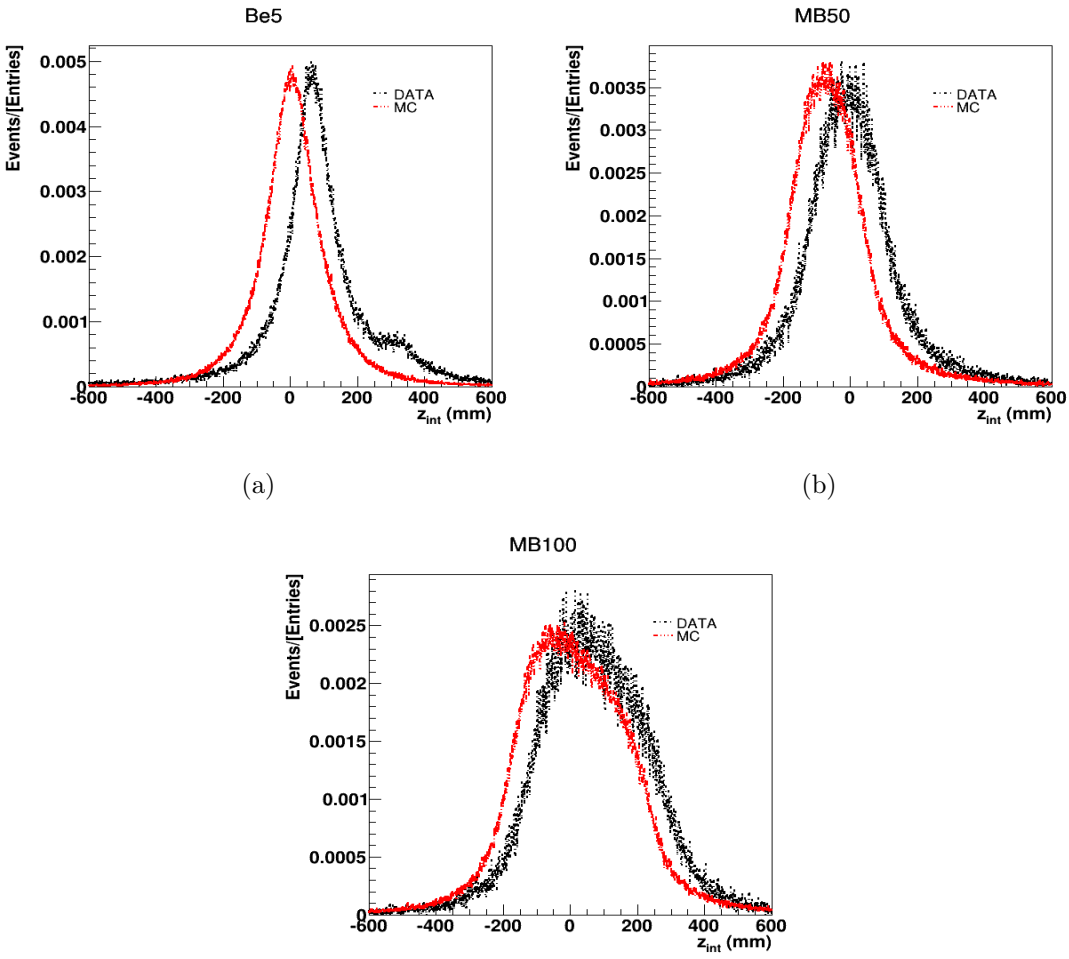

(a) (b)

(c)

Figure 5.4: Comparison of the the target position from DATA with MC in the reconstructed interaction vertex distribution. The red colored dash-dot-dot lines are for MC and the black colored dash-dot-dash distributions are for data. (a) short target Be5 (b) long target MB50 and (c) long target MB100.

In Fig. 5.5 shows the fitted χ^2 distribution of the target position shift by using MB100 long target data. Here the χ^2 minimum occurs at $z_0 = 65.34$ mm (p_1 in Table in Fig. 5.5).

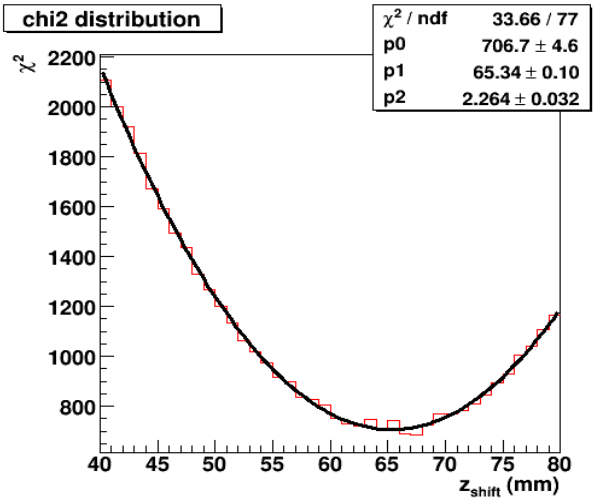

Figure 5.5: $\chi^2(z_0)$ distribution of target shift study in solid red and the fitted curve in solid black line.

The shifted data distributions are compared with the MC distributions in Fig. 5.6. Since the short target, Be5, cross section studies have been carried out by using VERTEX2-type center plane based tracks, a study is needed to determine the effect of the target shift on measurements. Taking the advantage of the independence of the VERTEX4 tracks from the center plane, the measurement of the ratio of $\tan\theta_{4x}$, angle from the VERTEX4 tracks, to $\tan\theta_{2x}$, angle from the VERTEX2 tracks, is used to estimate the correlation as a percentage of the angular shift. Fig. 5.7 (a) shows the ratio of $\tan\theta_{4x}$ to $\tan\theta_{2x}$ with the target interaction position. There is a dark area at around 300 mm that corresponds to the end plate of the field cage. In figure. 5.7 (b) shows the distribution of the ratio of $\tan\theta_{4x}$ to $\tan\theta_{2x}$ after subtracting the empty target data. This figure shows that the production angle is 2.6% low if the nominal target position is used as in the VERTEX2 analysis and by extension, the momentum is 2.6% high. Figure 5.7 (c) shows the 2D correlation distribution of the ratio of $\tan\theta_{4y}/\tan\theta_{2y}$ vs. the interaction vertex in the non-bending. The distribution of $\tan\theta_{4y}/\tan\theta_{2y}$ in Fig. 5.7 (d) shows the value of the ratio as 1.0 and that indicates

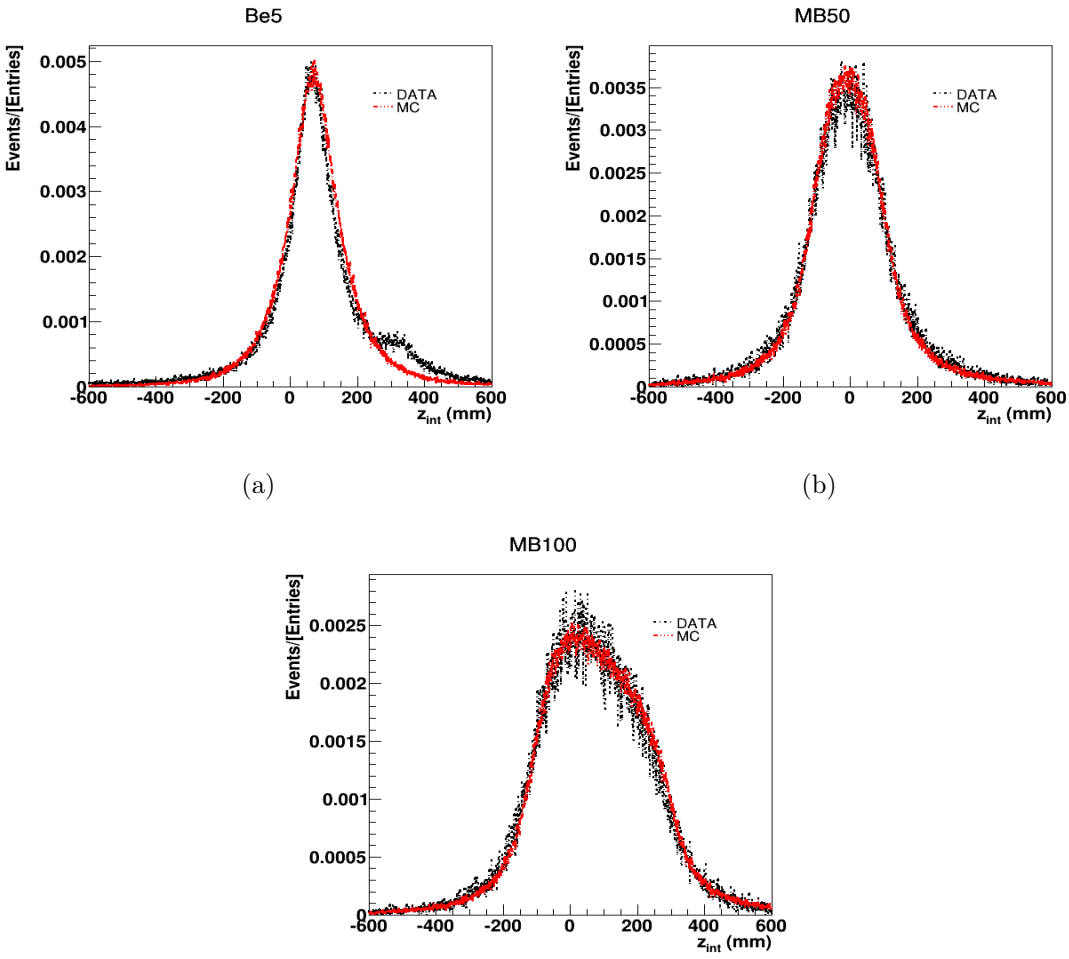

(a) (b)

(c)

Figure 5.6: Comparison of the position of the target from the 65.34 mm shifted MC with data in the interaction vertex distribution. Here the red colored dash-dot-dot lines are for MC and the black colored dash-dot-dash distributions are for data. (a) Short target, Be5 (b) long target MB50 and (c) long target MB100.

the target shift does not effect on the non-bending plane measurements.

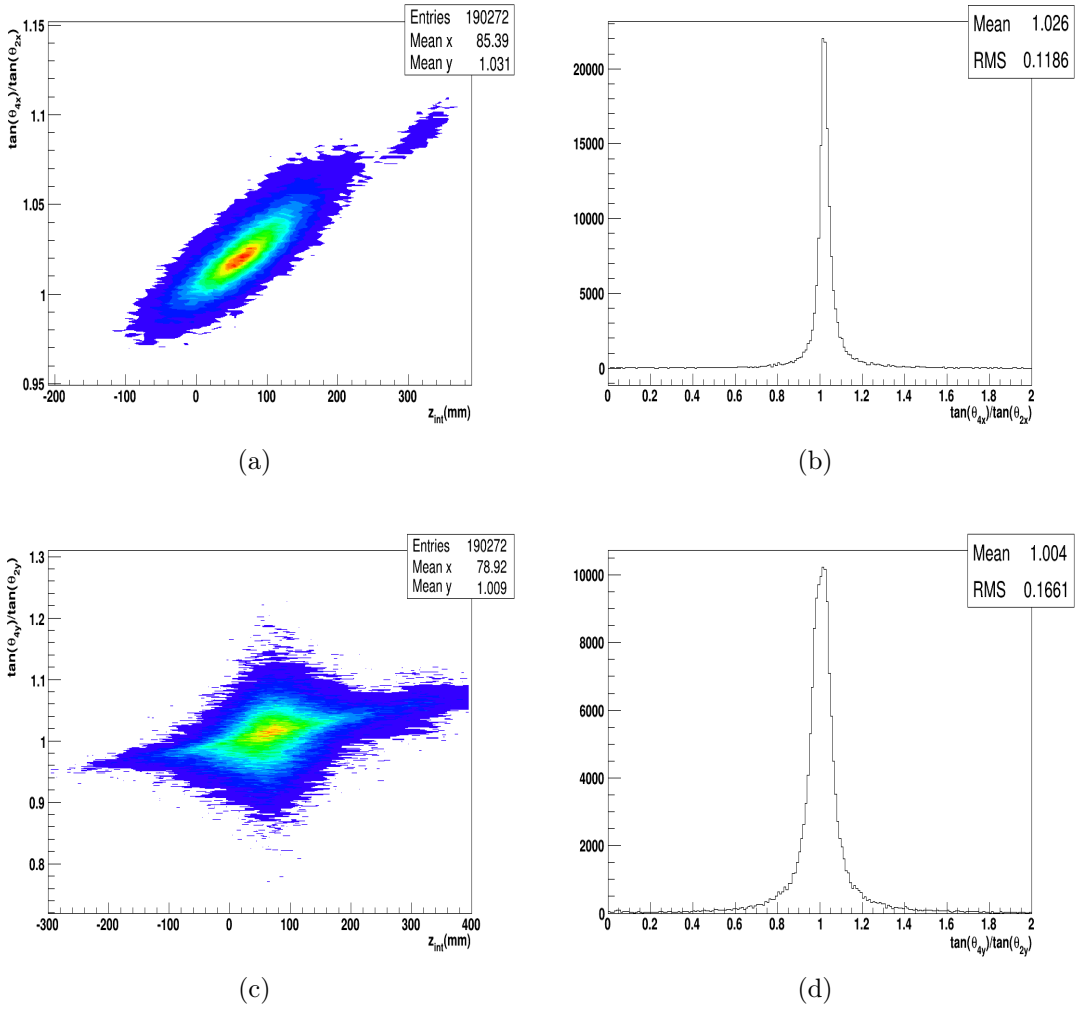

(a) (b)

(c) (d)

Figure 5.7: The target shift correlation study using Be5 short target. (a) The correlation of the ratio $\tan\theta_{4x}/\tan\theta_{2x}$ with the interaction vertex z_{int}. (b) The distribution of the ratio of $\tan\theta_{4x}/\tan\theta_{2x}$ after subtracting empty data. (c) The correlation of the ratio $\tan\theta_{4y}/\tan\theta_{2y}$ with the interaction vertex z_{int}. (d) The distribution of the ratio of $\tan\theta_{4y}/\tan\theta_{2y}$ after subtracting empty data.

5.5 Event selection

In the production yield and the cross section measurements, incoming beam protons are selected by testing the following criteria through the upstream detectors.

Each 8.9 GeV/c proton event must have

- time-of-flight counter hits in TOF-A, TOF-B and/ or TDS,

- Cherenkov detector counts in BCA and BCB,
- a beam position (extrapolated from the MWPC) at the nominal target center within the beam radius 1.0 cm for Be5 and 0.4 cm for MB50 and MB100.
- extrapolated beam angle less than 5 mrad, and
- no HALO detector hits

to accept the incoming beam event.

The angular condition guarantees that the beam particles are passing through the whole target volume.

The Forward Trigger Plane (FTP), a scintillation counter with a central hole of 60 mm diameter on it, was used in the trigger to select interacting events for the Be5 target run. The efficiency of FTP is above 99%. Figure 4.2 shows the location of the FTP trigger plane in the downstream of the TPC volume. For the Be5 run, an unbiased trigger was also defined. It was a trigger that required only an incident particle. This trigger was downscaled by a factor of 64. The number of protons on the target (POT) was taken as 64 times the number of unbiased triggers which passed the beam selection criteria. The POT for long targets is equivalent to the number of good protons passing through the target. The FTP counter was not used in the trigger for these data. The POT counts on short Be5 target and empty target data sets for 1.0 cm beam radius cut is shown in Table 5.1. Table 5.1 also shows the POT counts for

DATA	Proton on target
Be5 (1.0 cm)	13,074,880
Empty target (1.0 cm)	1,990,400
MB100 (0.4 cm)	622,791
MB50 (0.4 cm)	814,749
Empty target (0.4 cm)	475,776

Table 5.1: Number of protons on target for MB100, MB50, Be5 and empty targets with 0.4 cm and 1.0 cm beam radius cuts.

0.4 cm radius cut for the MB50, MB100, and empty target data sets.

5.6 Track selection

In the production yield measurements of three targets, the reconstructed VERTEX4 type secondary tracks should satisfy the following criteria:

i. a combination of the downstream track segments on NDC2 or back plane (NDC3, NDC4 or NDC5) and the NDC1 track segment which formed a track,

ii. number of hits in the road around the track in NDC2 ≥ 7,

iii. number of hits in the road around the track in NDC3-5 ≥ 6,

iv. number of hits in the road around the track in NDC1 ≥ 7 and the averaged χ^2 for hits with respect to the track in NDC1 chamber: $\chi^2_{NDC1} \leq 20$, and,

v. the match-χ^2_{v4} for the full track reconstruction by combining downstream 3D track on NDC1 3D segment ≤ 10.

These above cuts eliminate badly reconstructed tracks through the downstream chambers.

The VERTEX4 tracks reconstructed efficiency in the lower range $-10 < \theta_x < 10$ mrad was affected by primary beam hits on the NDC1 chamber. Therefore to eliminate these effects, positive tracks are selected in the region $-210 \leq \theta_x \leq -10$ mrad and negative tracks are selected in the region $10 \leq \theta_x \leq 210$ mrad. The yield measurements are corrected by taking account this angular selection into the geometric acceptance correction term. An angle cut of $|\theta_y| \leq \pm 80$ mrad cuts are applied for secondary track selections to eliminate the edge effects of the bending magnet and chambers on the non-bending plane. This is the same cut for short (5%) target data set that was used in [59] and [72]. Since the cutting boundaries of θ_y is a target length dependent factor, the starting position of long targets are used to estimate these θ_y boundary limits for long targets. Therefore the distance to the first chamber, $NDC1_z = 237.0$ cm from the center plane to the target z=0 plane, and the acceptance limits of $\theta_y = \pm 80$ mrad from the z= 0 plane which was selected for short target analysis are used to estimate the θ_y cuts on long targets. Since both MB50 and MB100 targets are starting at the

same position (10.5 cm upstream the target center) along the z-axis, the y direction angular cut of θ_y can be calculated as $\theta_y = \tan^{-1}(237 \times \tan(0.08)/247.5) \approx 0.0767$ rad.

- MB100 : $-76 \leq \theta_y \leq 76$ mrad,
- MB50 : $-76 \leq \theta_y \leq 76$ mrad,
- Be5 : $-80 \leq \theta_y \leq 80$ mrad.

Each secondary positive or negative track has to pass through this fiducial volume to be counted as a good track.

	Target radius cut : 1.0 cm	
Target	Be5	Empty
Proton on target	13,074,880	1,990,400
Total events processed	4,682,911	413,095
Events with accepted beam protons	2,277,657	200,310
Events with FTP trigger	1,518,683	91,690
Total good tracks in fiducial volume (pos)	158,287	4,674
Total good tracks in fiducial volume (neg)	19,510	481

Table 5.2: Total number of selected events for Be5 data and empty target data with 1.0 cm radius cut.

The short Be5 target data is measured with the 1.0 cm beam radius cut. Events are filtered with FTP trigger selection as described in the Sec. 5.5. Therefore the empty target data is also measured following the same Be5 short target event selection criteria. In Table 5.2 shows the total event selection for Be5 data and empty data. After applying above cuts, the number of filtered events are described in Table 5.3 on MB100, MB50 long MiniBooNE targets data and the empty target data for thick trigger selection.

5.7 Geometric Acceptance Correction

Figure 5.8 illustrates the 3D trajectory of the particle passing through the NDC1 chamber. Here z_{NDC1} is the distance between the $z = 0$ reference frame and the NDC1 chamber. According to the fiducial volume cuts, the 2D representation of tracks passing through the first chamber can be divided into three regions as shown

	Target radius cut : 0.4cm		
Target	MB100	MB50	Empty
Proton on target	622,791	814,749	475,776
Total events processed	2,820,668	2,776,711	413,095
Events with accepted beam protons	622,791	814,749	48,899
Total good tracks in fiducial volume (pos)	63,773	58,763	1,124
Total good tracks in fiducial volume (neg)	8800	7945	100

Table 5.3: Total number of selected events for MB100, MB50 data and empty target data with 0.4 cm radius cut.

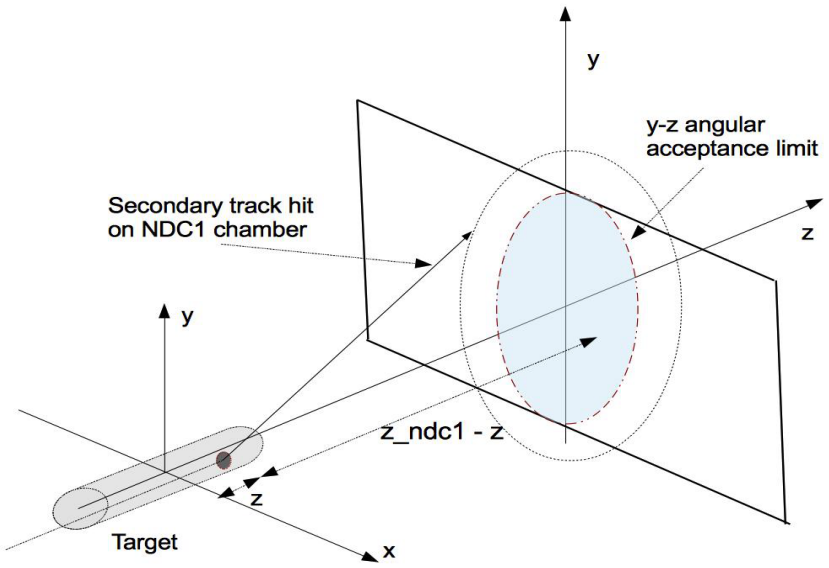

Figure 5.8: Schematic drawing of the geometric acceptance limit.

in Fig. 5.9. The limits of θ_y, θ_y^{min} and θ_y^{max} as shown in Fig. 5.9 are described in the Sec. 5.6 for different targets. The angular limit $\theta_x^{max} = -10$ mrad ($\theta_x^{min} = 10$ mrad) for positive (negative) tracks is used for all three targets. The angular limit of θ' in the region II is estimated by,

$$\begin{aligned} \theta' &= tan^{-1}\left(\frac{\sqrt{a_x^2 + a_y^2}}{z_{NDC1}}\right), \\ &= tan^{-1}\left(\sqrt{\tan^2\theta_x^{max} + \tan^2\theta_y^{limit}}\right). \end{aligned} \tag{5.8}$$

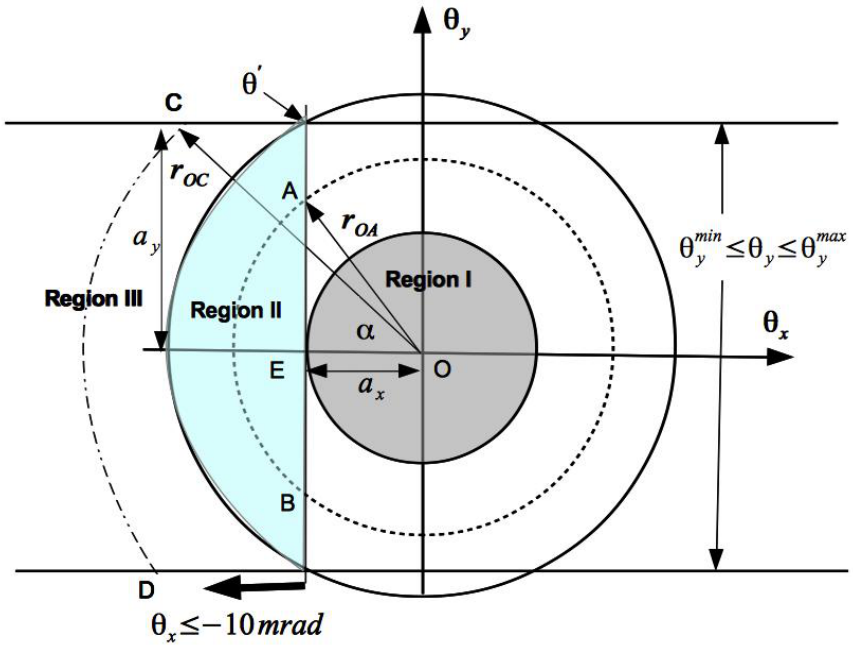

Figure 5.9: Schematic drawing of the geometric acceptance limits for positive particles. This limits can be divided into three regions: region I - $\theta < |\theta_x^{max}|$, region II : $|\theta_x^{max}| < \theta < \theta'$ and region III : $\theta \geq \theta'$.

region I : $\theta < |\theta_x^{max}|$

Particles with $\theta \leq 10$ mrad are not accepted into the yield measurement. Therefore the geometric acceptance correction, $\varepsilon_{acc} = 0$.

region II : $|\theta_x^{max}| < \theta < \theta'$

In this region the acceptance correction can be calculated by referring the dashed arc AB for general event hit on the plane. Now the angle $A\hat{O}E$ is defined as $\alpha_{A\hat{O}E} = \cos^{-1}(a_x/r_{OA})$ with the terms $r_{OA} = (z_{ndc1} - z) \cdot \tan\theta$ and $a_x = (z_{ndc1} - z) \cdot \tan|\theta_x^{max}|$. The acceptance correction ε_{acc} is calculated as,

$$\varepsilon_{acc} = \frac{1}{\pi} \cdot \cos^{-1}\left(\frac{\tan|\theta_x^{max}|}{\tan\theta}\right). \tag{5.9}$$

region III : $\theta \geq \theta'$

Any general event representation in this final region can be draw as the CD arc. Now the angle $C\hat{O}E$ is defined as $\alpha_{C\hat{O}E} = \sin^{-1}(a_y/r_{OC})$ with the terms of $r_{OC} = (z_{ndc1} - z) \cdot \tan\theta$ and $a_y = (z_{ndc1} - z) \cdot \tan\theta_y^{max}$. Now the acceptance correction term can be calculated as

$$\varepsilon_{acc} = \frac{1}{\pi} \cdot \sin^{-1}\left(\frac{\tan|\theta_y^{max}|}{\tan\theta}\right). \tag{5.10}$$

As a summery, the geometric acceptance correction can be written as:

$$\varepsilon_{acc}(\theta) = \begin{cases} \frac{1}{\pi} \cdot \cos^{-1}\left(\frac{\tan|\theta_x^{max}|}{\tan\theta}\right) & \text{for } |\theta_x^{max}| < \theta < \theta'; \\ \\ \frac{1}{\pi} \cdot \sin^{-1}\left(\frac{\tan|\theta_y^{max}|}{\tan\theta}\right) & \text{for } \theta \geq \theta'; \end{cases}$$

where the acceptance limit of $\theta_y^{max} = 0.076$ rad is used for MB100 and MB50 long targets and also $\theta_y^{max} = 0.08$ rad is used for Be5 short target. According to the above analytical description, the calculated geometric acceptance in the three regions for a randomly simulated event sample is shown in Fig. 5.10. This is simulated through a same geometric fiducial volume as the HARP detector volume.

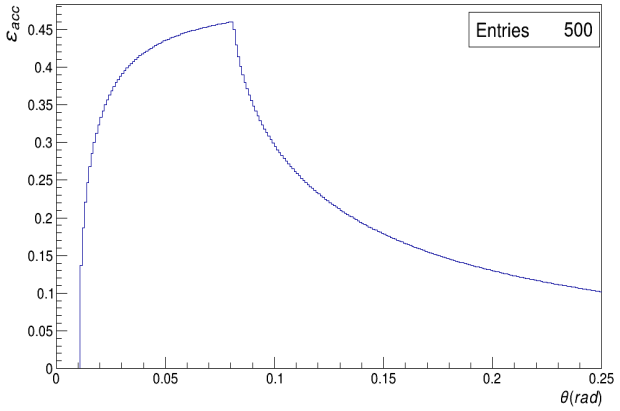

Figure 5.10: The variation of the calculated geometric acceptance correction as a function of angle for all three regions.

5.8 Track reconstruction efficiency

The performance of the chambers and the tracking algorithm is an important factor for the particle production yield measurements. The total track reconstruction efficiency depends on individual module efficiencies as described in this section.

In the track reconstruction algorithm as described in the Sec. 4.3.1, the NDC2 or the back plane (combination of NDC3-5 chambers) hits (or both hits) and the TOF wall hits are combined with the NDC1 measurements to reconstruct a secondary track. The criteria to accept as a good secondary track for the analysis is described in Sec. 5.6.

In general, the track reconstruction efficiency, ε^{track} is defined as a fraction of total number of particles that pass through the fiducial volume of the HARP spectrometers, N^{parts}, and the number of tracks which pass all track reconstruction algorithm in the parameter space p, θ_x and θ_y, N^{track}.

$$\varepsilon^{track}(p, \theta_x, \theta_y) = \frac{N^{track}(p, \theta_x, \theta_y)}{N^{parts}(p, \theta_x, \theta_y)}. \tag{5.11}$$

Here, all efficiencies are measured in the 3D parameter space (p, θ_x, θ_y) where θ_x and θ_y are the angular measurements in the horizontal plane and vertical plane respectively. Taking advantage of having two independent momentum reconstruction algorithms, VERTEX2 and VERTEX4, for secondary tracks, one type of track can be used as a control sample to measure the tracking efficiency through the chambers of the other type. Therefore, a good sample of VERTEX2 type tracks which have the matching $\chi^2_{v2} < 5$ and $r_{V2} < 200$ mm (reconstructed vertex radius of VERTEX2 tracks) is used to measure the chamber efficiencies of VERTEX4 type track reconstruction. In Fig. 5.11 shows the correlation between reconstructed VERTEX4 parameters with the reconstructed VERTEX2 parameters, (a) p_2 vs p_4, (b) θ_{x2} vs θ_{x4} and (c) θ_{y2} vs θ_{y4} measured in a good sample of VERTEX2 tracks of MB100 data. The following subsections detail the final track reconstruction efficiency combining individual chamber

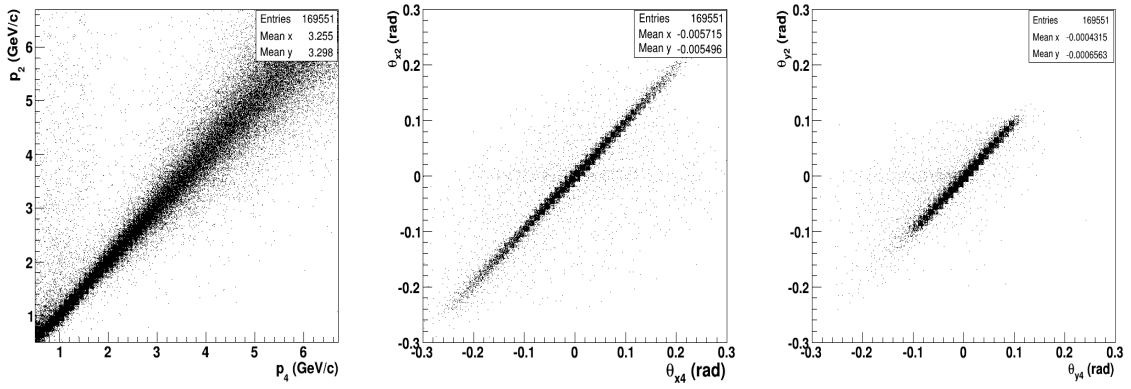

(a) (b) (c)

Figure 5.11: Correlation between reconstructed parameters from VERTEX2 and VERTEX4 algorithms. Here (a) p_2 vs p_4, (b) θ_{x2} vs θ_{x4} and (c) θ_{y2} vs θ_{y4}.

efficiencies. The chamber module efficiency measurements using negatively charged tracks for MB50 and MB100 targets are measured by combining the data sets of MB50 and MB100 to decrease the statistical uncertainty. The efficiency plots presenting in this chapter are 1D projections along the axis of p, θ_x and θ_y from the 3D efficiency measurements for all three targets.

5.8.1 NDC2 and back-plane efficiencies

Chamber efficiency calculations downstream of the bending magnet start by selecting a good sample of VERTEX2 tracks.

NDC2 chamber efficiency, ε^{NDC2}:

NDC2 chamber efficiency is estimated by taking the ratio of the number of reconstructed tracks which pass through the NDC2 and the back-plane[3] to the number of tracks pass through the the back-plane in the selected good VERTEX2 sample. Here the VERTEX2 sample is cleaned by making additional cuts: $\chi^2_{NDC1} \leq 20$ and the TOFW hit ($\beta > 0$).

[3]Track should reach NDC3 or NDC4 or NDC5 chambers

ε^{NDC2} is estimated as :

$$\varepsilon^{NDC2} = \frac{N[\exists p_2(\text{good}); \chi^2_{NDC1} \leq 20; \beta > 0; \exists \text{NDC2}_{seg}; \exists(\text{NDC3} \vee \text{NDC4} \vee \text{NDC5})_{seg}]}{N[\exists p_2(\text{good}); \chi^2_{NDC1} \leq 20; \beta > 0; \exists(\text{NDC3} \vee \text{NDC4} \vee \text{NDC5})_{seg}]}.$$

Here $\exists p_2(\text{good})$ assure that the control sample pass cuts $\chi^2_{v2} < 5$ and $r_{V2} < 200$ mm to select a good VERTEX2 sample.

The efficiency of NDC2 chamber measured with positively and negatively charged tracks as a function of momentum, θ_x and θ_y for targets of Be5, MB50 and MB100 are shown in Fig. 5.12 and Fig. 5.13 respectively. This shows a disagreement between data and MC in the low momentum range and the large angular range due to the edge effects.

Back plane efficiency, $\varepsilon^{back-plane}$:

The back-plane efficiency is estimated taking the ratio of number of VERTEX2 tracks which should pass through NDC2 and back-plane to the number of tracks which pass through NDC2. This is the opposite of the NDC2 efficiency measurement. Here also the VERTEX2 sample is selected with the $\chi^2_{NDC1} \leq 20$ and the TOFW hit ($\beta > 0$). The control sample is also satisfied the cuts as described in (5.8.1) to select the good VERTEX2 track sample. In addition to that the track needs to have a signal in the electromagnetic calorimeter (ECAL) to confirm the track pass the back plane of chambers. The numerator of the efficiency is the number of events with any back plane chamber segment with the cut of number of hits in the road around the track, $hit_{NDC3-5} \geq 6$:

$$\varepsilon^{back-plane} = \frac{N[\exists p_2(\text{good}); \chi^2_{NDC1} \leq 20; \beta > 0; \exists \text{NDC2}_{seg}; \exists(\text{NDC3} \vee \text{NDC4} \vee \text{NDC5})_{seg}]}{N[\exists p_2(\text{good}); \chi^2_{NDC1} \leq 20; \beta > 0; \exists(NDC2)_{seg}]}.$$

In the figure 5.14 and 5.15 show the back-plane efficiency measured as a function of 3D parameter (p, θ_x, θ_y) for all three targets with positively and negatively charged tracks respectively.

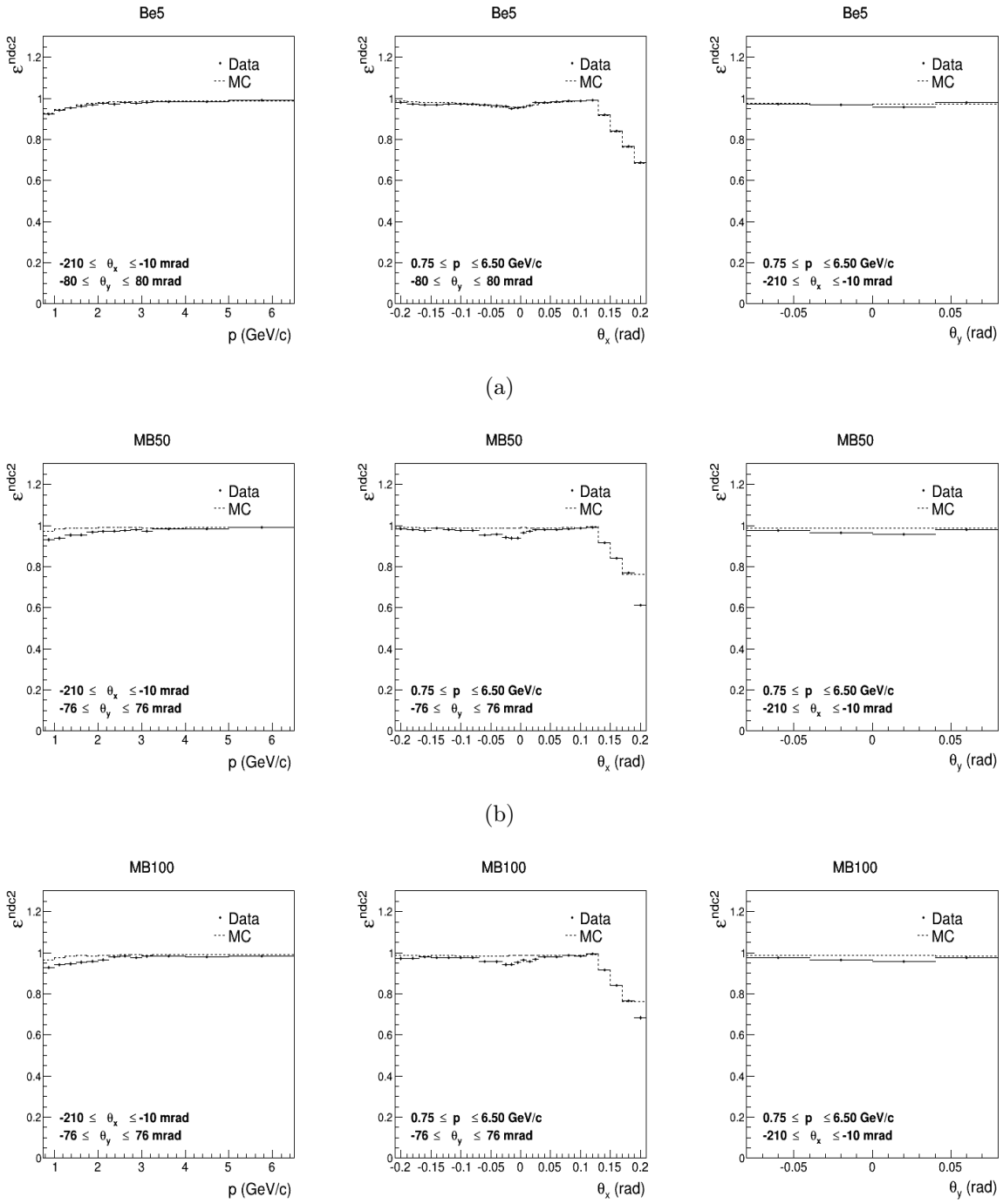

Figure 5.12: NDC2 chamber efficiency measured by positively charged tracks as a function of momentum, p (left), θ_x (middle) and θ_y (right). The dark line represent the MC efficiency which compare to the dark dotted DATA estimation. (a) is representing the Be5, the (b) row is from MB50 and the (c) row is from MB100 measurements.

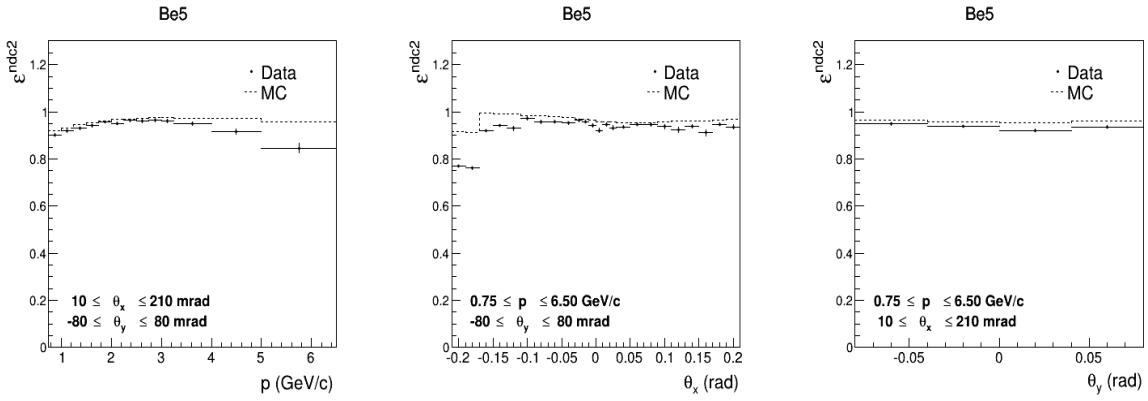

(a)

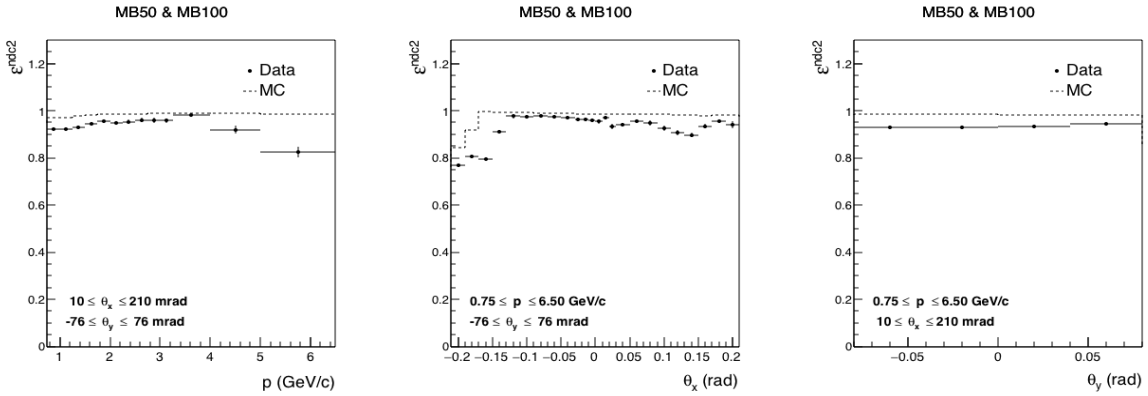

(b)

Figure 5.13: NDC2 chamber efficiency measured by negatively charged tracks as a function of momentum, p (left), θ_x (middle) and θ_y (right). The dark line represent the MC efficiency which compare to the dark dotted DATA estimation. Top row represents the Be5 and the bottom row is from the combination of MB50 and MB100 measurements.

5.8.2 VERTEX4 efficiency

The first chamber measurements of the forward spectrometer (NDC1) has been affected by the primary proton beam. Therefore the sample needs to be carefully selected to avoid contamination. The VERTEX4 efficiency is measured by using a control sample of VERTEX2 tracks. The computation of the efficiency is performed by counting the number of tracks which satisfy the matching condition of VERTEX4 algorithm in the selected VERTEX2 track sample.

First, a clean VERTEX2 control sample is obtained by selecting cuts $\chi^2_{v2} \leq 5$,

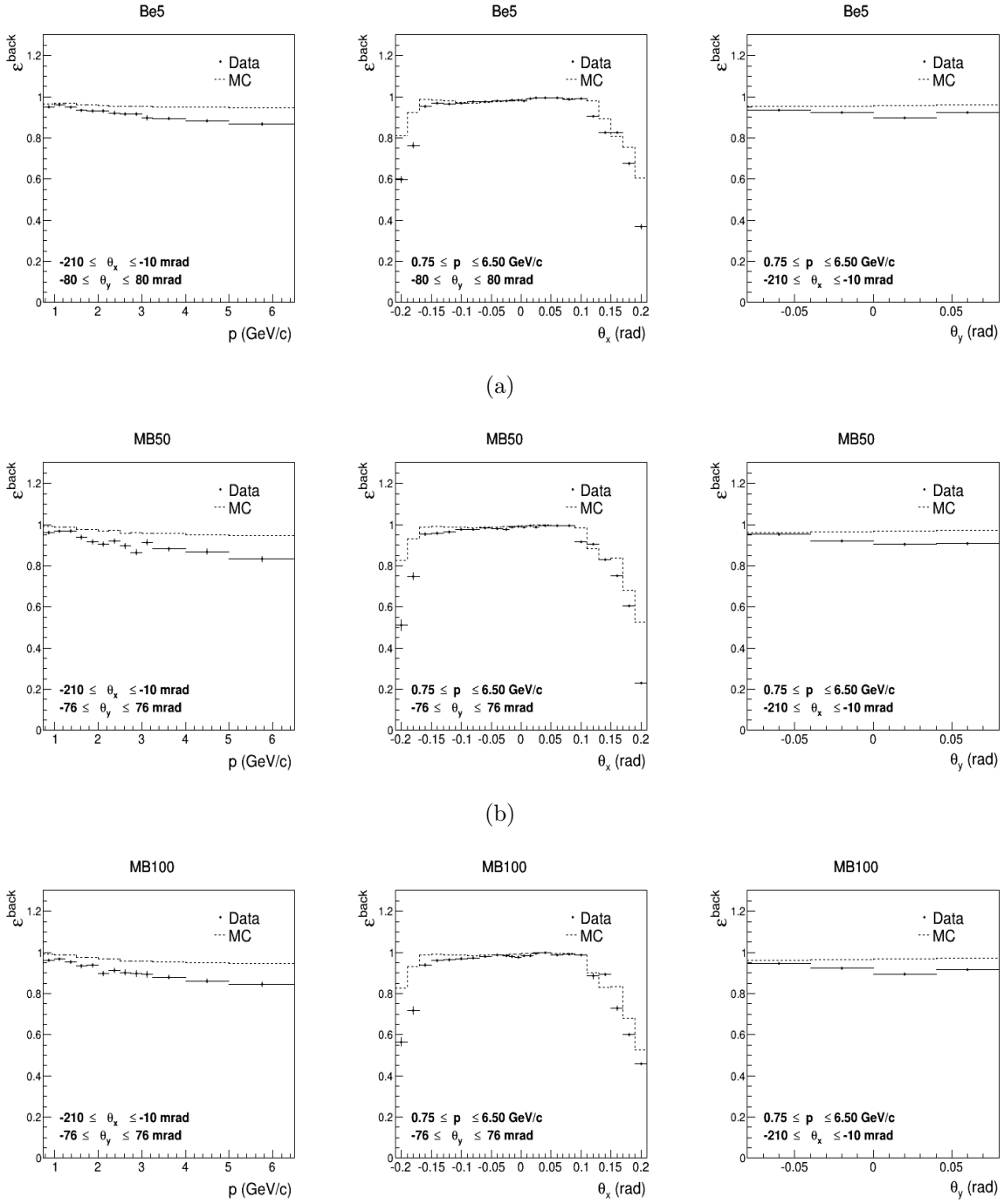

Figure 5.14: Back-plane efficiency from positive tracks as a function of p (left), θ_x (middle) and θ_y (right). The dark line represent the MC estimation compare to the dark dotted DATA estimation. (a) is representing the Be5, the (b) row is from MB50 and the (c) row is from MB100 measurements.

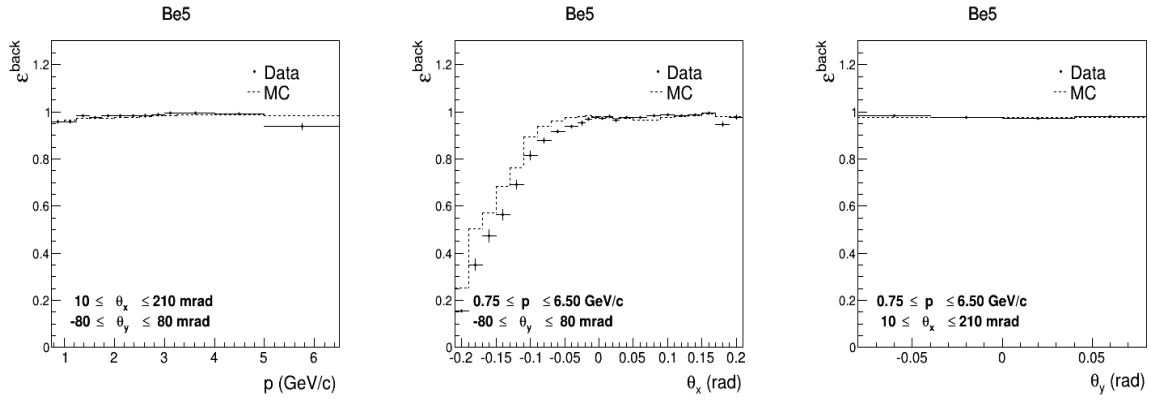

(a)

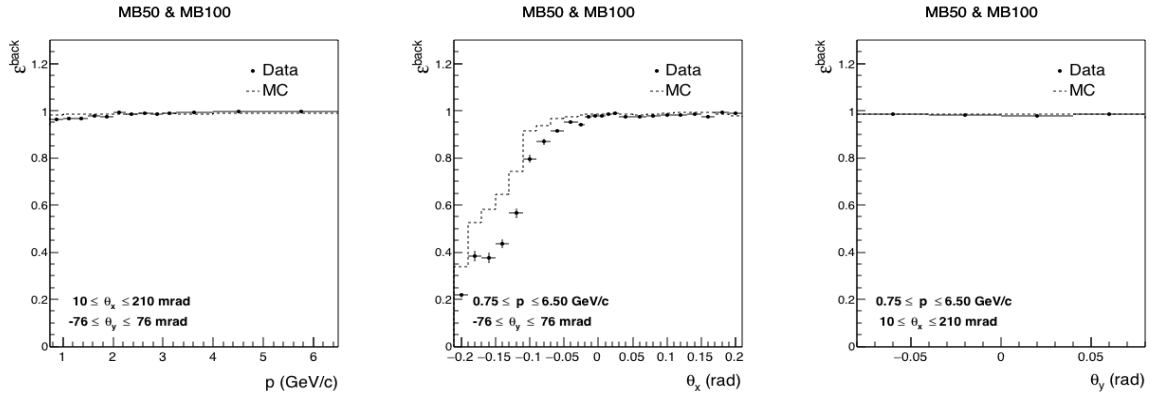

(b)

Figure 5.15: Back-plane efficiency from negative tracks as a function of p (left), θ_x (middle) and θ_y (right). The dark line represent the MC estimation compare to the dark dotted DATA estimation. Top row is representing the Be5 and the bottom row is from the combination of MB50 and MB100 data.

$r_{V2} \leq 200$ mm and requiring NDC2 and back plane hits. The averaged χ^2_{NDC1} relative to reconstructed hits in NDC1 chamber from Be5 data is compared with data and the background free Monte Carlo distributions in Fig. 5.16. This comparison shows the MC distribution is falling down faster than data in $\chi^2_{NDC1} > 20$. This effect is recognized as a background in the data due to the primary beam effect. To estimate this background in addition to the first cut on VERTEX2 sample was made the sample should have $\chi^2_{NDC1} \leq 20$ or $\chi^2_{V4} \leq 10$. In Fig. 5.16 (b) shows the VERTEX2 control sample distribution (black) after applying $\chi^2_{NDC1} \leq 20$ or $\chi^2_{V4} \leq 10$ cut and that is compared with the distribution of before cut (blue).

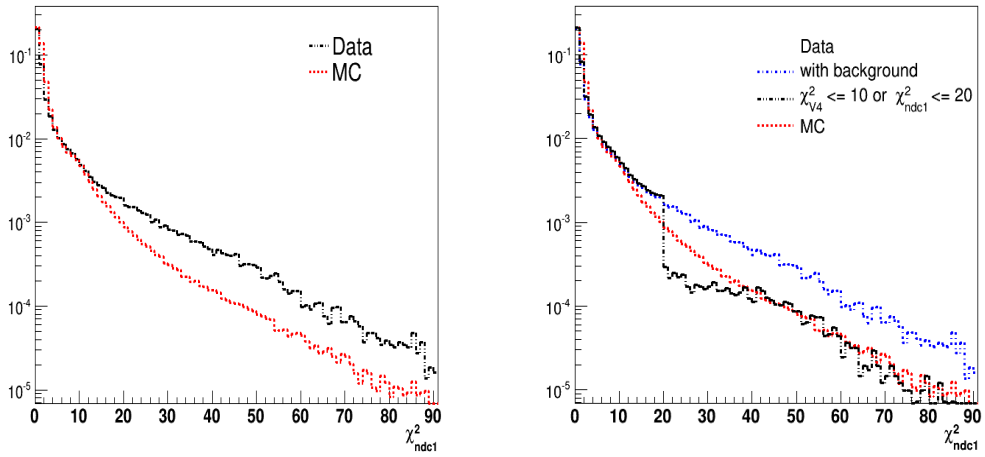

(a) (b)

Figure 5.16: The normalized χ^2_{NDC1} relative to reconstructed hits in NDC1 from Be5 data has been plotted in the log scale. (a) The comparing the black dash-dotted data distribution with the red dotted MC distribution, data shows a background in $\chi^2_{NDC1} > 20$ due to the primary beam effect. (b) The dash-dotted black distribution shows the controlled sample data after applying $\chi^2_{NDC1} \leq 20$ or $\chi^2_{V4} \leq 10$ and that compared with the distribution of before cuts as blue dotted.

The numerator of the efficiency measurement is the subset of the above controlled sample that satisfy the VERTEX4 good track selection condition. Furthermore this sample subset which has track segments on NDC1 and also cuts $\chi^2_{NDC1} \leq 20$ and $\chi^2_{V4} \leq 10$ and the number of hits in the road around the track on NDC1, $hr_{NDC1} \geq 7$, is the accepted numerator for the VERTEX4 efficiency calculation.

$$\varepsilon^{VERTEX4} = \frac{N[\exists p_2(\text{good}); \exists p_4; \chi^2_{NDC1} \leq 20; \chi^2_{V4} \leq 10; hr_{NDC1} \geq 7]}{N[\exists p_2(\text{good}); (\chi^2_{NDC1} \leq 20 \vee \chi^2_{V4} \leq 10)]}$$

The VERTEX4 efficiencies measured with positively and negatively charged tracks for all three targets are shown in Fig. 5.17 and Fig. 5.18 respectively. The VERTEX4 efficiency is affected by the inefficiency of the NDC1 chamber at around $\theta_x = 0$ due to the primary beam as shown in the middle of these figures. This dip also affects the overall efficiency on other distributions of p and θ_y as shown in the left and right figures respectively.

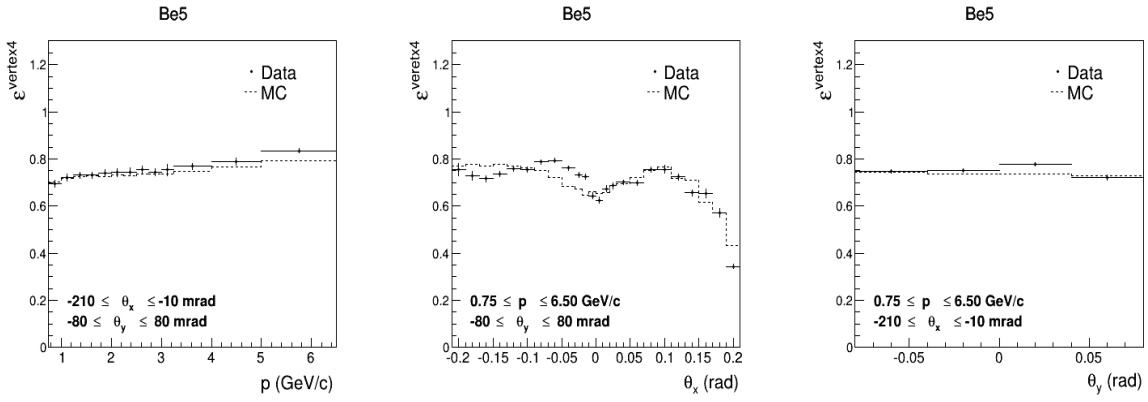

(a)

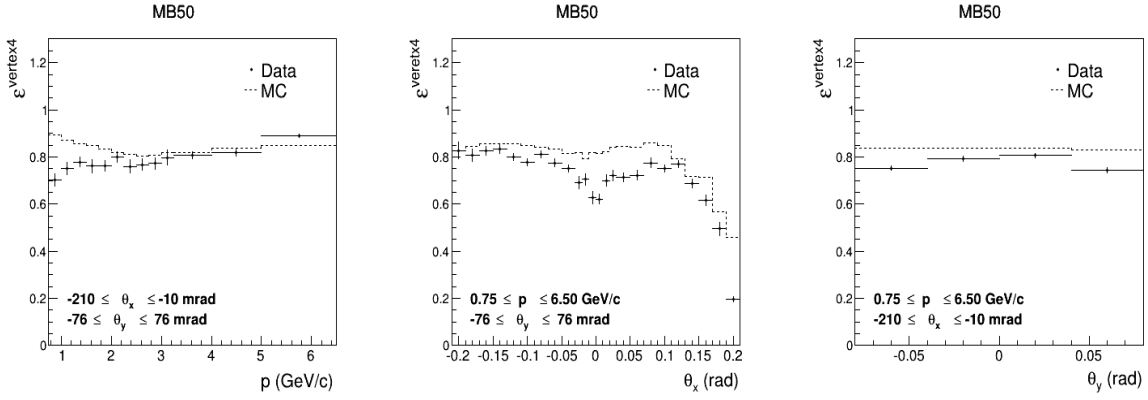

(b)

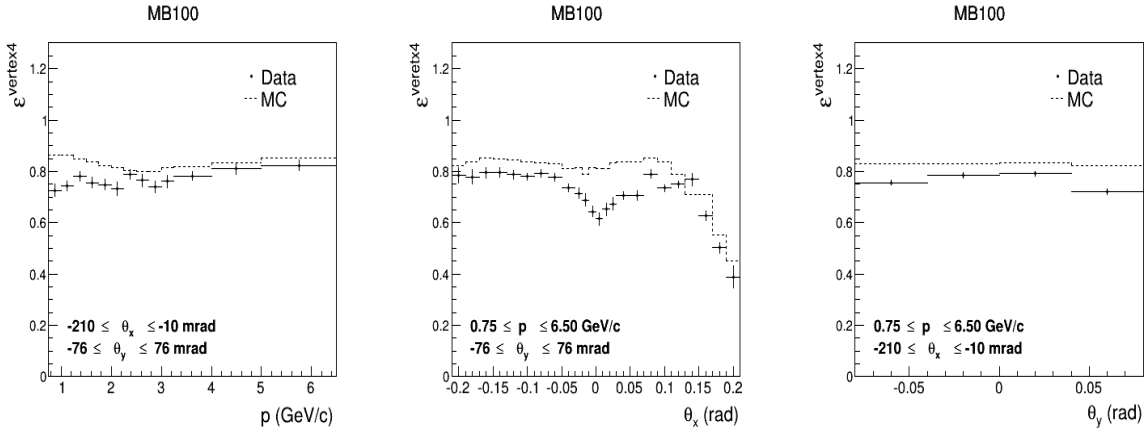

(c)

Figure 5.17: VERTEX4 efficiency from positive tracks as a function of p (left), θ_x (middle) and θ_y (right). The dark line represent the MC estimation compare to the dark dotted DATA. (a) is representing the Be5, the (b) row is from MB50 and the (c) row is from MB100 measurements.

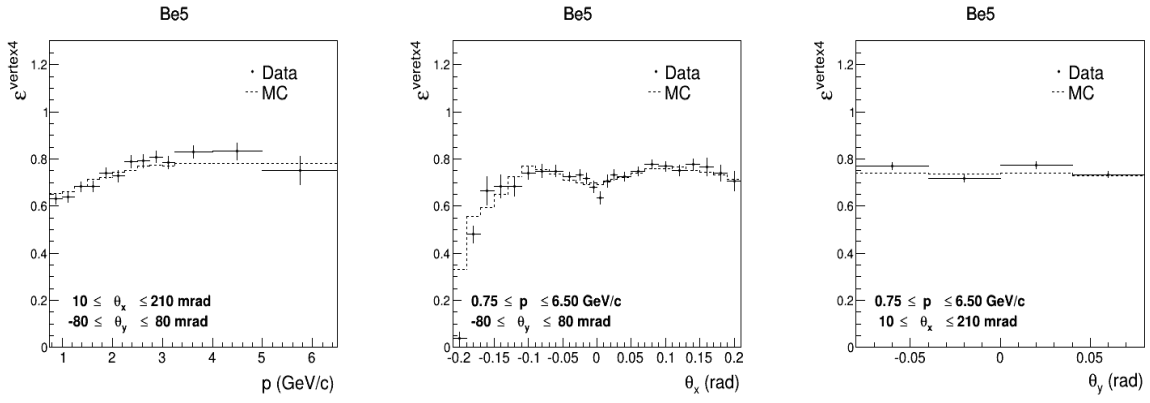

(a)

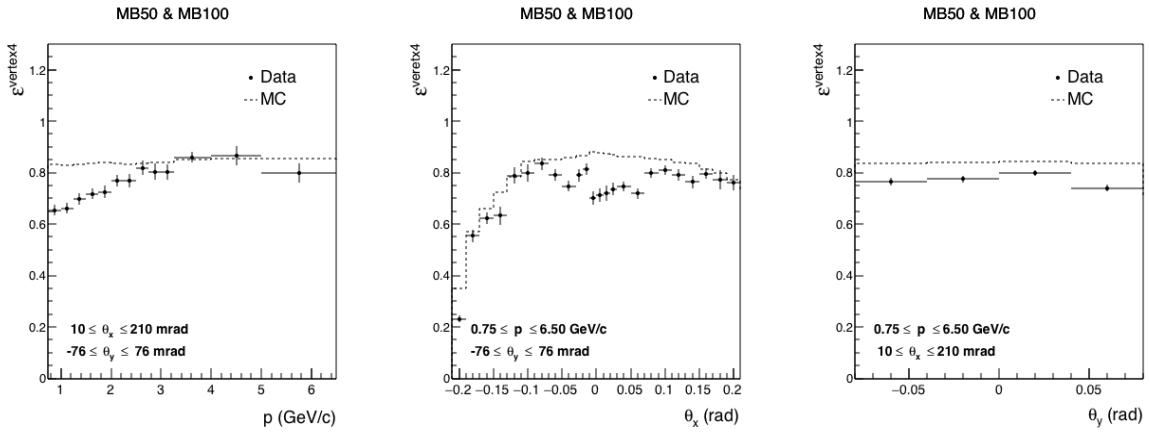

(b)

Figure 5.18: VERTEX4 efficiency from negative tracks as a function of p (left), θ_x (middle) and θ_y (right). The dark line represent the MC estimation compare to the dark dotted DATA. Top row is representing the Be5 and the bottom row is from the combination of MB50 and MB100 data.

5.8.3 Total reconstruction efficiency

The complete reconstruction efficiency of secondary tracks depends on several pieces of chamber efficiencies as described in the above sections. Therefore we can write the ε^{track} as:

$$\varepsilon^{track} = \varepsilon^{down}.\varepsilon^{vertex}. \tag{5.12}$$

The downstream track reconstruction efficiency, ε^{down}, is defined in terms of the efficiencies of NDC2 and the back-plane which is the combination of NDC3,NDC4 and NDC5 chambers.

$$\varepsilon^{down} = \varepsilon^{NDC2} + \varepsilon^{back-plane} - \varepsilon^{NDC2} \cdot \varepsilon^{back-plane} \tag{5.13}$$

where the subtraction of $\varepsilon^{NDC2} \cdot \varepsilon^{back-plane}$ term is correcting the double counting of the events that belongs to ε^{NDC2} and $\varepsilon^{back-plane}$ sets. The downstream track reconstruction efficiency measured with positively and negatively charged tracks as a function of variable p, θ_x and θ_y are shown in Fig. 5.19 and Fig. 5.20 respectively. The downstream efficiency shows high efficiency except at larger angles where the acceptance is limited.

The total track reconstruction efficiency is measured by combining ε^{down} with the VERTEX4 efficiency in the upstream as described in Sec. 5.12. Figure 5.21 shows the the 1D projections of total positively charged track reconstruction efficiency along the coordinates of p, θ_x and θ_y. Following the same procedure, Fig. 5.22 shows the projections of total negatively charged track reconstruction efficiencies for all three targets.

In the process of the secondary particle identification, particles should have to pass through the time-of-flight wall, TOFW. The reconstruction of track hits (x, y) on TOFW is performed by using Kalman Filter fitting package. The studies on particle velocity, β, show that there exists a non-Gaussian tail in the β distribution. This non-Gaussian tail of greater than 5σ from the peak which contains pions and protons could not use for particle identification. These events are called $\beta - outliers$. Studies shows that many of $\beta - outliers$ are generating low signal in the slab. The number of minimum ionizing particles, MIPs, distribution for MB100 target data is shown in the left panel of Fig. 5.23. Since $\beta - outliers$ are associating lower MIPs, they can reduce by selecting tracks of $MIPs > 1.5$. Furthermore the best match-$\chi^2 \leq 6$ (see the right panel of Fig. 5.23) cut of reconstructed position of the track along the scintillator and the actual hit on TOFW scintillator slab is also applied to enhance the quality of the

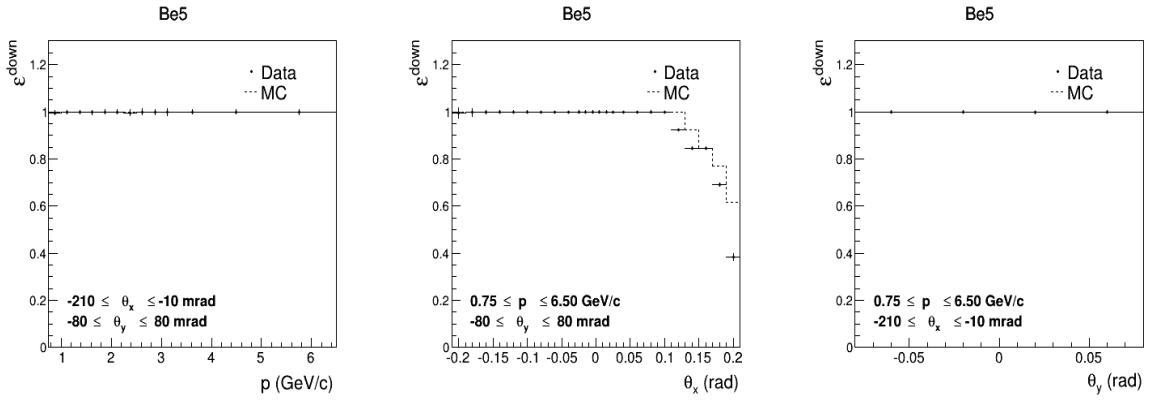

(a)

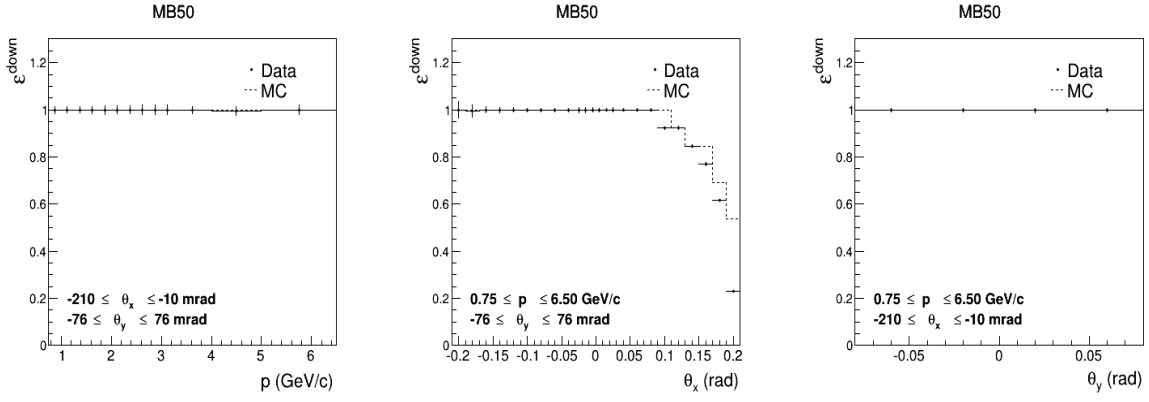

(b)

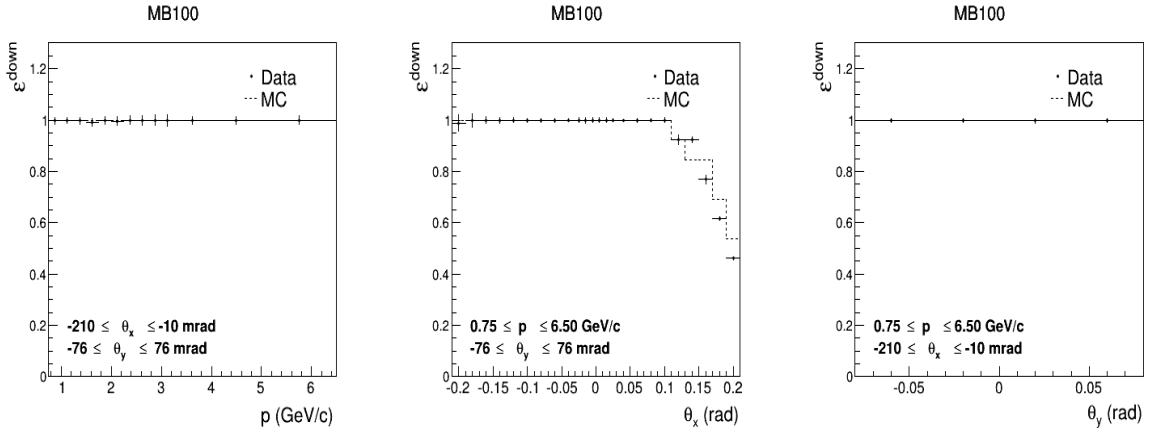

(c)

Figure 5.19: Downstream efficiency from positive tracks as a function of p (left), θ_x (middle) and θ_y (right). The dark line represent the MC estimation compare to the doted DATA. (a) is representing the Be5, the (b) row is from MB50 and the (c) row is from MB100 measurements.

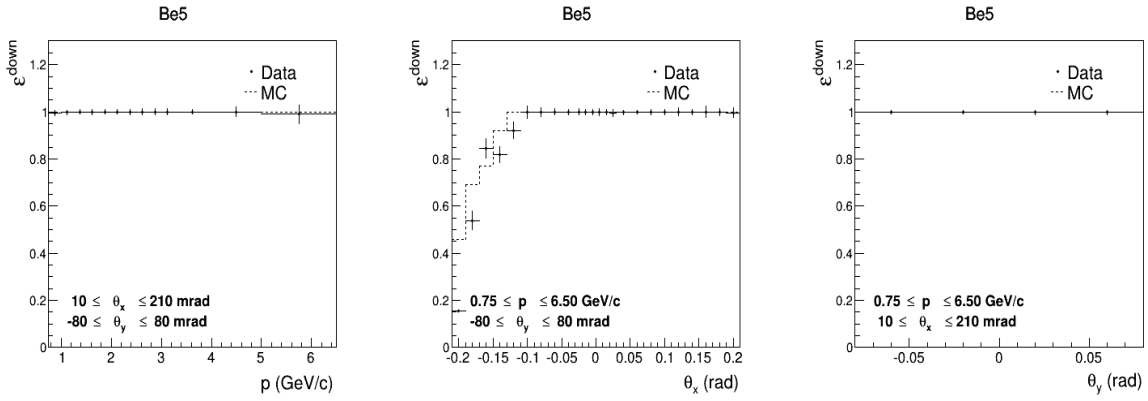

(a)

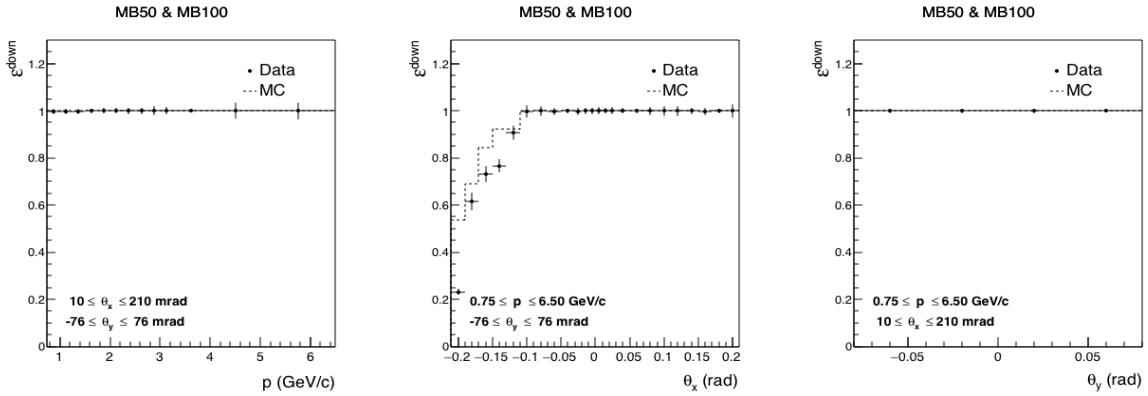

(b)

Figure 5.20: Downstream efficiency from negative tracks as a function of p (left), θ_x (middle) and θ_y (right). The dark line represent the MC estimation compare to the doted DATA. Top row is representing the Be5 and the bottom row is from the combination of MB50 and MB100 measurements.

TOFW measurements. Here, the two PMT timing information is used to obtain the position of the particle hit on the slab.

The loss of small amount of tracking efficiency of secondaries through the TOFW hit selection criteria is corrected by defining the complete reconstruction efficiency calculation.

$$\varepsilon^{recon} = \varepsilon^{track} \cdot \varepsilon^{TOF-match}. \tag{5.14}$$

To compute the TOF-match efficiency, $p2$ tracks those pass the back-plane and $\chi^2_{v2} \leq 5$ count in the denominator and any track in the sample that show up hits on TOF wall

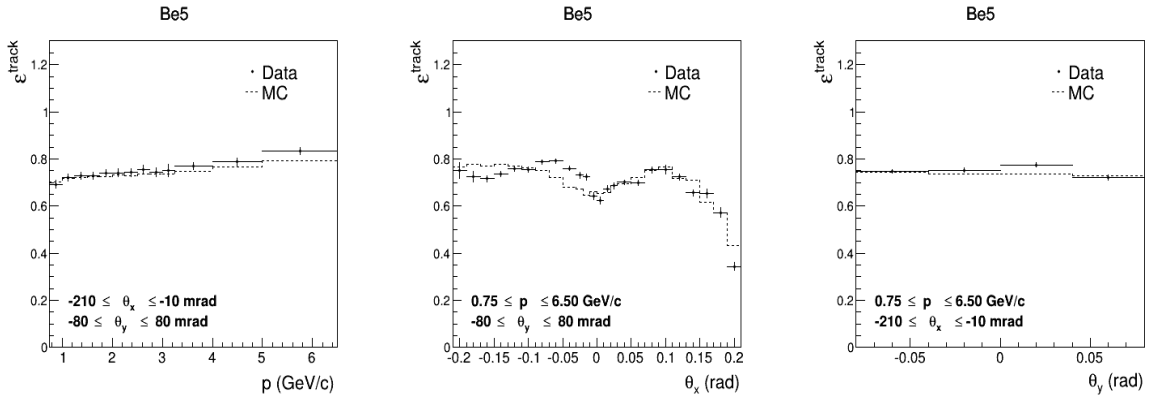

(a)

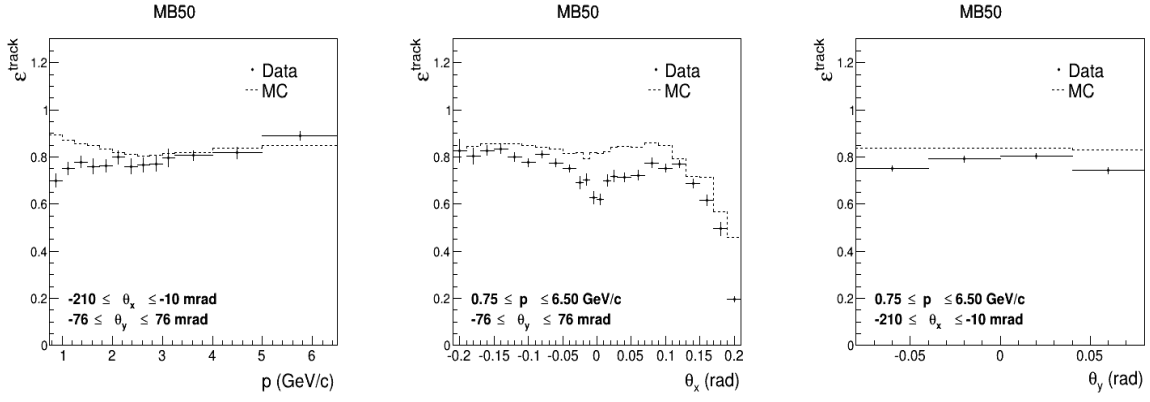

(b)

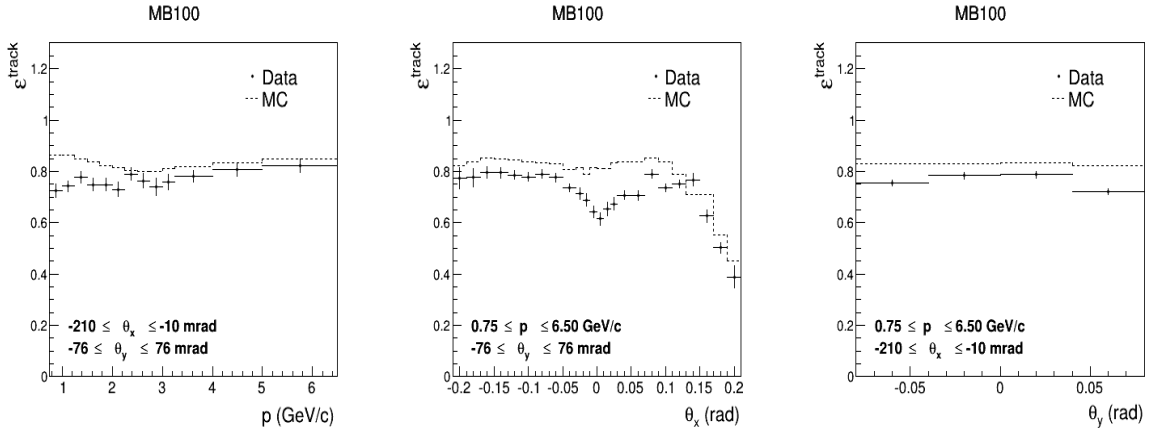

(c)

Figure 5.21: Total track reconstruction efficiency by VERTEX4 as a function of p (left), θ_x (middle) and θ_y (right). The dark line represent the MC calculation compare to the dark dotted DATA calculation. (a) is representing the Be5, the (b) row is from MB50 and the (c) row is from MB100 measurements.

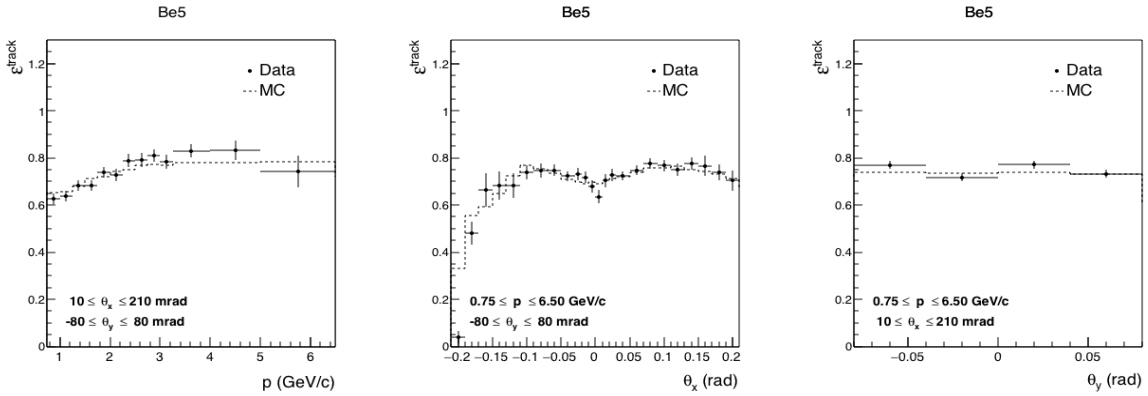

(a)

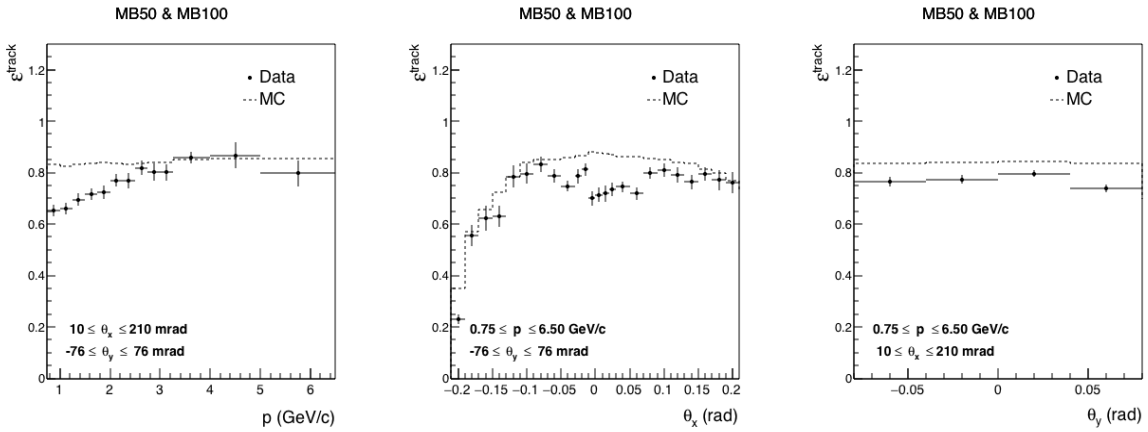

(b)

Figure 5.22: Total VERTEX4 track reconstruction efficiency from negative tracks as a function of p (left), θ_x (middle) and θ_y (right). The dark line represent the MC calculation compare to the dark dotted DATA calculation. Top row is representing the Be5 and the bottom row is from the combination of MB50 and MB100 measurements.

counts in the numerator of the fraction as:

$$\varepsilon^{TOF-match} = \frac{N[\exists p_2(\text{good}); \chi^2_{NDC1} \leq 20; (\text{NDC3} \vee \text{NDC4} \vee \text{NDC5}); \beta > 0]}{N[\exists p_2(\text{good}); \chi^2_{NDC1} \leq 20; (\text{NDC3} \vee \text{NDC4} \vee \text{NDC5})]}.$$

Here also the $\exists p_2(\text{good})$ assure that the control sample pass cuts $\chi^2_{v2} < 5$ and $r_{V2} < 200$ mm to select a good VERTEX2 sample.

In Fig. 5.24 and Fig. 5.25 show the TOFW-match efficiency as a function of p, θ_x and θ_y kinematic variables for positively and negatively charged tracks respectively. Consequently the total reconstruction efficiency measured with positively and negatively

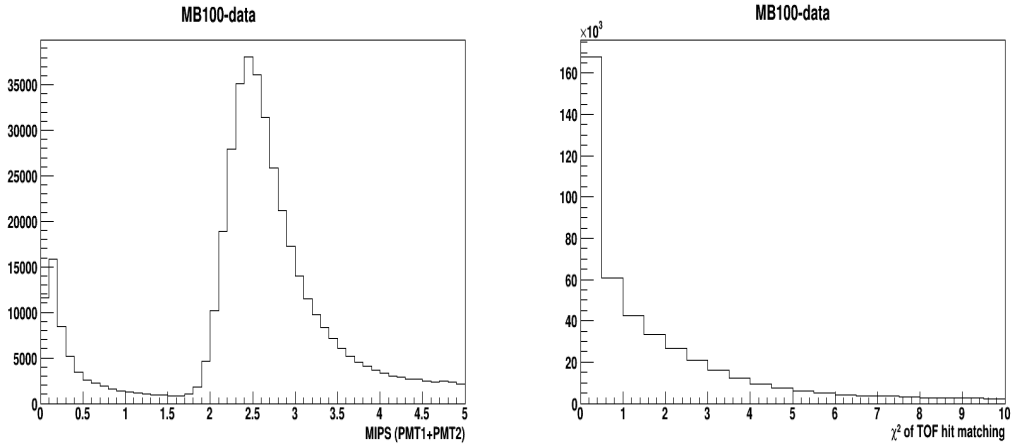

Figure 5.23: The TOFW hit measurements for MB100 target data. In the left panel, the reconstructed number of minimum ionizing particles, MIPS, distribution. Right distribution shows the match-χ^2 distribution of track position on TOFW hits.

charged tracks as shown in the projections along p, θ_x and θ_y variables in Fig. 5.26 and Fig. 5.27 are computed by combining the VERTEX4 track reconstruction efficiency with the TOF-match efficiency. The comparison of reconstruction efficiencies of data with MC in Fig. 5.26 and Fig. 5.27 shows the effect of the NDC1 chamber inefficiency of $p4$ type track reconstruction.

5.9 Momentum Migration Matrix

The reconstruction process can move a particle into a wrong momentum bin. To correct this momentum migration, a migration matrix is calculated. Elements of the momentum migration matrix are calculated by using Monte Carlo simulated events. The inverse correction matrix of momentum migration, $M^{-1}_{p.p'}$, is defined to unfold the true momentum, p, of a track from the reconstructed track momentum, p', as

$$N(p)_{true} = M^{-1}_{p.p'} \cdot N(p')_{observed}. \tag{5.15}$$

In this analysis we measure the momentum migration of p_4 to p_{truth} for short target Be5 and the long targets MB100, MB50 measurements. The diagonal matrix elements of each momentum range for all targets is shown in Fig. 5.28.

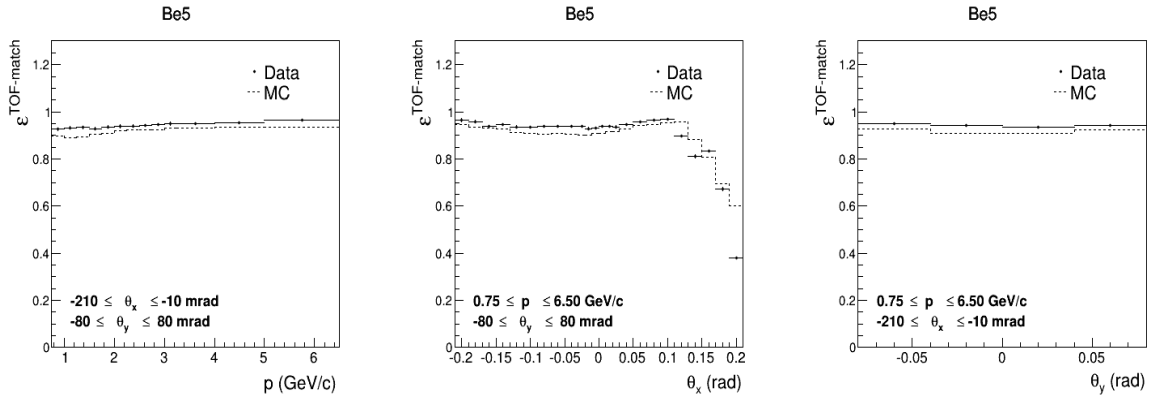

(a)

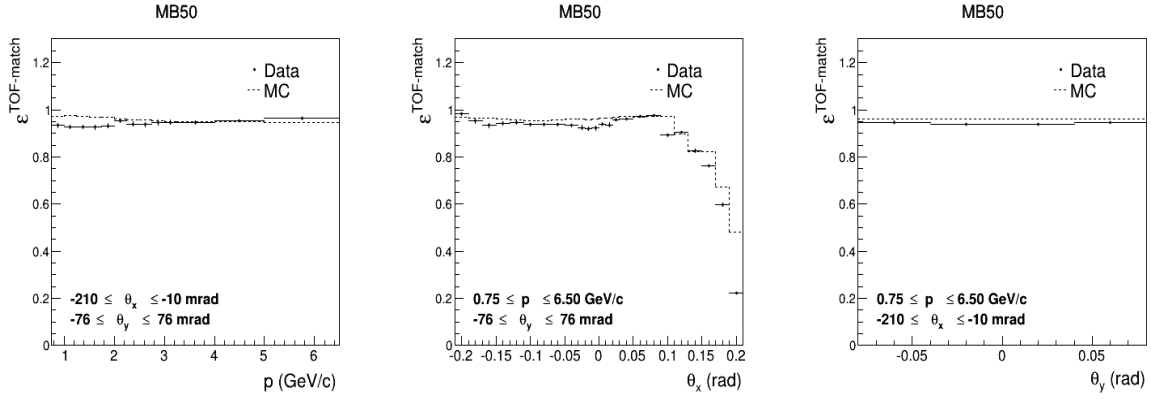

(b)

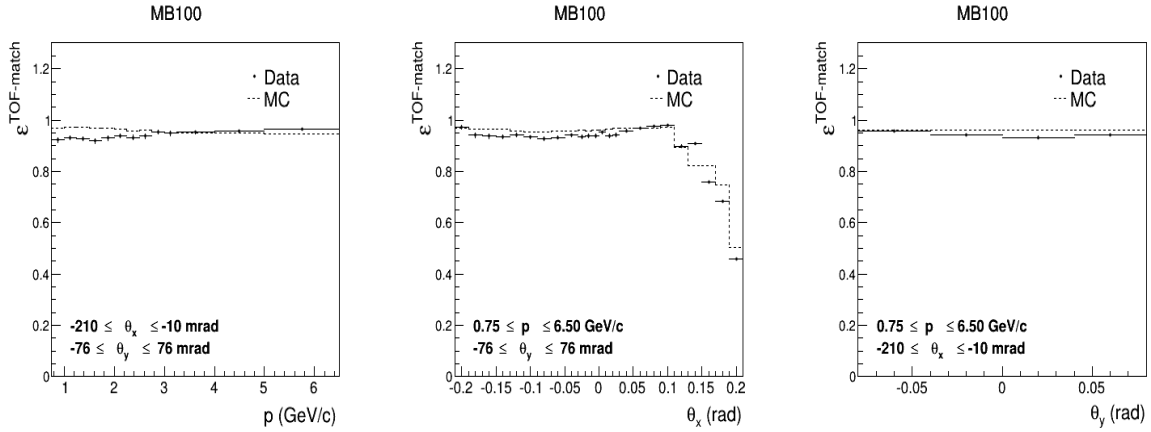

(c)

Figure 5.24: TOF-matching efficiency from positive tracks as a function of p (left), θ_x (middle) and θ_y (right). The dark line represent the MC estimation compare to the dark dotted DATA estimation. Top row is representing the Be5, the middle row is from MB50 and the bottom row is from MB100 measurements.

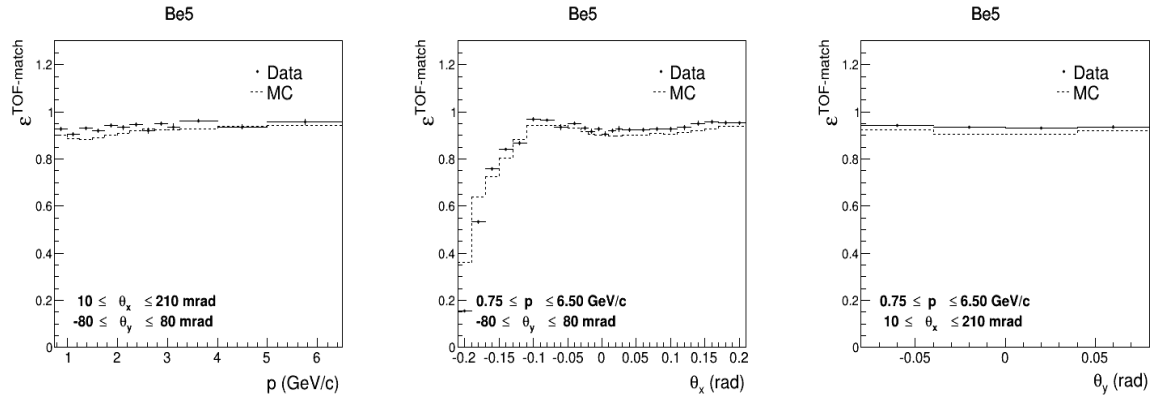

(a)

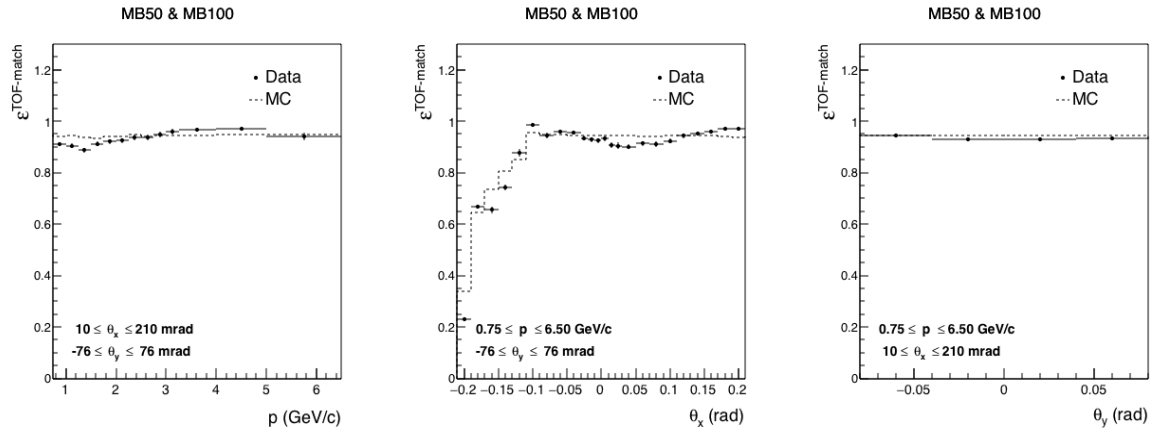

(b)

Figure 5.25: TOF-matching efficiency from negative tracks as a function of p (left), θ_x (middle) and θ_y (right). The dark line represent the MC estimation compare to the dark dotted DATA estimation. Top row is representing the Be5 and the bottom row is from the combination of MB50 and MB100 measurements.

The long target analysis for positive tracks is performed using MB100-8.9 GeV/c single proton Monte Carlo generated events. The negative track momentum migration is performed by using MB100-8.9 GeV/c single π^- MC generated events. The momentum migration matrix elements for MB50 target are measured by filtering the first half (-20.0-0 cm) of the MB100-8.9 GeV/c MC events to keep consistency with the target length of MB50 (20 cm) target.

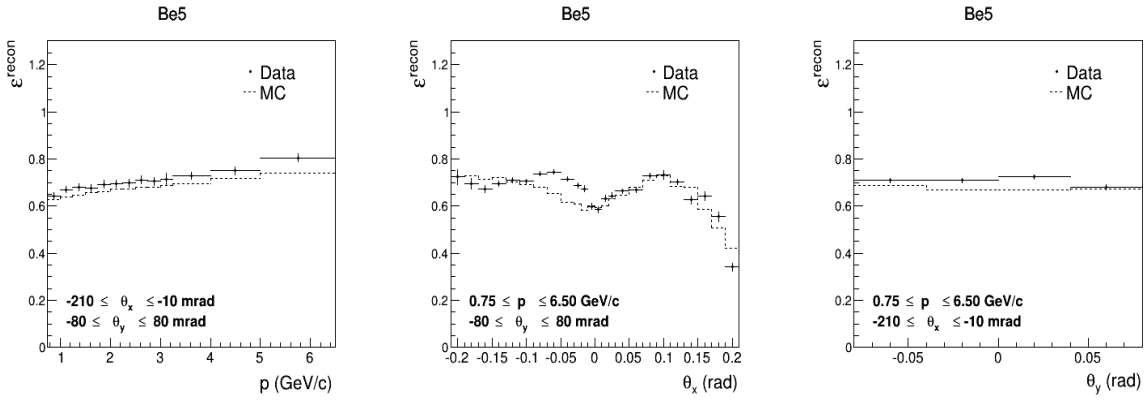

(a)

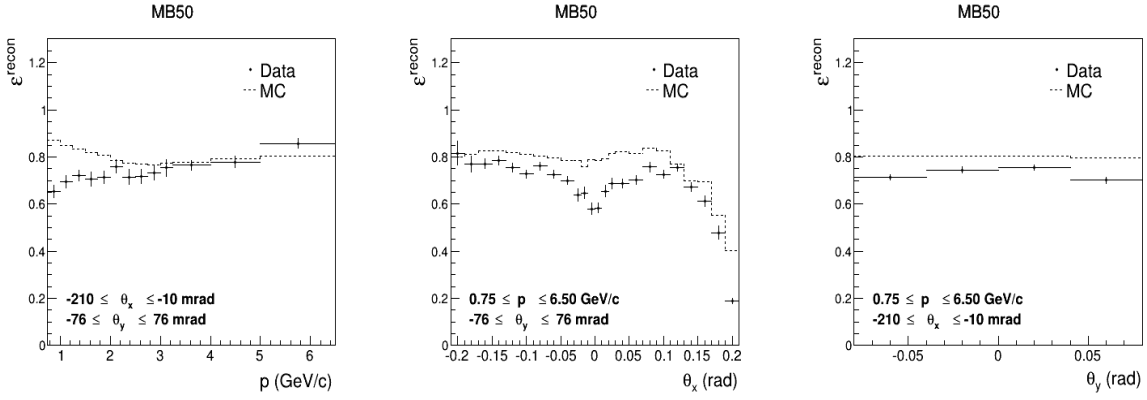

(b)

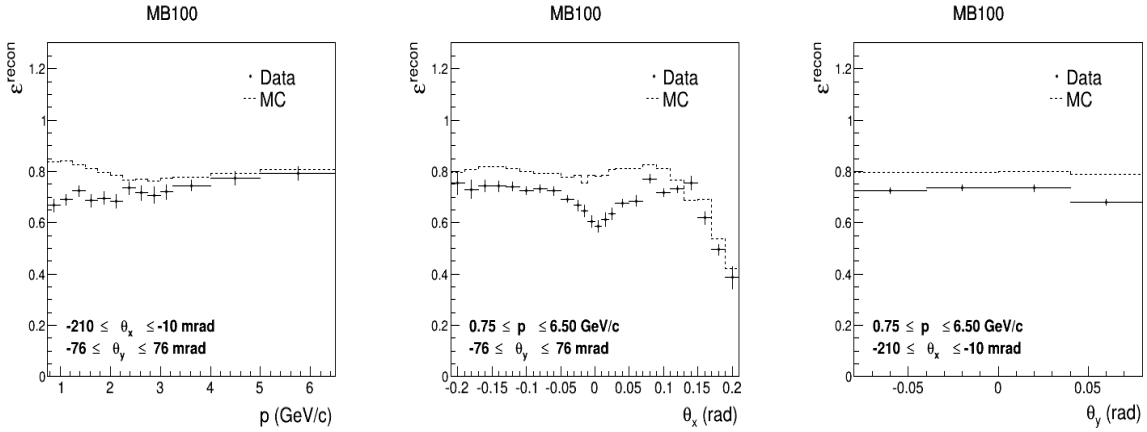

(c)

Figure 5.26: Total reconstruction efficiency by VERTEX4 as a function of p (left), θ_x (middle) and θ_y (right). The dark line represent the MC estimation compare to the dark dotted DATA estimation. Top row is representing the Be5, the middle row is from MB50 and the bottom row is from MB100 measurements.

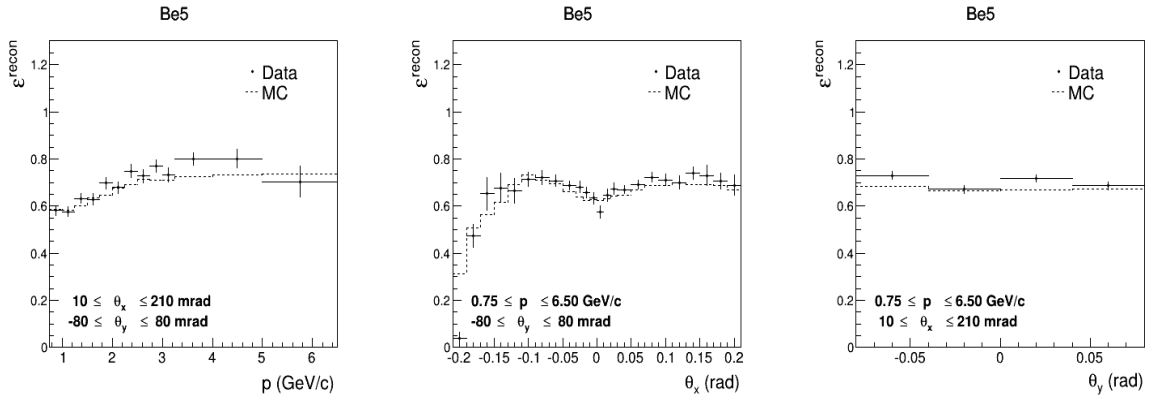

(a)

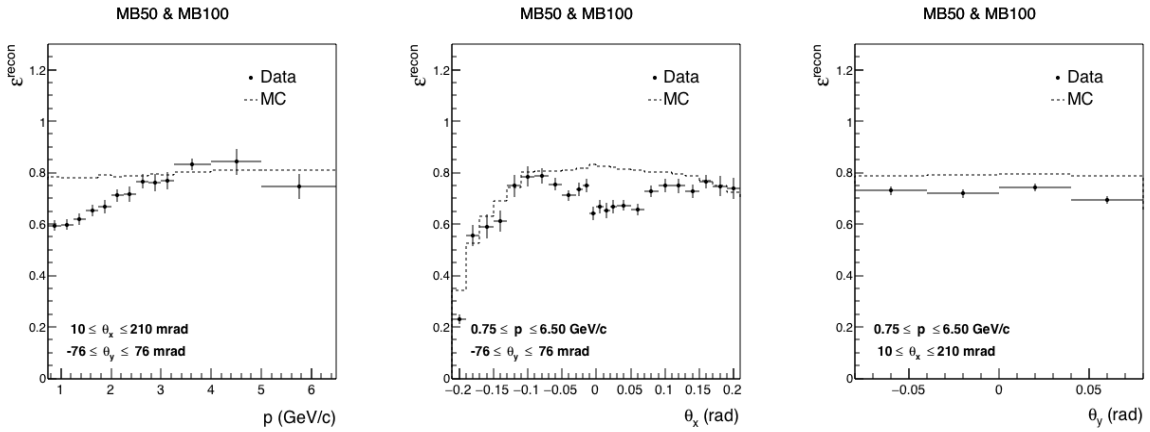

(b)

Figure 5.27: Total reconstruction efficiency by VERTEX4 from negative tracks as a function of p (left), θ_x (middle) and θ_y (right). The dark line represent the MC estimation compare to the dark dotted DATA estimation. Top row is representing the Be5 and the bottom row is from the combination of MB50 and MB100 measurements.

5.10 PID Efficiency and Migration Matrix

The reconstruction process can identify a pion as a proton and vice versa. The inefficiency of the particle ID algorithm is corrected by applying the PID migration matrix on the yield measurements. The particle ID migration matrix is

$$\begin{pmatrix} N^{\pi} \\ N^{\mathrm{p}} \end{pmatrix}_{obs} = \begin{pmatrix} M_{\pi\pi} & M_{\pi\mathrm{p}} \\ M_{\mathrm{p}\pi} & M_{\mathrm{pp}} \end{pmatrix} \cdot \begin{pmatrix} N^{\pi} \\ N^{\mathrm{p}} \end{pmatrix}_{true}$$

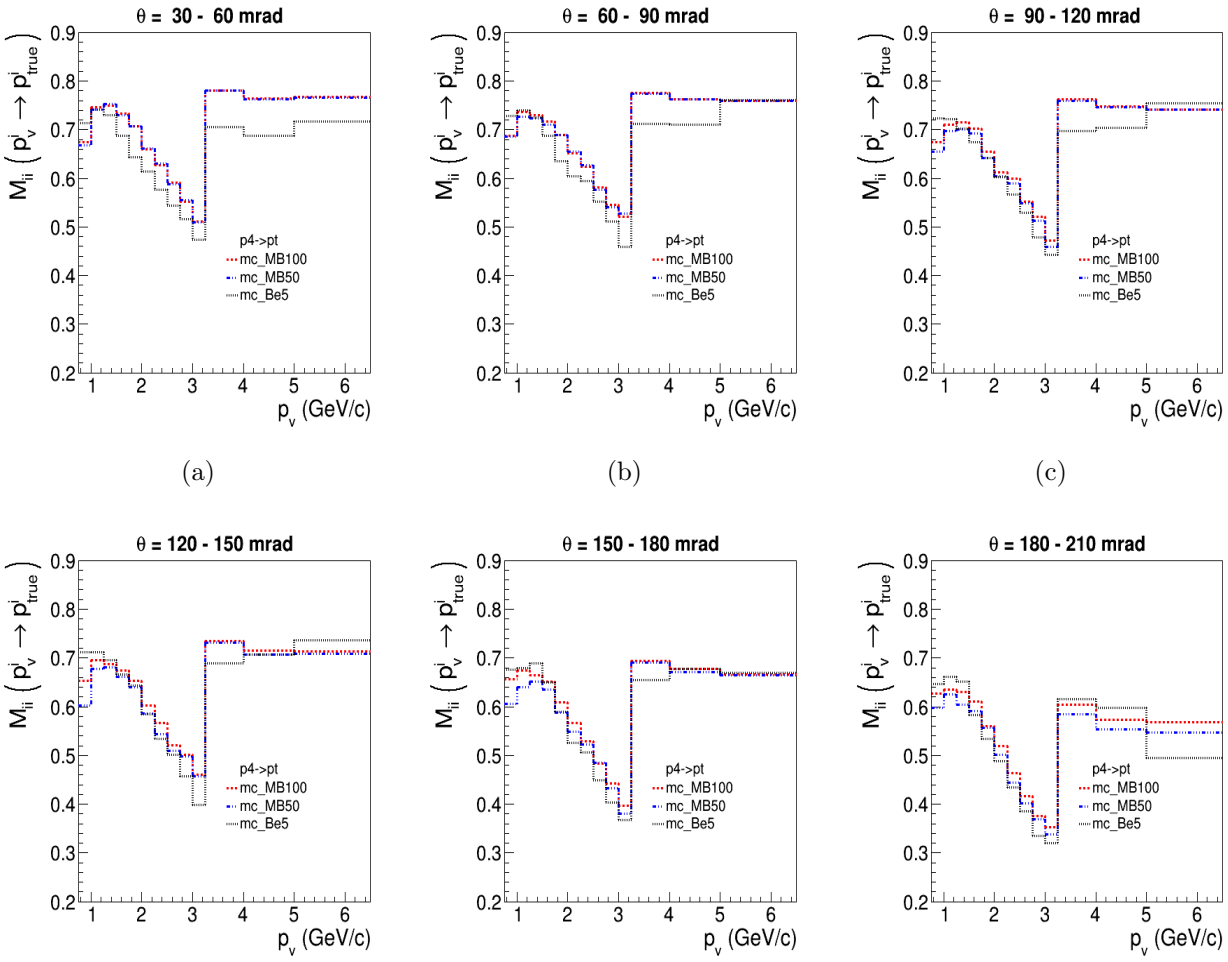

(a) (b) (c)

(d) (e) (f)

Figure 5.28: Diagonal elements of momentum migration matrix for angular bins from 30-210 mrad as a function of momentum. Black-dashed lines are representing for short target matrix elements. Red-dotted lines and blue dot-dasshed lines are representing for MB100 and MB50 respectively.

where the $M_{\pi\pi}$ and M_{pp} are the efficiencies of the identification of pions and protons respectively. The migration of pion to proton and proton to pions are representing by the elements of $M_{\pi\mathrm{p}}$ and $M_{\mathrm{p}\pi}$. To unfold the particle ID on observed measurements, the inverse of this migration matrix is applied on the yield measurements.

In the analytical calculation of matrix elements, the matrix elements of the particle ID migration matrix can be written as,

$$M_{\alpha,\alpha'} = \int_{P_\alpha > P_{cut}} d\beta dN_{phe} P(\beta|\alpha') \cdot P(N_{phe}|\alpha'), \tag{5.16}$$

where the terms $P(\beta|\alpha^{'})$ and $P(N_{phe}|\alpha')$ are the response probability density functions (PDFs) for α' type particle of the TOF wall and the Cherenkov counter respectively. A detailed analytical calculation of particle ID matrix elements is described in Ref. [71]. This references describe 4×4 covariance matrix from the elements $C_{i,j}$ for particle ID efficiency and migration matrix:

$$C_{i,j}^{k,l} = cov(M_{i,j}, M_{k,l}) = \frac{\partial M_{i,j}}{\partial \eta_m} \frac{\partial M_{k,l}}{\partial \eta_m} \cdot cov(\eta_m, \eta_m) \tag{5.17}$$

where the η_m has eight independent parameters: Cherenkov inefficiencies for pions and protons, mean β of pions and protons, standard deviation of β for pions and protons and the outlier rates for pion and protons. A detailed analytical calculation of the terms $\partial M_{i,j}/\partial \eta_m$ has been reported in the Ref. [71].

Since the particle type is independent from the target length, the migration matrix elements are estimated by using short target Monte Carlo generated events. This matrix elements are obtained by using p_4 type tracks. Fig. 5.29 shows the variation of the PID matrix elements as a function of momentum, p. Here the particle ID migration matrix elements of the processed events for incident beams with 1.0 cm and 0.4 cm beam radii are compared. The comparison study shows a negligible difference on matrix elements.

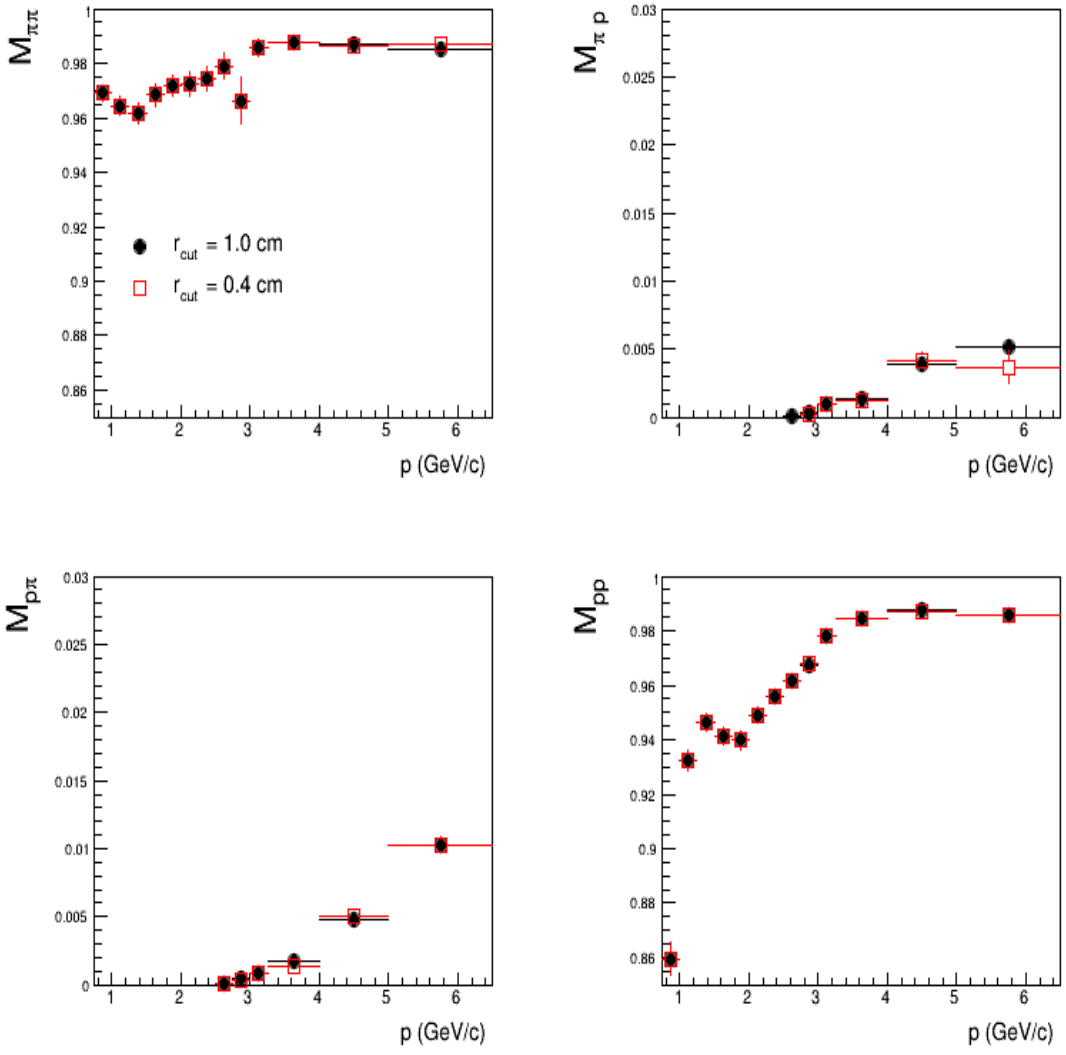

Figure 5.29: Particle ID matrix elements as a function of momentum, p, measured by short target MC generated events of p4 tracks. Here the black dotted distributions are representing the incident beam with 1.0 cm radius cut and the red-squared distributions are from the incident beam of 0.4 cm radius cut. The top-left distribution shows the pion identification efficiency, $M_{\pi\pi}$. The top-right distribution shows the migration of pion to proton, $M_{\pi \mathrm{p}}$. The bottom-left distribution shows the migration of proton to pion, $M_{\mathrm{p}\pi}$ and the bottom-right distribution shows the proton identification efficiency, M_{pp}.

5.11 Particle Absorption or Decay Correction

In the particle tracking process, some of the generated secondary particles from the p-Be interactions can be absorbed or decay before they reach the time of flight wall. The three dimensional absorption/decay correction term, $\eta_{\alpha}^{absorp}(p, \theta_x, \theta_y)$, is defined to take these missing tracks into account as a weight, $w_{abs} = [1 - \eta_{\alpha}^{absorp}(p, \theta_x, \theta_y)]^{-1}$. Using generated information from the Monte Carlo events we estimate the number of total missing particles that are created within the target geometry but do not pass through any back wall chamber. Since the absorption or the decay of the secondary particle through the detector volume does not depend on the target length or target type, the short target Monte Carlo generated events are used to perform the absorption correction for all targets. The result of the obtained absorption correction of pions and protons in the three variables space of (p, θ_x, θ_y) are shown in Fig. 5.30.

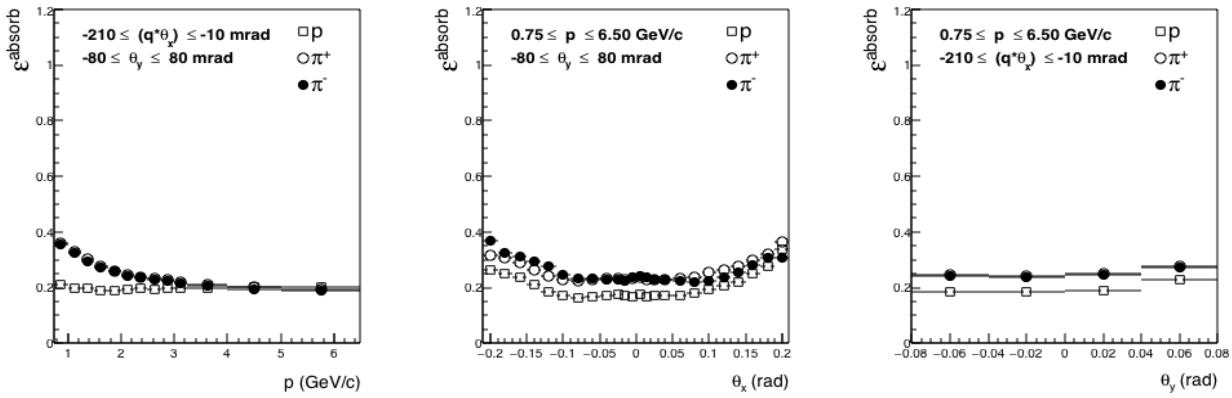

Figure 5.30: The absorption rates of π^+ (open-circles), π^- (solid-circles) and protons (open-square) distributions as a function of momentum (left), horizontal θ_x (middle) and vertical direction θ_y (right).

5.12 Tertiary Particle Production Correction

Any particle which is not created by primary proton-target nuclei interaction is defined as a tertiary particle. These background tertiary particles can be generated by re-interacting secondary particles with target nuclei or with material nuclei outside the

target. A tertiary track which is generated by a interaction of secondary pion with the material outside the target is removed from the data sample by this correction but the parent pion track is accounted for by the absorption correction. Pions which decay to muons are also removed by this correction. The other tertiary particle background is coming from the interaction of primary proton with the material nuclei outside the target. This background can subtract from the yield by using empty target data subtraction as describe in Section 5.3.

Three dimensional tertiary correction factor is calculated using truth information of tertiary tracks from the Monte Carlo simulated short beryllium target data. This is also applied as a weight, $w_{ter} = [1 - \eta_{\alpha}^{ter}(p', \theta'_x, \theta'_y)]$, for pion cross section analysis.

The tertiary correction for cross section measurements on short target is calculated by considering all above possibilities. Estimated rates of tertiary protons, pions and muons are compared in Fig. 5.31. This correction is applying to the secondary particle production cross section measurements of short Be5 target data.

The secondary particle interaction inside the target must be ignored for the yield measurements. Therefore the tertiary correction for these measurements is calculated by only taking account the tertiary particles generated outside the target volume. Since the rates of the tertiary particles generated outside the target is independent of the target length, the tertiary rates estimated from the short beryllium target MC are used to correct the pions and proton yield measurements in the long targets. The variation of the measured tertiary rates for yield measurements is showing in Fig. 5.32.

5.13 Electron Veto Correction

Electrons are removed from the sample by applying e-veto cut. This cut causes some loss of pions and protons below the pion Cherenkov threshold. The studies on electrons as described in [73] shows the ratio of electrons to pions below 3.0 GeV/c is low (see the left panel of Fig. 5.33). The right panel of Fig. 5.33 shows the efficiency of pions

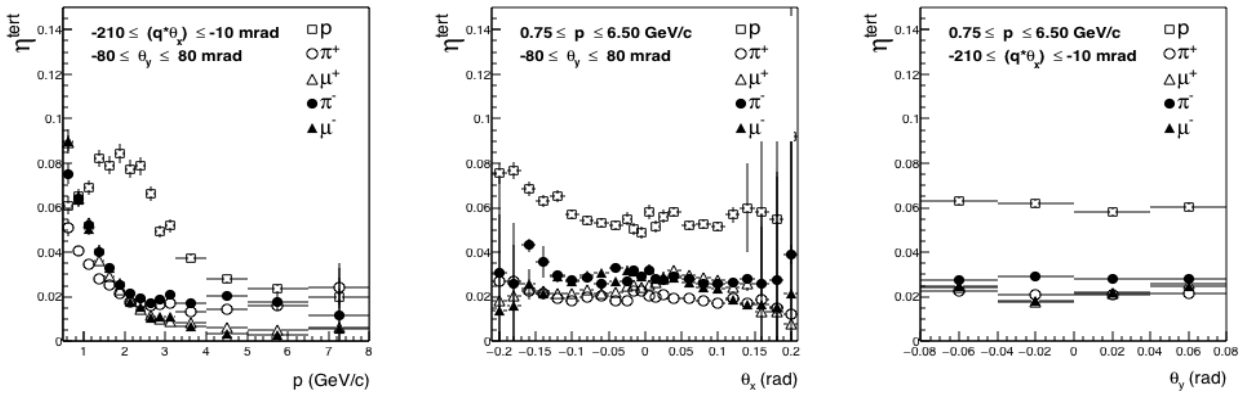

Figure 5.31: Tertiary particle rates to correct the secondary particle production cross section measurements on short beryllium target. Rates of proton, π^+, μ^+, π^- and μ^- as function of momentum (left), θ_x (middle) and θ_x (right) measured by Monte Carlo generated events of colliding 8.9 GeV/c proton beam with the short beryllium target. The parameters are selected to the analysis range of momentum: $0.75 < p < 8.0(GeV/c)$, the angular ranges of $-210 < \theta_x < -10(mrad)$ and $-80 < \theta_y < 80(mrad)$.

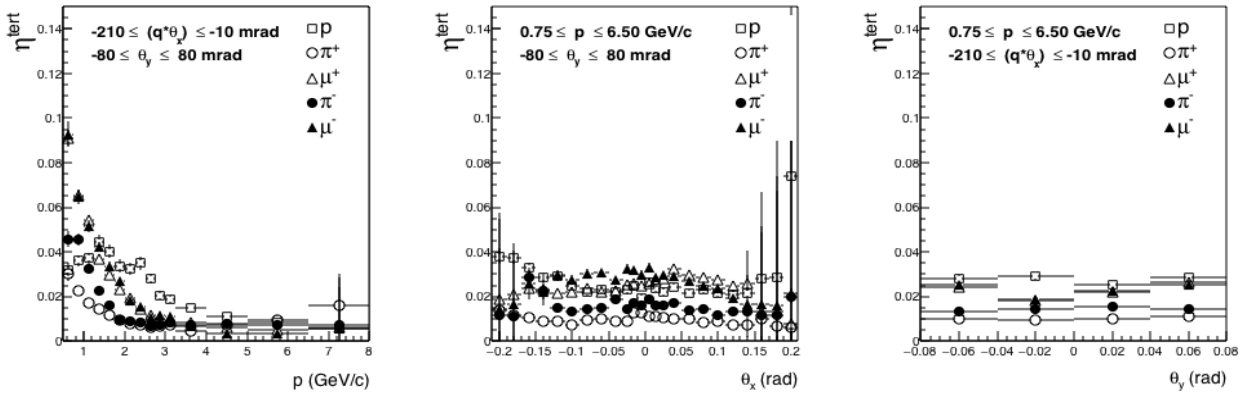

Figure 5.32: Tertiary particle rates to correct the secondary particle production yield measurements on all three targets. Rates of proton, π^+, μ^+, π^- and μ^- as function of momentum (left), θ_x (middle) and θ_x (right) measured by Monte Carlo generated events of colliding 8.9 GeV/c proton beam with the short beryllium target. The parameters are selected to the analysis range of momentum: $0.75 < p < 8.0(GeV/c)$, the angular ranges of $-210 < \theta_x < -10(mrad)$ and $-80 < \theta_y < 80(mrad)$.

(solid squares) and protons (open squares) which pass the electron veto cut.

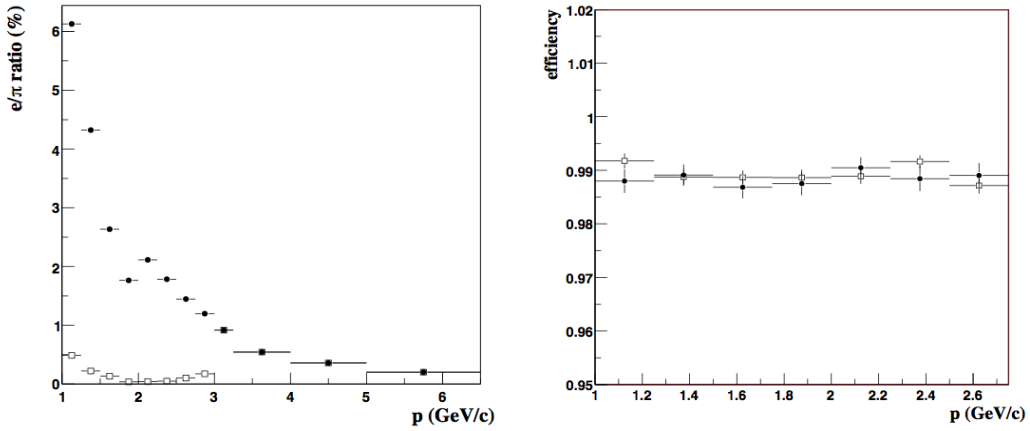

Figure 5.33: The correlation of electron veto cut from [73]. The ratio of pion to electron is shown in the left panel. Solid squares and open squares in the left panel describe the e/π ratio before and after applying $N_{phe} > 15$ cut respectively. The right panel shows the acceptance efficiency of the electron veto cut for pions (solid squares) and protons (open squares). This plot is taken from [73]

Chapter 6

Error Estimation

The estimation of the errors on each correction term is described in detail below.

First, the the central values of the double differential yield of secondary particle production, $d^2N^{\alpha}_{CV}/(dpd\Omega)$, is measured by applying the correction weights on raw events as described in the section 5. Next, a new set of correction values are prepared by selecting randomly fluctuated Gaussian values for given RMS on each correction term. This randomly selected sample of m^{th} correction term is applied to measure the double differential yield of secondary particle production again, $d^2N^{\alpha,m}/(dpd\Omega)$. In order to get an accurate estimation of uncertainty for each correction, this procedure is repeating for $\mathscr{N} \sim 100$ times.

After having all $\mathscr{N}$ number of double differential yield measurements for m^{th} correction source, the final elements of error matrix in (p, θ) parameter space is estimated by,

$$(\delta^{\alpha,m}_{i,j})^2 = \frac{1}{\mathscr{N}} \cdot \sum_{n=1}^{\mathscr{N}} \left[\frac{d^2N^{\alpha}_{CV}}{(dpd\Omega)} - \frac{d^2N^{\alpha,m}_{n}}{(dpd\Omega)} \right]_i \times \left[\frac{d^2N^{\alpha}_{CV}}{(dpd\Omega)} - \frac{d^2N^{\alpha,m}_{n}}{(dpd\Omega)} \right]_j , \tag{6.1}$$

where i and j representing given (p, θ) bins. This same error analysis criteria has been followed to estimate the errors on short target cross section measurements. The kinematical ranges in momentum and angle for presenting results are 0.75 GeV/c

$\leq p \leq 6.5$ GeV/c and 0.03 rad $\leq \theta \leq 0.21$ rad respectively. There are 13 momentum bins and 6 angular bins in the analysis. Therefore the full error matrix for production yield and cross section measurements has $(13 \times 6)^2 = 6084$ matrix elements.

6.1 The sources of errors

The error sources in the yield and the cross section measurements for all three targets are itemized as below.

i. **Target data (Statistical uncertainty)**

The matrix elements of the squared statistical error, $(\delta_{i,j}^{\alpha,stat})^2$, for the target data is estimated by taking the multiplication of the number of reconstructed tracks in a given (i^{th}, j^{th}) bins, $N_{i,j}$, with a required constant factor. This calculated factor converts the error into differential cross section or the differential yield. The statistical error matrix is a diagonal matrix because the statistical errors are not correlated.

ii. **Empty data (Statistical uncertainty)**

The matrix elements of the empty data statistical uncertainty are also similarly estimated as the target statistical uncertainty. Here we use 8.9 GeV/c momentum proton beam empty target data.

xiii. **Empty target subtraction uncertainty (Systematic uncertainty)**

According to the attenuation of the proton beam through the target, the fractions of empty target data subtraction used for MB100 and MB50 are 0.37, and 0.61 respectively as described in the Sec. 5.3. Therefore the fraction for the empty data subtraction systematic error is taken as 0.63 and 0.39 for MB100 and MB50 targets respectively. Since the 100% subtraction of empty target data on Be5 data analysis, the empty target subtraction uncertainty for Be5 is used as 5%.

iii. **Track reconstruction efficiency (Statistical uncertainty)**

The statistical uncertainty of the total track reconstruction efficiency is an error propagation of the uncertainties of chamber efficiencies, TOFW efficiency and

the VERTEX4 efficiency. The uncertainties of individual chamber efficiencies and TOFW efficiency are obtained as binomial errors. As described in the Sec. 5.8.2, the VERTEX4 efficiency is estimated by subtracting background effects on NDC1. Therefore the uncertainty of VERTEX4 efficiency is obtained by combining the $\sqrt{N_{bkg}}/N_{total}$ with the binomial error of VERTEX4 efficiency. Here the term N_{bkg} is the number of background events and N_{total} is the total number of events in the selected sample. The incident proton beam effects on NDC1 chamber depend on the target length and the target material type. Therefore we use three target data samples (Be5, MB50 and MB100) for their track reconstruction efficiency measurements.

iv. **Absorption correction (Systematic uncertainty)**

The simulated short target Monte Carlo data is used to compute the absorption correction for pions and protons. The systematic uncertainty of absorption correction for pions and protons is assumed to be 10% as described in the reference [59].

v. **Absorption correction (Statistical uncertainty)**

Since the absorption correction is independent from the target material type or the incident beam momentum, the absorption correction is calculated by combining Monte Carlo samples which were generated for different target materials. Hence the statistical uncertainty has been decreased by increasing the data sample size.

vi. **Tertiary particle correction (Systematic uncertainty)**

The tertiary particle subtraction corrections for production cross section and production yield measurements are correlated with the target material density, nuclear structure and also with the incident beam momentum. Therefore this correction is calculated by using short beryllium target Monte Carlo simulated data. A similar analysis as described in the [59] has been carried out to calculate the systematic uncertainty of tertiary particle subtraction correction. The systematic uncertainty of tertiary particle correction is assumed to be 50% for

production yield analysis.

vii. **Tertiary particle correction (Statistical uncertainty)**

As described in [vi], the tertiary particle rate calculation is performed by short beryllium target simulated Monte Carlo sample. Therefore the statistical uncertainty depends on the size of the MC generated p-Be event sample.

viii. **Momentum scale (Systematic uncertainty)**

The momentum calibration has been studied by using empty target data sets of momentum range 1.5-15.0 GeV/c for zero angle and also using elastic scattering events for non-zero angles as described in [59] and [73]. Momentum resolution $\sigma(p)/p$ has been compared with the Monte Carlo measurements. These studies imply 2% uncertainty on momentum reconstruction. Therefore the momentum scale systematic uncertainty is calculated by scaling the momentum of each track randomly from a Gaussian function with width 0.02 and mean 1.0 in the cross section (and yield) measurements.

ix. **Momentum migration (Systematic uncertainty)**

The systematic uncertainty of the migration is defined by the migration of the true momentum value in to a different momentum value due to the reconstruction algorithm and the particle detector resolutions. The migration systematic uncertainty on cross section (and yield) measurements is calculated by generating a migration matrix for a hadronic interaction model as described in the [59].

x. **Momentum migration (Statistical uncertainty)**

The statistical uncertainty of momentum migration is estimated by generating fluctuated migration matrix elements in a binomial distribution before the normalization. The cross sections (and yields) are measured for 100 random variations.

xi. **Electron veto (Statistical uncertainty)**

The cross section and the yield measurements are estimated by using a randomly selected (according to a Gaussian distribution) electron veto correction within

their statistical errors. This procedure has been repeated for 100 number of random variations to estimate the statistical uncertainty.

xii. **Particle ID (Systematic uncertainty)**

The cross section and the yield measurements are estimated by using the fluctuated particle ID migration matrix due to a multivariate normal distribution of the 16-element covariance matrix generated in the particle identification algorithm as described in Sec. 5.10. This analysis is repeated for 100 number of variations to estimate the particle ID systematic uncertainty.

xiv. **Overall normalization (Systematic uncertainty)**

The incoming beam protons selection cuts makes an accurate beam selection with the 1% uncertainty for the overall normalization of the cross section measurements and the yield measurements. In addition to that, another 1% of normalization systematic uncertainty comes from the reconstruction efficiency and particle identification efficiency measurements as described in the Ref. [59]. Therefore the overall normalization systematic uncertainty for measurements is estimated as 2%.

6.2 Fractional error

The quantitative terms of averaged fractional error on double differential yield or cross section measurements δ_{diff},

$$\delta_{diff} = \frac{1}{N_{bins}} \sum_{i=1}^{N_{bins}} \frac{\delta_{ii}}{[d^2\sigma^{\alpha}_{CV}/(dpd\Omega)]_i}, \text{ and} \tag{6.2}$$

the total integrated fractional error, δ_{int},

$$\delta_{int} = \frac{\sqrt{\sum_{i,j}(dp.d\Omega)_i \delta^2_{ij}.(dp.d\Omega)_j}}{\sum_i (d^2\sigma^{\alpha}_{CV})_i}. \tag{6.3}$$

are defined to present a general interpretation about the estimated uncertainties of each error source. In the Eq. 6.2 the terms of i represent the given (p, θ) bin and the N_{bins} is the number of (p, θ) bins in the matrix. The term δ_{ii} is the covariance matrix diagonal elements of given i^{th} bin in the parameter space. In the Eq. 6.3 the terms of δ_{ij} is the covariance error matrix elements of given i^{th} and j^{th} bins in the parameter space. The term $(d^2\sigma^{\alpha}_{CV})_i$ is the product of the phase space factor $(dp.d\Omega)_i$ with the CV of the double differential cross section in i^{th} bin.

The Table 6.1 shows a summary of each error source evaluated for double differential production cross section measurements on short Be5 target. The Table 6.2 and Table 6.3 show the summary of the estimated uncertainties for each error category from π^+ and π^- production yield analysis on all three targets respectively.

Particle type	π^+		π^-		p	
momentum range (GeV/c)	$0.75 - 6.5$		$0.75 - 6.5$		$0.75 - 8.0$	
angular range (rad)	$0.03 - 0.210$		$0.03 - 0.210$		$0.03 - 0.210$	
Error Category	$\delta^{\pi^+}_{diff}(\%)$	$\delta^{\pi^+}_{int}(\%)$	$\delta^{\pi^-}_{diff}(\%)$	$\delta^{\pi^-}_{int}(\%)$	$\delta^{p}_{diff}(\%)$	$\delta^{p}_{int}(\%)$
Statistical Errors :						
1. Target statistics	5.0	0.6	8.0	0.9	5.1	0.4
2. Empty target statistics	4.5	0.6	6.4	0.8	5.2	0.4
Sub-total	**6.7**	**0.8**	**10.2**	**1.2**	**7.3**	**0.6**
Track yield corrections:						
3. Empty target subtraction	1.0	0.1	0.8	0.1	1.0	0.2
4. Reconstruction efficiency	3.4	0.8	6.9	1.5	3.6	0.5
5. Pion, proton absorption (syst)	3.8	4.3	3.5	4.4	2.7	2.5
6. Pion, proton absorption (stat)	0.4	0.1	0.4	0.1	0.4	< 0.1
7. Tertiary subtraction (syst)	2.7	3.2	3.0	4.1	3.5	2.2
8. Tertiary subtraction (stat)	0.3	0.1	0.4	0.1	0.6	< 0.1
Sub-total	**5.9**	**5.4**	**8.4**	**6.2**	**5.8**	**3.4**
Momentum reconstruction:						
9. Momentum scale	3.9	0.1	6.3	0.3	3.9	1.5
10. Momentum resolution (syst)	2.6	0.3	3.5	0.2	2.8	0.4
11. Momentum resolution (stat)	1.5	< 0.1	2.5	0.2	1.5	< 0.1
Sub-total	**4.9**	**0.3**	**7.6**	**0.4**	**5.0**	**1.6**
Particle Identification:						
12. Electron veto	0.1	< 0.1	0.1	< 0.1	0.1	< 0.1
13. Pion, proton ID correction	0.4	0.4	0.4	0.4	0.3	0.1
Sub-total	**0.4**	**0.4**	**0.4**	**0.4**	**0.3**	**0.1**
Overall normalization:	**2.0**	**2.0**	**2.0**	**2.0**	**2.0**	**2.0**
Total	**10.4**	**5.8**	**15.4**	**6.6**	**10.8**	**4.3**

Table 6.1: A summery of the estimated uncertainties in each error source for $\pi^{\pm}$ and proton production cross sections , $d^2\sigma/(dpd\Omega)$, of proton (8.9 GeV/c) + Be5 target interaction.

Particle type	π^+		π^+		π^+	
Target type	Be5		MB50		MB100	
momentum range (GeV/c)	$0.75 - 6.5$		$0.75 - 6.5$		$0.75 - 6.5$	
angular range (rad)	$0.03 - 0.210$		$0.03 - 0.210$		$0.03 - 0.210$	
Error Category	$\delta^{\pi^+}_{diff}(\%)$	$\delta^{\pi^+}_{int}(\%)$	$\delta^{\pi^+}_{diff}(\%)$	$\delta^{\pi^+}_{int}(\%)$	$\delta^{\pi^+}_{diff}(\%)$	$\delta^{\pi^+}_{int}(\%)$
Statistical Errors :						
1. Target statistics	5.0	0.6	7.9	0.9	7.2	0.8
2. Empty target statistics	4.6	0.6	0.9	0.1	0.3	< 0.1
Sub-total	**6.8**	**0.8**	**8.0**	**0.9**	**7.2**	**0.8**
Track yield corrections:						
3. Empty target subtraction	1.0	0.1	0.8	0.1	0.5	< 0.1
4. Reconstruction efficiency	3.4	0.8	5.4	1.3	4.8	1.2
5. Pion absorption (syst)	3.5	4.1	3.4	3.9	3.7	4.3
6. Pion absorption (stat)	0.4	< 0.1	0.4	< 0.1	0.4	< 0.1
7. Tertiary subtraction (syst)	1.8	2.2	1.7	2.3	1.9	2.5
8. Tertiary subtraction (stat)	0.2	< 0.1	0.3	< 0.1	0.3	< 0.1
Sub-total	**5.3**	**4.7**	**6.7**	**4.7**	**6.4**	**5.1**
Momentum reconstruction:						
9. Momentum scale	3.8	0.1	4.4	0.2	3.9	0.1
10. Momentum resolution (syst)	2.6	0.3	4.0	0.5	3.0	0.7
11. Momentum resolution (stat)	1.5	< 0.1	1.4	0.1	1.0	< 0.1
Sub-total	**4.8**	**0.3**	**6.1**	**0.5**	**5.0**	**0.7**
Particle Identification:						
12. Electron veto	0.1	< 0.1	0.1	< 0.1	0.1	< 0.1
13. Pion, proton ID correction	0.3	0.3	0.5	0.3	0.5	0.3
Sub-total	**0.3**	**0.3**	**0.5**	**0.3**	**0.5**	**0.3**
Overall normalization:	**2.0**	**2.0**	**2.0**	**2.0**	**2.0**	**2.0**
Total	**10.1**	**5.18**	**12.3**	**5.2**	**11.0**	**5.6**

Table 6.2: A summery of the estimated uncertainties in each error source for π^+ production yield, $d^2N/(dpd\Omega)$, of proton (8.9 GeV/c) interactions with Be5, MB50 and MB100 targets.

Particle type	π^-		π^-		π^-	
Target type	Be5		MB50		MB100	
momentum range (GeV/c)	$0.75 - 6.5$		$0.75 - 6.5$		$0.75 - 6.5$	
angular range (rad)	$0.03 - 0.210$		$0.03 - 0.210$		$0.03 - 0.210$	
Error Category	$\delta^{\pi^-}_{diff}(\%)$	$\delta^{\pi^-}_{int}(\%)$	$\delta^{\pi^-}_{diff}(\%)$	$\delta^{\pi^-}_{int}(\%)$	$\delta^{\pi^-}_{diff}(\%)$	$\delta^{\pi^-}_{int}(\%)$
Statistical Errors :						
1. Target statistics	8.0	0.9	11.3	1.2	10.5	1.2
2. Empty target statistics	6.4	0.8	0.8	0.1	0.3	< 0.1
Sub-total	**10.2**	**1.2**	**11.3**	**1.2**	**10.5**	**1.2**
Track yield corrections:						
3. Empty target subtraction	0.8	0.1	0.9	0.2	0.4	<0.1
4. Reconstruction efficiency	7.0	1.6	6.2	1.4	6.5	1.7
5. Pion absorption (syst)	3.3	4.1	3.4	4.4	3.8	4.8
6. Pion absorption (stat)	0.4	0.1	0.4	0.1	0.4	0.1
7. Tertiary subtraction (syst)	2.4	3.5	2.8	4.0	2.7	3.8
8. Tertiary subtraction (stat)	0.3	0.1	0.4	0.1	0.3	0.1
Sub-total	**8.2**	**5.6**	**7.7**	**6.1**	**8.0**	**6.4**
Momentum reconstruction:						
9. Momentum scale	5.4	0.2	6.3	0.4	5.7	0.2
10. Momentum resolution (syst)	3.5	0.2	8.5	0.3	11.1	0.3
11. Momentum resolution (stat)	2.5	0.2	2.0	0.2	1.6	0.1
Sub-total	**6.9**	**0.3**	**10.8**	**0.5**	**12.6**	**0.4**
Particle Identification:						
12. Electron veto	0.1	<0.1	0.1	<0.1	0.1	<0.1
13. Pion, proton ID correction	0.4	0.4	0.4	0.4	0.4	0.4
Sub-total	**0.4**	**0.4**	**0.4**	**0.4**	**0.4**	**0.4**
Overall normalization:	**2.0**	**2.0**	**2.0**	**2.0**	**2.0**	**2.0**
Total	**14.9**	**6.1**	**17.5**	**6.6**	**18.4**	**6.8**

Table 6.3: A summery of the estimated uncertainties in each error source for π^- production yield, $d^2N/(dpd\Omega)$, of proton (8.9 GeV/c) interactions with Be5, MB50 and MB100 targets.

Part III

Results

Chapter 7

Pion production results

The production cross section results and the production yield results measured on Be5, MB50 and MB100 targets as described in the above sections are presented in this section.

7.1 Production cross section results

Figures 7.1 and 7.2 compares the measured double differential π^+ and π^- production cross sections respectively from Be5 short target using the VETTEX4 type reconstructed tracks with that of measured by VERTEX2 type reconstructed tracks in the analysis of [59]. As can be seen there, the two algorithms agree with each other. Furthermore the $\pi^{\pm}$ cross sections are compared with the cross sections predicted by the simulation of the MiniBooNE beamline Monte Carlo (blue-trangular points). The Sanford-Wang, SW, parameters measured by VERTEX2 analysis of short Be5 target [59] are used for the beamline MC event simulator. The dashed green cross section (in Fig. 7.1 and Fig. 7.2) obtained from the SW model are compared with the cross section measured by data and the MC. The MC prediction is consistence with the Sanford-Wang calculation predicted curves but falls below the measured cross section for most angular bins. Figure 7.3 show the production cross section measurements of protons for short Be5 target. Here we compare the yield measurements from VERTEX4

type tracks with the measurements from VERTEX2 type reconstructed tracks. The measured production cross sections of pions and protons with their estimated errors are presented in the Table A.1.

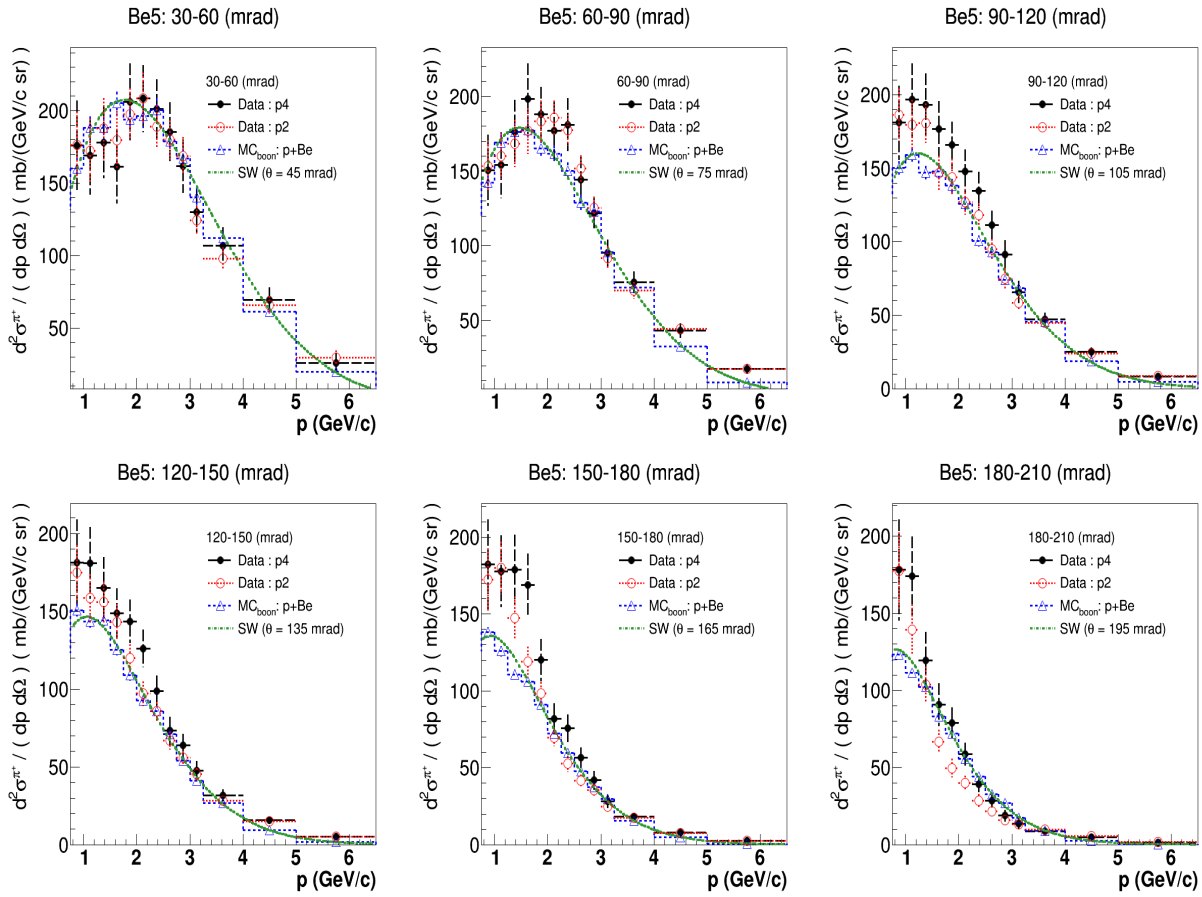

Figure 7.1: π^+ production cross section, $d^2\sigma/(dpd\Omega)$, as a function of momentum p for Be5 data. The measured pion production cross sections from VERTEX4 (black-dotted) type tracks compared with the MiniBooNE MC predicted cross section (blue-triangular shaped) and the measured cross section from VERTEX2 type tracks (red-squared). Here the green-dashed curve shows the SW predicted cross section.

7.2 Production yield results

The double differential pion ($\pi^{\pm}$) production yields for three beryllium targets are presented in Figs. 7.4 - 7.9 and Tables B.1 and C.1. In these figures show the $\pi^{\pm}$ differential yields are compared with the MiniBooNE beamline MC predicted $\pi^{\pm}$ differential yields. Since the re-interactions of secondaries are not taking place within

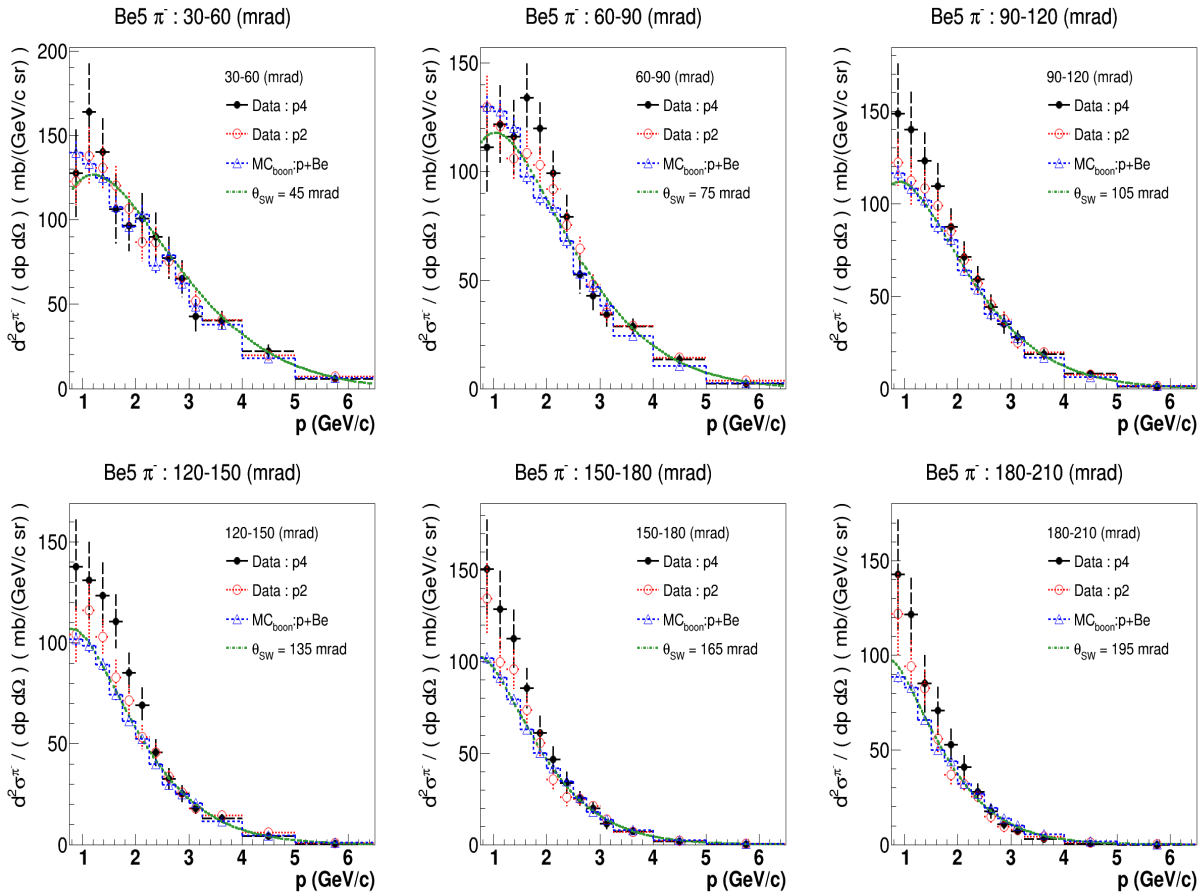

Figure 7.2: π^- production cross section, $d^2\sigma/(dpd\Omega)$, as a function of momentum p for Be5 data. The measured pion production cross sections from VERTEX4 (black-dotted) type tracks compared with the MiniBooNE MC predicted cross section (blue-triangular shaped) and the measured cross section from VERTEX2 type tracks (red-squared). Here the green-dashed curve shows the SW predicted cross section.

the volume of 2 cm short target, the MC generated pion production from the p+Be primary interactions (p+Be) has a small difference with that from the out coming pion production of the target (final state). This re-interaction of the secondaries in the target volume is visible in the small angles comparing the primary (p+Be) and the out coming (final state) productions from the MC generated 20 cm and 40 cm targets. That implies the simulation has been taken care of this model dependent tertiary particle productions.

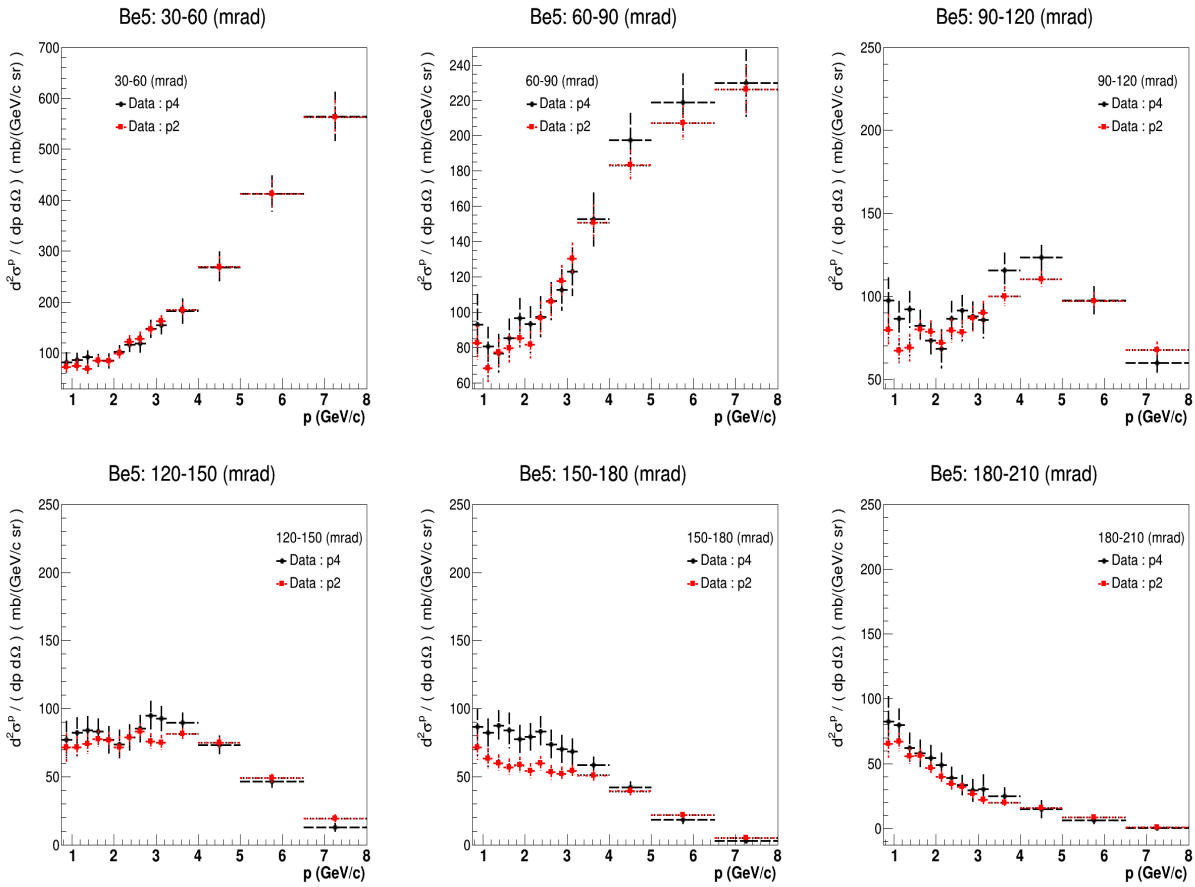

Figure 7.3: The comparison of proton production cross sections, $d^2\sigma/(dpd\Omega)$, measured from VERTEX2 (red-squared) and VERTEX4 (black-dotted) type tracks.

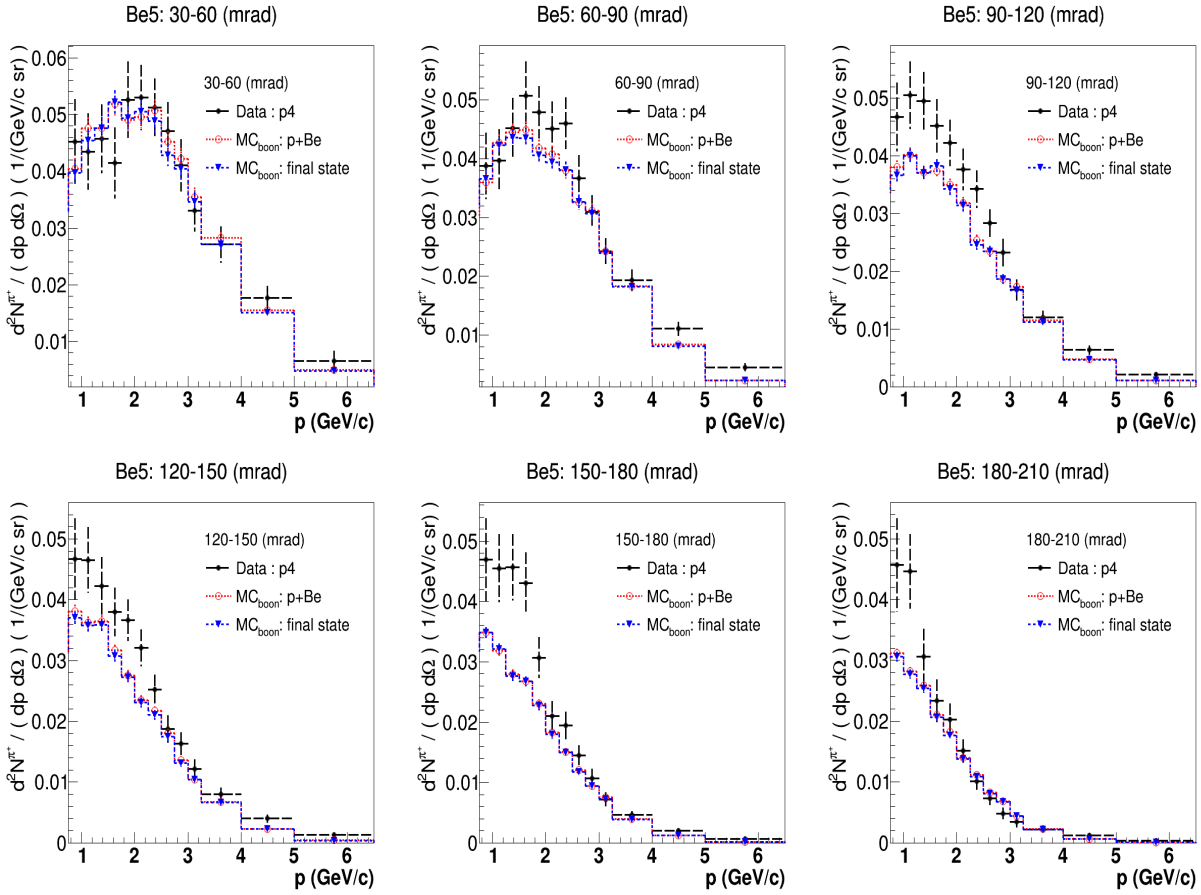

Figure 7.4: π^+ production yield , $d^2N/(dpd\Omega)$, as a function of momentum p for Be5 is compared with the MiniBooNE MC predicted π^+ yield for 2.0 cm target. Here the red upward triangular distribution is the output from the primary p+Be interaction and the blue downward triangular distribution is the final out coming particles from the target.

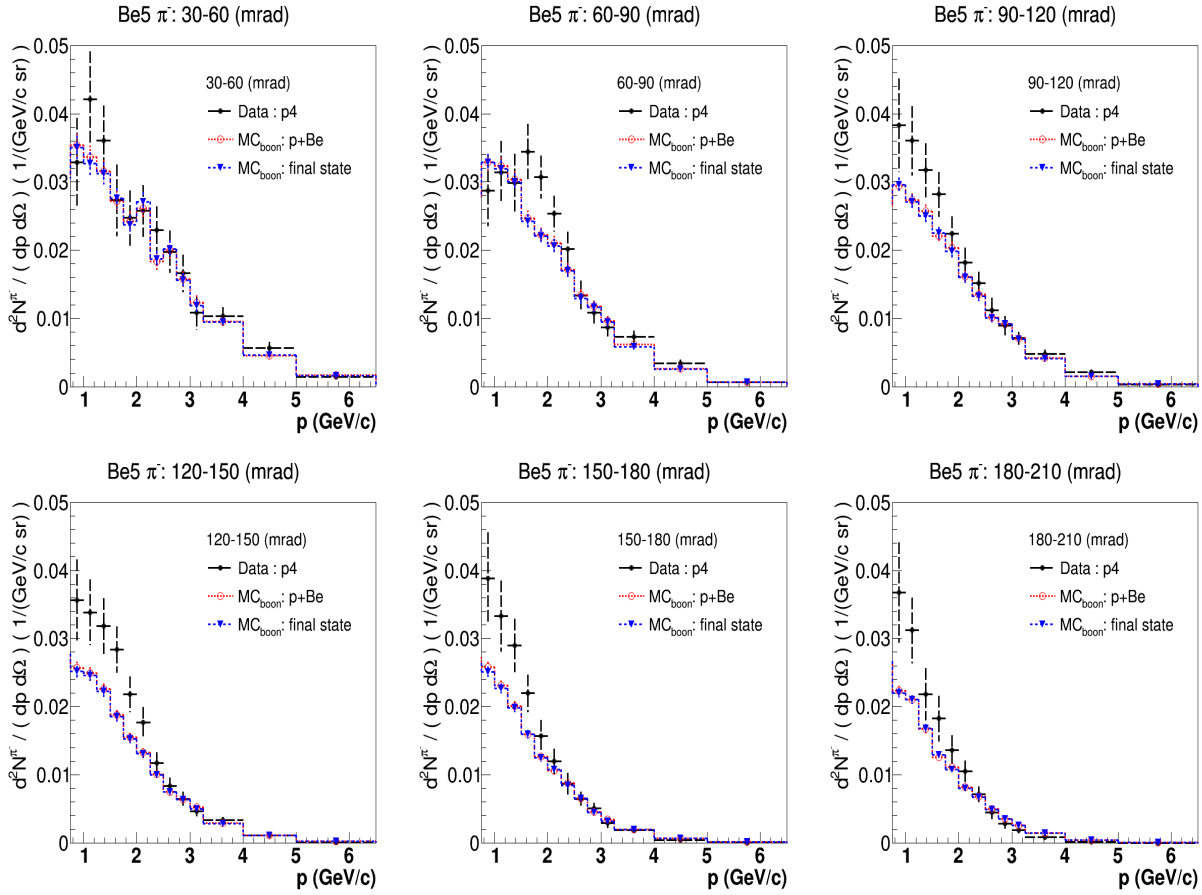

Figure 7.5: π^- production yield , $d^2N/(dpd\Omega)$, as a function of momentum p for Be5 is compared with the MiniBooNE MC predicted π^- yield for 2.0 cm target. Here the red upward triangular distribution is the output from the primary p+Be interaction and the blue downward triangular distribution is the final out coming particles from the target.

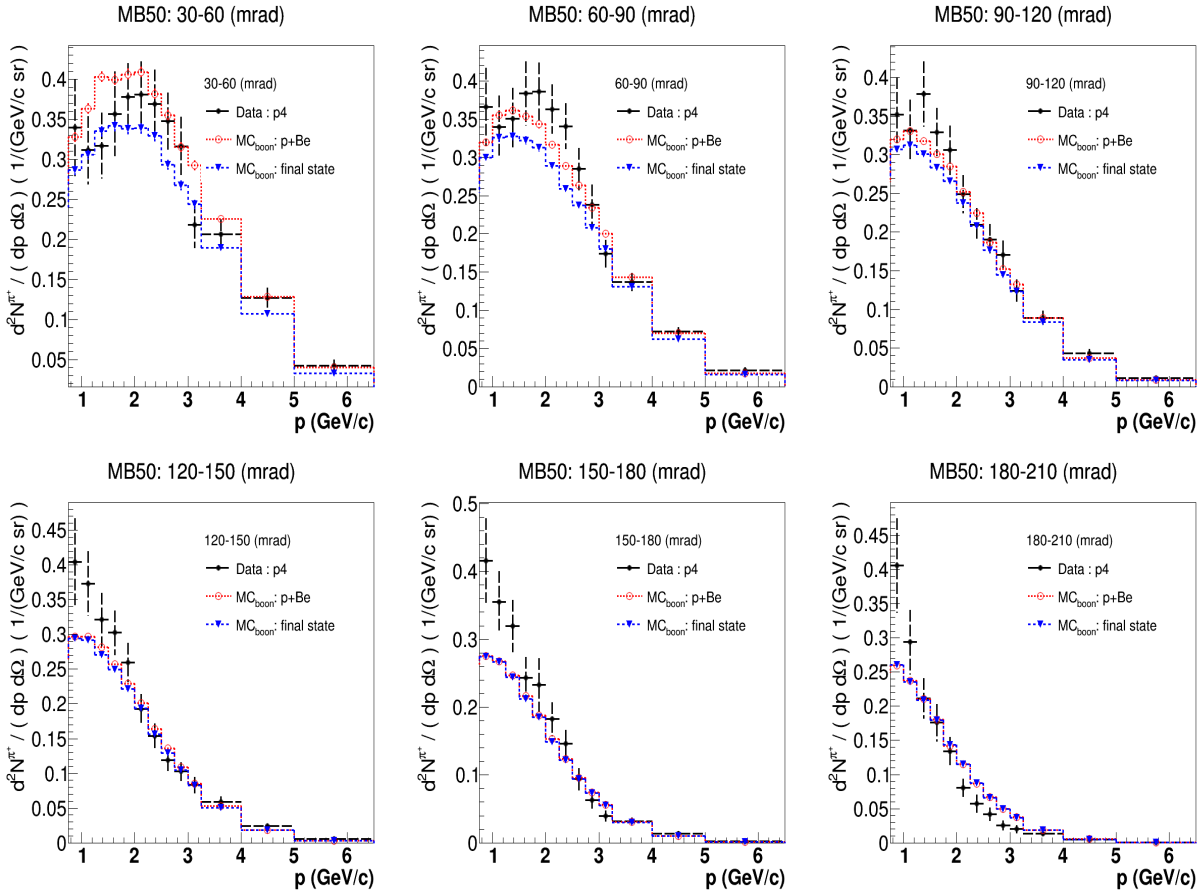

Figure 7.6: π^+ production yield , $d^2N/(dpd\Omega)$, as a function of momentum p for MB50 data is compared with the MiniBooNE MC predicted yield for 20.0 cm target. Here the red upward triangular distribution is the output from the primary p+Be interaction and the blue downward triangular distribution is the final out coming particles from the target.

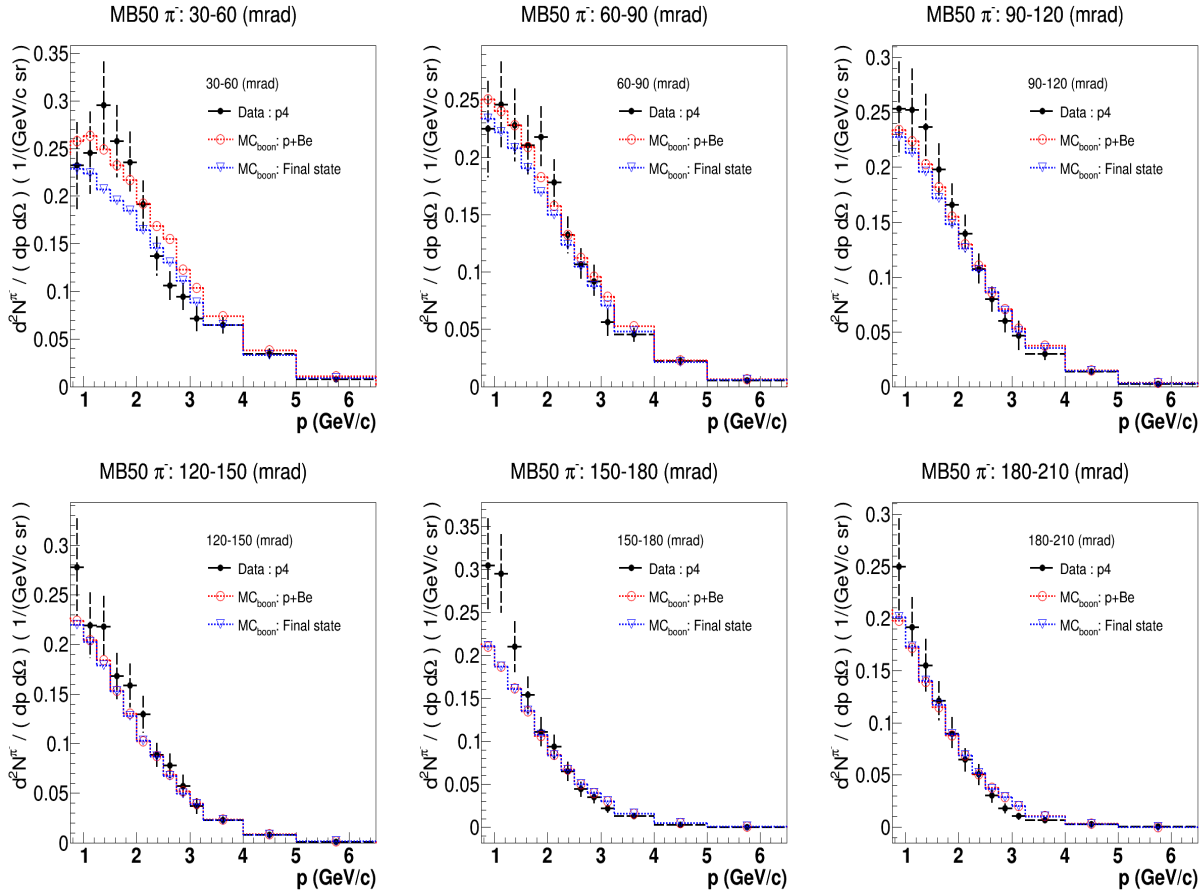

Figure 7.7: π^- production yield , $d^2N/(dpd\Omega)$, as a function of momentum p for MB50 data is compared with the MiniBooNE MC predicted yield for 20.0 cm target. Here the red upward triangular distribution is the output from the primary p+Be interaction and the blue downward triangular distribution is the final out coming particles from the target.

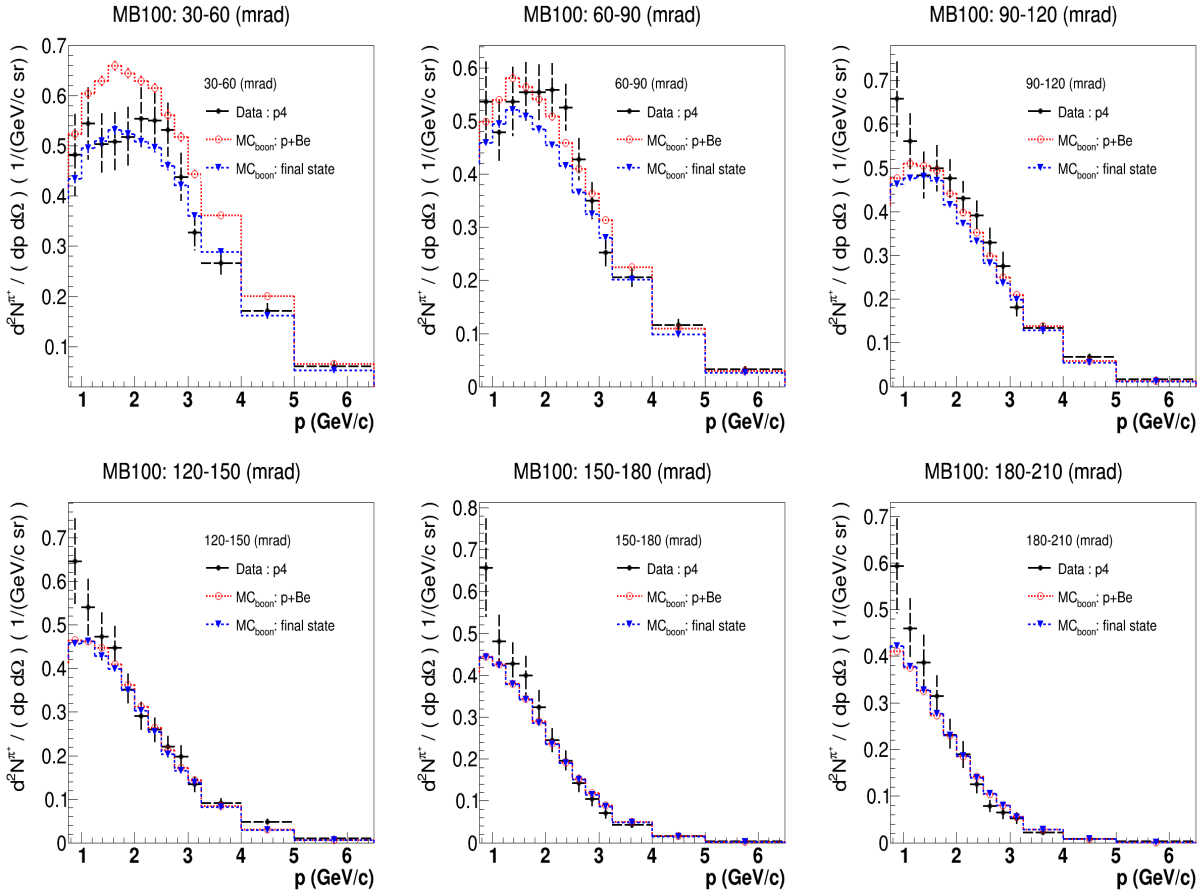

Figure 7.8: π^+ production yield , $d^2N/(dpd\Omega)$, as a function of momentum p for MB100 data is compared with the MiniBooNE MC predicted yield for 40.0 cm target. Here the red upward triangular distribution is the output from the primary p+Be interaction and the blue downward triangular distribution is the final out coming particles from the target.

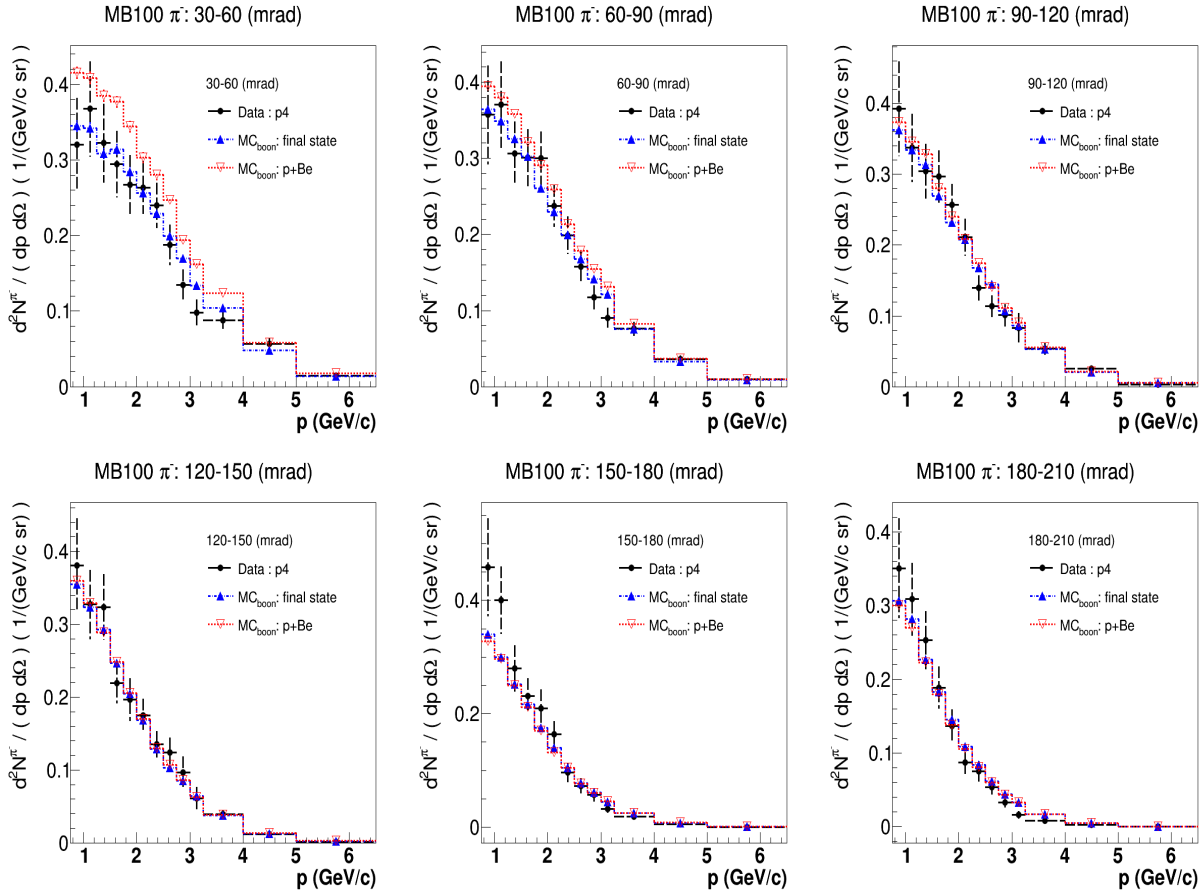

Figure 7.9: π^- production yield , $d^2N/(dpd\Omega)$, as a function of momentum p for MB100 data is compared with the MiniBooNE MC predicted yield for 40.0 cm target. Here the red upward triangular distribution is the output from the primary p+Be interaction and the blue downward triangular distribution is the final out coming particles from the target.

Chapter 8

Sanford-Wang models and ν_μ flux

The Sanford-Wang (SW) model which has fitted parameters as shown in the table 3.2 does not describe well the HARP targets pion production measurements presented in Sec. 7. Therefore, the production results are compared with two modified SW model predictions as described in this chapter. The prediction of ν_μ neutrino flux for MiniBooNE described in [74, 50] is compared with that from the new model predictions by implementing the extended SW model in to the MiniBooNE MC generator.

8.1 Comparison of production results with three SW-type models

In chapter 7, the results of pion production cross section measurements are presented for Be5 target data using VERTEX4 type reconstructed tracks. In order to implement the measured production cross section results for MiniBooNE MC simulation, the results are fitted with a modified Sanford-Wang model described in the HARP article [73]. This article [73] has defined an Extended Sanford-Wang (ESW) model to fit the measured π^+ production cross sections for short beryllium target (Be5) data as described in [73]. The production results which used for this fitting were measured using VERTEX2 type tracks. The ESW model is described for double differential cross sections, $d^2\sigma/(dpd\Omega)$, of secondary meson production with nine parameters, $c_1 - c_9$,

as:

$$\frac{d^2\sigma}{dpd\Omega} = \exp(A)p^{c_2}\left(1-\frac{p}{p_B}\right)\times\left(1+\frac{p}{p_B}\right)^{c_9\theta(p-c_7p_B\cos^{c_8}\theta)} \tag{8.1}$$

where p and θ are the momentum and the angle of outgoing secondary mesons and also p_B is the beam proton momentum. Here the factor A is defined as:

$$A = c_1 - c_3\frac{p^{c_4}}{p_B^{c_5}} - c_6\theta(p - c_7p_B\cos^{c_8}\theta). \tag{8.2}$$

This ESW model fits the π^+ data better than the SW model used in Ref. [50] which is used in the MiniBooNE Monte Carlo generator. The best fitted model parameters for VERTEX2 type production measurements are given in the table 8.1 taken from Ref. [73].

Particle type	c_1	c_2	c_3	c_4	c_5	c_6	c_7	c_8	c_9
π^+	5.13	1.87	6.67	1.56	1.56	11.9	0.173	19.8	16.0

Table 8.1: Best fitted ESW parameters taken from [73] for HARP VERTEX2 type reconstructed tracks of Be5 data.

To fit the cross section measurements of VERTEX4 results shown in the Fig. 7.1 and given in table A.1, a χ^2, defined as:

$$\chi^2 = \sum_{i,j}(Data - ESW)_i M_{ij}^{-1}(Data - ESW)_j, \tag{8.3}$$

where i and j represent given (p,θ) bins and M^{-1} represents the inverse of the covariance matrix of data which included the normalization matrix as describe below. The systematic covariance matrices of absorption correction and tertiary particle correction have completely correlated matrix elements in the kinematical space. These systematics contribute to the overall normalization error. Therefore, the diagonal elements of theses systematics error matrix combine together with the fully correlated overall normalization in the data fitting process as $M(N)_{ii} = 1/\delta_{ii}^2$. This $M(N)_{ii}$ elements are associated with the normalization parameter c_1 of the ESW model to optimize the best model fitting parameters. Rest of the covariance matrices,

corresponding to all other error sources are used as correlated covariance matrix, $M(C)_{ij}$, for fitting algorithm. In the fitting algorithm, the data fit with the model by combining two functions as $\chi^2 = \chi^2_{\rm N} + \chi^2_{\rm C}$. Therefore the term χ^2 can be written as:

$$\chi^2 = \sum_i \frac{(Data - ESW)_i^2}{\delta_{ii}^2} + \sum_{i,j} (Data - ESW)_i M(C)_{ij}^{-1} (Data - ESW)_j, \quad (8.4)$$

To minimize the defined χ^2 for ESW model, eight model parameters are used to fit the data (c_5 is fixed to be equal to c_4). The best fitted ESW model parameters for measured π^+ production cross section for the Be5 target data using VERTEX4 type tracks is given in the table 8.2. The best-fit χ^2 minimum value is $\chi^2_{min} = 125.4$ for 70[1] degrees of freedom. The correlation matrix of the best fitting parameters are shown in

Parameter	Best fit value
c_1	5.39 ± 0.32
c_2	2.30 ± 0.29
c_3	7.19 ± 0.68
$c_4 = c_5$	1.17 ± 0.22
c_6	11.2 ± 0.6
c_7	0.191 ± 0.008
c_8	18.4 ± 1.8
c_9	13.2 ± 1.4

Table 8.2: Best fitted ESW parameters for cross section measurements of VERTEX4 type reconstructed tracks on Be5 target shown in the Tab. A.1.

the table 8.3. The data fitting with three SW models are shown in the Fig. 8.1. The measured VERTEX2 data that we used here for the comparison is taken from the analysis describe in [59].

To compare the pion production from the ESW model predictions with the measured long target data, we have implemented it into Geant4 based MiniBooNE Monte Carlo simulator. This updated MiniBooNE MC predictions of π^+ yields are compared with the measured data on Be5, MB50 and MB100 targets as shown in Fig. 8.2, Fig. 8.3 and Fig. 8.4.

[1]Here we fit 13×6 bins and we have 8 free parameters for fitting function.

parameters	c_1	c_2	c_3	$c_4 = c_5$	c_6	c_7	c_7	c_9
c_1	1							
c_2	0.848	1						
c_3	0.711	0.926	1					
$c_4 = c_5$	-0.975	-0.884	-0.697	1				
c_6	-0.507	-0.056	0.157	0.485	1			
c_7	-0.161	0.090	-0.029	-0.032	0.085	1		
c_8	0.089	0.028	-0.084	-0.184	-0.418	0.723	1	
c_9	-0.534	-0.112	0.157	0.539	0.977	0.0316	-0.390	1

Table 8.3: The correlation coefficients of ESW model parameters which fitted with VERTEX4 type short Be target data.

To compare the goodness of fit of the ESW and SW models predicted π^+ production rates with the measured data, the $\chi^2_{data-MC}$ parameter is defined as:

$$\chi^2_{data-MC} = \sum_{p_i,\theta_j} \frac{\left([d^2N^\pi_{\rm MC}/(dpd\Omega)]_{p_i,\theta_j} - [d^2N^\pi_{\rm data}/(dpd\Omega)]_{p_i,\theta_j}\right)^2}{\delta^2_{\rm data}}, \tag{8.5}$$

where $[d^2N^\pi_{\rm MC}/(dpd\Omega)]_{p_i,\theta_j}$ and $[d^2N^\pi_{\rm data}/(dpd\Omega)]_{p_i,\theta_j}$ are the MC predicted and data measured differential production yields in (p_i, θ_j) bins respectively. The values for $\delta^2_{\rm data}$ are obtained from the uncertainty of measured $[d^2N^\pi_{\rm data}/(dpd\Omega)]_{p_i,\theta_j}$ in the (p_i, θ_j) bin. The $\chi^2_{data-MC}$ is calculated over the parameter space of ranging momentum $0.75 \leq p \leq 6.5$ (GeV/c) and the angle $0.03 \leq \theta \leq 0.21$ (rad). Here each $\chi^2_{data-MC}$ is calculated by summing over each p and θ bins in the binning space of $13 \times 6 = 78$ total number of bins in the parameter space. The calculated $\chi^2_{data-MC}$ is shown in the Table. 8.4. According to the Table 8.4, the ESW:p4 model has better agreement with the measured data for all targets than that from the standard SW model in the MiniBooNE MC and the ESW:p2 model.

8.2 Effects of ESW model on MiniBooNE ν_μ flux

The predictions of muon neutrino fluxes from standard SW model and the ESW models are compared as shown in Fig. 8.5. The muon neutrino flux for MiniBooNE

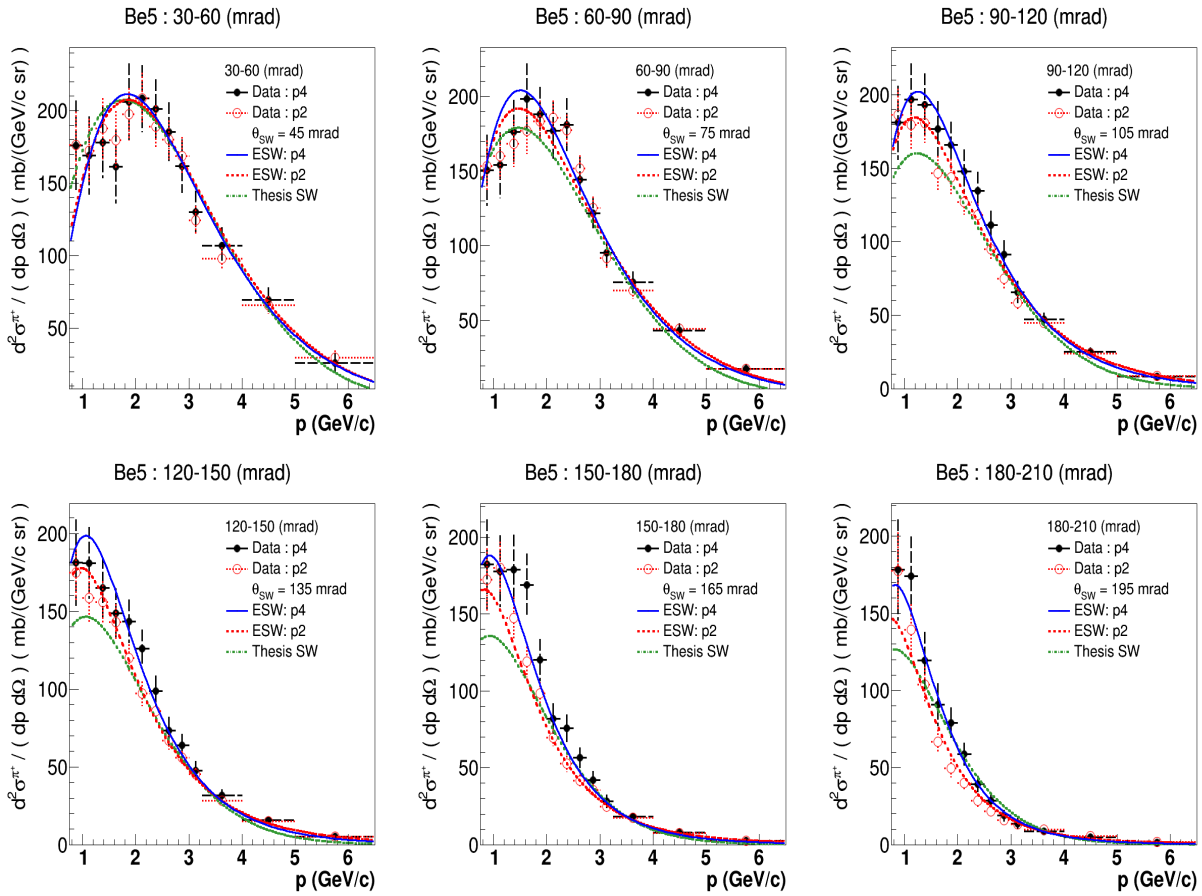

Figure 8.1: The best fitting of SW and ESW models with measured π^+ production cross sections. Here ESW:p4 (blue-solid) and ESW:p2 (red-dashed) are compared with the cross sections of p_2 (red-square) and p_4 (black-dots) data and thesis SW model [59] (green-dashed-dotted).

momentum range (GeV/c)	$0.75 \leq p \leq 5.0$		
angular range (rad)	$0.03 \leq \theta \leq 0.21$		
Total number of bins	$N_{bins} = 72$		
Target	Be5	MB50	MB100
$\chi^2_{data-MC}$ (ESW:p4)	68.0	68.6	54.3
$\chi^2_{data-MC}$ (ESW:p2)	140.9	72.6	67.7
$\chi^2_{data-MC}$ (SW:p2)	198.0	148.2	95.9

Table 8.4: According to Eq. (8.5), the calculated $\chi^2_{data-MC}$ values by using π^+ production from the simulated ESW and standard SW models on beamline MC and p_4 data for Be5, MB50 and MB100 targets.

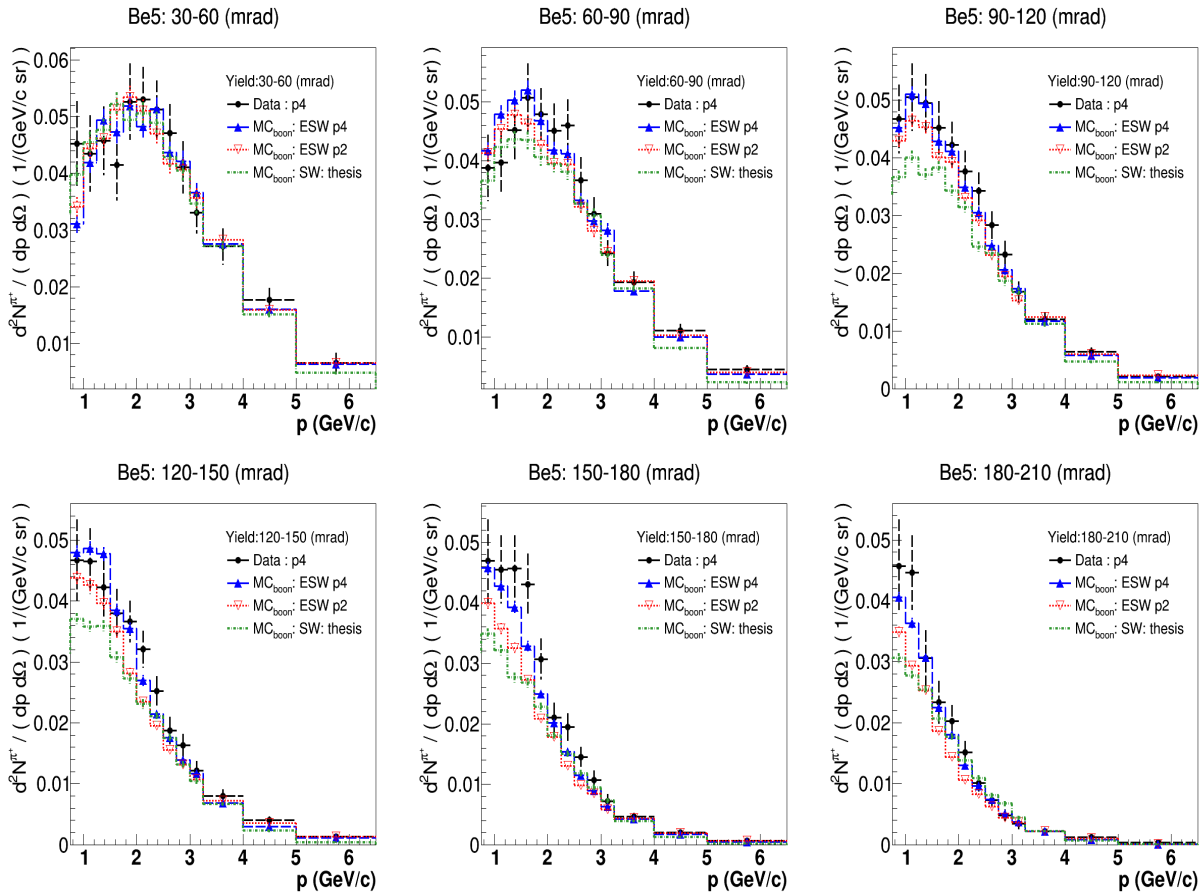

Figure 8.2: π^+ production yield , $d^2N/(dpd\Omega)$, as a function of momentum p for Be5 is compared with the MiniBooNE MC predicted π^+ yield for 2.0 cm target. Here the red downward and blue upward triangular distributions are the MiniBooNE MC predictions of π^+ yield from the primary p+Be interactions for simulated standard SW and ESW models respectively.

experiment has been predicted by simulating primary p+Be interactions from the standard SW model parameters as described in [59]. The ratio of the integrated fluxes of $ESW : p4(\pi^+ \rightarrow \nu_\mu)$ to $SW : p2(\pi^+ \rightarrow \nu_\mu)$ from [0 - 3.0 GeV] shows a 6.0% increase of ESW:p4 model prediction over the standard SW model prediction.

8.3 Extrapolation from short to long

The extrapolation from short target to long target used in the Geant4 simulation needs to be checked. Therefore, we have compared various ratios of predicted pions as described in this section. This test can be formulated by defining the extrapolation

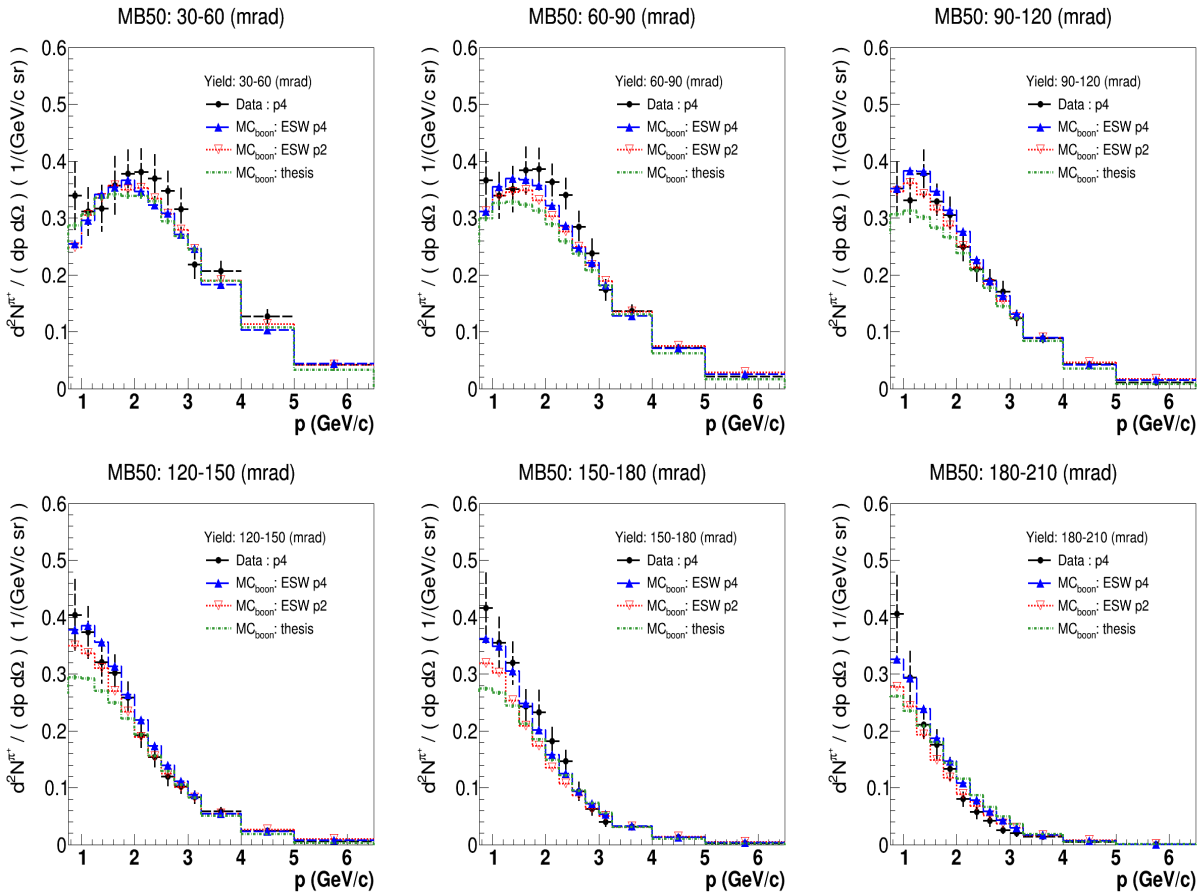

Figure 8.3: π^+ production yield , $d^2N/(dpd\Omega)$, as a function of momentum p for MB50 data is compared with the MiniBooNE MC predicted yield for 20.0 cm target. Here the red downward and blue upward triangular distributions are the MiniBooNE MC predictions of π^+ yield from the primary p+Be interactions for simulated standard SW and ESW models respectively.

parameters of $\eta_{5\%\lambda\to100\%\lambda_I}$, $\eta_{5\%\lambda\to50\%\lambda_I}$ and $\eta_{50\%\lambda\to100\%\lambda_I}$ for 2 cm to 40 cm, 2 cm to 20 cm and 20 cm to 40 cm respectively as:

$$\eta_{5\%\lambda\to100\%\lambda_I} = \left\{\frac{N_{100\%\lambda_I}}{\sigma_{5\%\lambda_I}}\right\}^{DATA} \cdot \left\{\frac{\sigma_{5\%\lambda_I}}{N_{100\%\lambda_I}}\right\}^{MC}$$

$$\eta_{5\%\lambda\to50\%\lambda_I} = \left\{\frac{N_{50\%\lambda_I}}{\sigma_{5\%\lambda_I}}\right\}^{DATA} \cdot \left\{\frac{\sigma_{5\%\lambda_I}}{N_{50\%\lambda_I}}\right\}^{MC} \tag{8.6}$$

$$\eta_{50\%\lambda\to100\%\lambda_I} = \left\{\frac{N_{100\%\lambda_I}}{N_{50\%\lambda_I}}\right\}^{DATA} \cdot \left\{\frac{N_{50\%\lambda_I}}{N_{100\%\lambda_I}}\right\}^{MC}$$

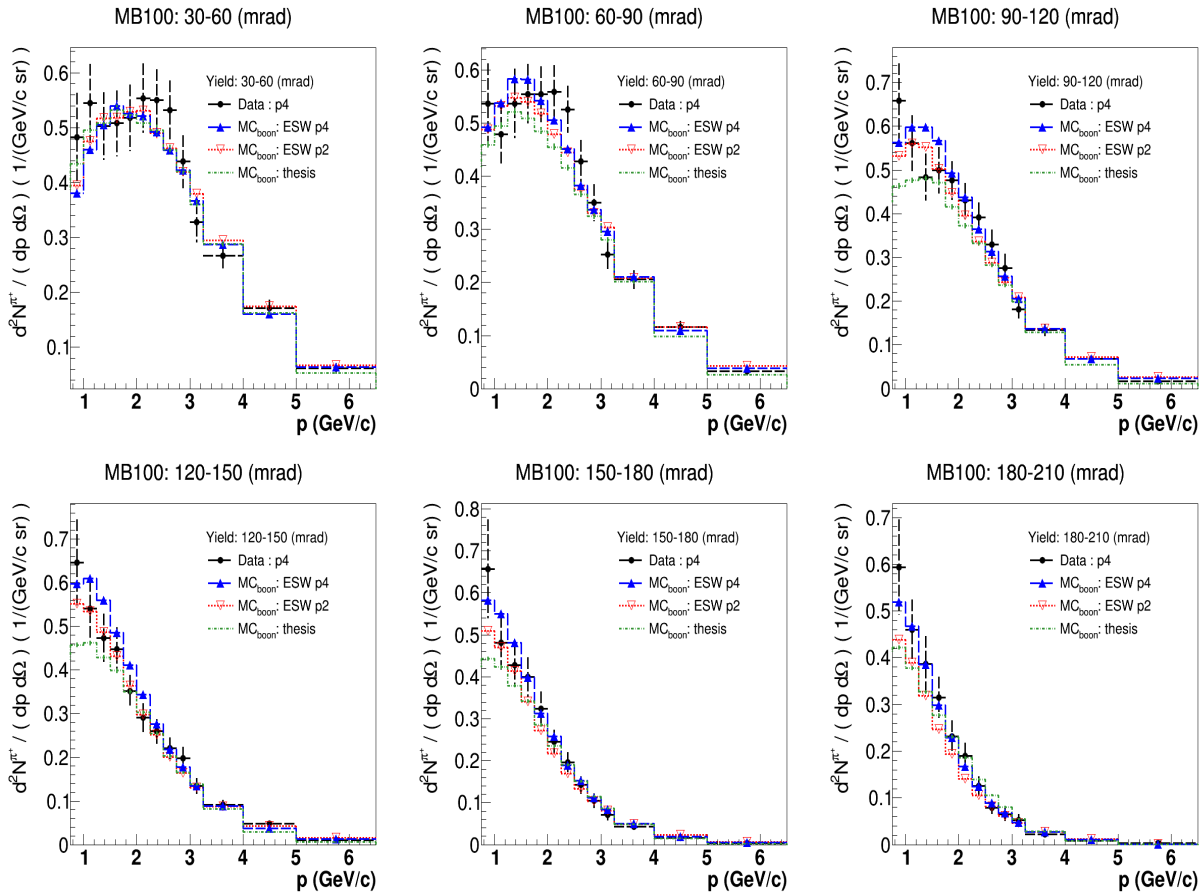

Figure 8.4: π^+ production yield , $d^2N/(dpd\Omega)$, as a function of momentum p for MB100 data is compared with the MiniBooNE MC predicted yield for 40.0 cm target. Here the red downward and blue upward triangular distributions are the MiniBooNE MC predictions of π^+ yield from the primary p+Be interactions for simulated standard SW and ESW models respectively.

where σs represent the cross sections from 2 cm Be target and Ns represent the yields from long targets in data and MC. The extrapolation parameters should be close to 1.0. The uncertainties of the three extrapolation parameters can be derived as:

$$\delta\eta = \eta \left[\sum_{data,MC} \left(\frac{\delta N}{N} \right)^2 + \sum_{data,MC} \left(\frac{\delta\sigma}{\sigma} \right)^2 \right]^{1/2} \tag{8.7}$$

The extrapolation parameters for $\pi^\pm$ particle productions using HARP data measurements and MiniBooNE MC simulation predictions is given in the table 8.5.

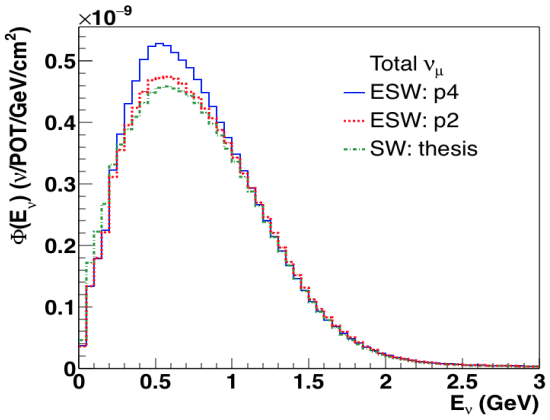

Figure 8.5: The comparison of total ν_μ flux from all possible decay modes for EWS:p4 (blue), ESW:p2 (red) and SW:p2 (green) model predictions.

Particle	π^+		π^-
Model	ESW:p4	Thesis SW	Thesis SW
$\eta_{5\%\lambda\to100\%\lambda_I}$	0.97 ± 0.02	1.05 ± 0.02	0.95 ± 0.03
$\eta_{5\%\lambda\to50\%\lambda_I}$	0.96 ± 0.02	1.03 ± 0.02	1.03 ± 0.03
$\eta_{50\%\lambda\to100\%\lambda_I}$	0.99 ± 0.02	0.98 ± 0.02	1.08 ± 0.03

Table 8.5: According to Eq. (8.6), the calculated extrapolation parameters of η by using $\pi^\pm$ production data and MC for 2 cm, 20 cm and 40 cm targets. The uncertainties are estimated by Eq. 8.7

Chapter 9

Conclusions

The measurements of secondary hadron production are an important input to an event simulator to generate MC neutrino flux. In the previous studies, the pion production cross section results from the short beryllium target HARP data analysis has provided the fitted SW model parameters for the neutrino event generator in MiniBooNE experiment.

This thesis describes the pion production rates from the long beryllium target data measurements which can be used to understand the extrapolation of secondary pion productions from short to long target. The identified systematics are also described in this thesis.

Both π^+ and π^- production cross section measurements from the short Be target data consistent with the previously measured production cross sections. The simulated π^+ production cross sections using the parameterization of extended SW model (ESW:p4) shows a better agreement with the VERTEX4 type production measurement from short target data. π^- yield measurements from long targets is higher than the MiniBooNE MC predictions in some higher angular bins.

ν_μ neutrino flux prediction from the π^+ decay mode is compared for both standard and extended SW model (ESW:p4) simulations. The comparison shows a 6.1% increase of ν_μ neutrino flux from extended SW model prediction as compared to the standard

SW model prediction.

The study of the extrapolation from short to long target pion productions in the MiniBooNE MC indicates a close agreement with the data. That implies the Geant4 simulation in the MiniBooNE MC models the behavior of the hadrons after the first interaction well. The systematic error on the extrapolation is 2%.

Appendix A

Short target cross section data

The measured double-differential cross sections of π^+, π^- and proton production from the 8.9 GeV/c proton-beryllium interactions of short beryllium target data using the VERTEX4 algorithm are tabulated in this appendix. The table contains measurements and their estimated diagonal errors of the full covariance matrix. Measurements are tabulated in the momentum bins of 0.75 GeV/c - 6.5 GeV/c and the polar angular bins of 30 mrad - 210 mrad.

Table A.1: $\pi^{\pm}$ and proton production cross sections , $d^2\sigma/(dpd\Omega)$, for proton (8.9 GeV/c) + Be5 target interaction.

				π^+	π^-	p
θ_{min} (mrad)	θ_{max} (mrad)	p_{min} (GeV/c)	p_{max} (GeV/c)	$d^2\sigma^{\pi^+}/(dpd\Omega)$ mb/(GeV/c sr)	$d^2\sigma^{\pi^-}/(dpd\Omega)$ mb/(GeV/c sr)	$d^2\sigma^{p}/(dpd\Omega)$ mb/(GeV/c sr)
30	60	0.75	1.00	176.0 ± 30.9	127.5 ± 25.8	81.5 ± 15.5
		1.00	1.25	169.2 ± 26.9	163.8 ± 28.6	85.8 ± 13.8
		1.25	1.50	178.0 ± 24.3	140.3 ± 19.8	91.6 ± 12.6
		1.50	1.75	161.2 ± 25.2	106.3 ± 20.2	85.5 ± 11.9
		1.75	2.00	206.1 ± 26.3	96.6 ± 15.0	84.8 ± 14.2
		2.00	2.25	208.3 ± 22.8	100.9 ± 15.0	102.3 ± 13.2
		2.25	2.50	201.2 ± 20.5	90.1 ± 14.0	116.5 ± 14.7
		2.50	2.75	185.5 ± 20.0	77.4 ± 12.4	118.6 ± 17.2
		2.75	3.00	161.8 ± 18.3	65.1 ± 10.9	147.1 ± 17.3
		3.00	3.25	130.1 ± 14.5	42.7 ± 10.1	154.4 ± 17.6
		3.25	4.00	106.8 ± 12.7	40.5 ± 5.4	182.3 ± 24.3
		4.00	5.00	69.5 ± 8.3	22.3 ± 3.7	267.8 ± 30.8
		5.00	6.50	25.9 ± 7.1	5.7 ± 1.6	412.8 ± 35.5
60	90	0.75	1.00	150.5 ± 23.7	111.1 ± 20.9	93.0 ± 12.9
		1.00	1.25	154.1 ± 21.9	121.9 ± 17.9	80.5 ± 10.5
		1.25	1.50	176.1 ± 21.4	116.2 ± 16.8	76.7 ± 10.8
		1.50	1.75	198.4 ± 23.4	134.1 ± 15.6	85.3 ± 10.7
		1.75	2.00	188.0 ± 18.0	120.0 ± 11.9	96.7 ± 10.9
		2.00	2.25	177.2 ± 18.6	99.3 ± 10.4	93.2 ± 10.1
		2.25	2.50	181.1 ± 17.5	79.2 ± 10.1	97.3 ± 11.4
		2.50	2.75	144.4 ± 15.4	52.5 ± 8.7	106.2 ± 10.6
		2.75	3.00	121.8 ± 11.3	42.8 ± 6.5	112.6 ± 11.3
		3.00	3.25	95.4 ± 8.8	34.0 ± 5.2	122.8 ± 13.5
		3.25	4.00	75.9 ± 7.1	28.7 ± 3.5	152.6 ± 15.4
		4.00	5.00	43.4 ± 4.7	13.5 ± 2.1	197.5 ± 15.1
		5.00	6.50	17.7 ± 2.8	2.5 ± 1.3	218.8 ± 16.5

				π^+	π^-	p
θ_{min} (mrad)	θ_{max} (mrad)	p_{min} (GeV/c)	p_{max} (GeV/c)	$d^2\sigma^{\pi^+}/(dpd\Omega)$ mb/(GeV/c sr)	$d^2\sigma^{\pi^-}/(dpd\Omega)$ mb/(GeV/c sr)	$d^2\sigma^{p}/(dpd\Omega)$ mb/(GeV/c sr)
90	120	0.75	1.00	181.1 ± 25.1	148.6 ± 26.9	97.7 ± 13.3
		1.00	1.25	196.7 ± 24.5	140.0 ± 20.5	86.5 ± 10.5
		1.25	1.50	193.3 ± 21.2	123.0 ± 15.4	92.1 ± 11.0
		1.50	1.75	176.8 ± 18.7	109.4 ± 12.6	82.2 ± 9.4
		1.75	2.00	165.8 ± 16.0	87.4 ± 9.9	73.2 ± 9.6
		2.00	2.25	148.0 ± 14.6	71.1 ± 8.5	68.4 ± 11.6
		2.25	2.50	134.7 ± 12.9	59.2 ± 6.8	86.4 ± 10.5
		2.50	2.75	111.5 ± 9.4	44.0 ± 6.9	91.3 ± 9.3
		2.75	3.00	91.4 ± 9.5	35.1 ± 5.2	87.8 ± 9.0
		3.00	3.25	65.8 ± 7.4	27.9 ± 3.6	85.9 ± 11.1
		3.25	4.00	47.2 ± 4.6	18.8 ± 2.8	115.8 ± 10.5
		4.00	5.00	25.1 ± 3.1	8.2 ± 1.4	123.4 ± 7.7
		5.00	6.50	8.5 ± 1.6	1.2 ± 0.4	97.4 ± 8.8
120	150	0.75	1.00	181.2 ± 27.6	137.8 ± 23.2	77.3 ± 13.2
		1.00	1.25	181.1 ± 22.8	131.1 ± 19.0	82.2 ± 11.4
		1.25	1.50	165.2 ± 19.6	123.5 ± 16.1	84.0 ± 10.1
		1.50	1.75	148.7 ± 16.1	110.7 ± 13.3	83.3 ± 9.3
		1.75	2.00	143.6 ± 13.8	85.2 ± 10.0	77.1 ± 9.9
		2.00	2.25	126.2 ± 12.0	69.1 ± 8.8	73.9 ± 10.3
		2.25	2.50	98.8 ± 9.6	45.7 ± 6.5	78.9 ± 9.1
		2.50	2.75	73.3 ± 8.8	32.7 ± 5.0	85.1 ± 10.0
		2.75	3.00	63.9 ± 7.2	25.4 ± 4.1	94.7 ± 10.5
		3.00	3.25	47.6 ± 6.0	18.1 ± 2.7	92.8 ± 8.6
		3.25	4.00	31.6 ± 3.9	13.0 ± 2.0	89.7 ± 7.3
		4.00	5.00	15.7 ± 2.3	4.4 ± 0.9	73.4 ± 6.7
		5.00	6.50	5.1 ± 0.6	0.4 ± 0.2	46.6 ± 4.1

				π^+	π^-	p
θ_{min} (mrad)	θ_{max} (mrad)	p_{min} (GeV/c)	p_{max} (GeV/c)	$d^2\sigma^{\pi^+}/(dpd\Omega)$ mb/(GeV/c sr)	$d^2\sigma^{\pi^-}/(dpd\Omega)$ mb/(GeV/c sr)	$d^2\sigma^{p}/(dpd\Omega)$ mb/(GeV/c sr)
150	180	0.75	1.00	182.3 ± 29.0	150.7 ± 27.0	86.6 ± 12.6
		1.00	1.25	177.8 ± 23.3	128.9 ± 21.0	82.3 ± 10.1
		1.25	1.50	178.9 ± 22.3	112.8 ± 15.7	87.3 ± 10.3
		1.50	1.75	169.0 ± 20.3	85.6 ± 10.9	84.0 ± 12.0
		1.75	2.00	120.1 ± 13.6	61.0 ± 9.4	77.4 ± 10.1
		2.00	2.25	81.9 ± 9.8	46.6 ± 7.2	79.2 ± 9.6
		2.25	2.50	75.8 ± 8.8	33.8 ± 5.9	83.3 ± 10.1
		2.50	2.75	56.6 ± 6.5	25.3 ± 4.0	73.8 ± 9.5
		2.75	3.00	42.0 ± 6.0	19.9 ± 3.1	70.3 ± 9.1
		3.00	3.25	28.3 ± 4.3	11.5 ± 2.7	68.4 ± 8.1
		3.25	4.00	18.2 ± 2.5	7.4 ± 1.6	58.6 ± 5.8
		4.00	5.00	7.9 ± 1.2	1.7 ± 0.5	42.1 ± 4.3
		5.00	6.50	2.7 ± 0.4	0.10 ± 0.05	18.4 ± 2.5
180	210	0.75	1.00	178.2 ± 32.5	142.9 ± 28.8	82.5 ± 14.8
		1.00	1.25	174.2 ± 25.4	121.5 ± 19.3	79.8 ± 10.4
		1.25	1.50	119.5 ± 18.3	85.1 ± 15.1	62.1 ± 10.9
		1.50	1.75	90.9 ± 13.9	70.9 ± 12.6	57.9 ± 9.4
		1.75	2.00	78.9 ± 10.2	52.7 ± 8.5	54.2 ± 8.2
		2.00	2.25	58.7 ± 7.4	40.9 ± 6.3	48.9 ± 7.1
		2.25	2.50	39.4 ± 5.1	27.8 ± 4.4	38.8 ± 6.2
		2.50	2.75	28.4 ± 4.0	17.6 ± 3.8	33.5 ± 5.4
		2.75	3.00	18.8 ± 3.5	10.8 ± 2.4	29.5 ± 4.8
		3.00	3.25	13.6 ± 3.5	7.1 ± 1.7	30.1 ± 5.2
		3.25	4.00	8.7 ± 2.0	3.1 ± 1.0	24.7 ± 3.7
		4.00	5.00	4.9 ± 0.8	0.5 ± 0.2	14.9 ± 2.3
		5.00	6.50	1.3 ± 0.2	0.03 ± 0.02	6.1 ± 1.4

Appendix B

Harp targets π^+ yield data

The measured double-differential yield of π^+ production from the 8.9 GeV/c proton-beryllium interactions of HARP data are tabulated in this appendix. The productions of π^+ from the three Be targets of 2 cm, 20 cm and 40 cm are presented in the table. The table contains measurements and their estimated diagonal errors of the full covariance matrix. Measurements are tabulated in the momentum bins of 0.75 GeV/c - 6.5 GeV/c and the polar angular bins of 30 mrad - 210 mrad.

Table B.1: π^+ production yield , $d^2N/(dpd\Omega)$, as a function of momentum p for MB100, MB50 and Be5 targets data.

				Be5	MB50	MB100
θ_{min} (mrad)	θ_{max} (mrad)	p_{min} (GeV/c)	p_{max} (GeV/c)	$d^2N^{\pi^+}/(dpd\Omega)$ 1/(GeV/c sr)	$d^2N^{\pi^+}/(dpd\Omega)$ 1/(GeV/c sr)	$d^2N^{\pi^+}/(dpd\Omega)$ 1/(GeV/c sr)
30	60	0.75	1.00	0.045 ± 0.007	0.340 ± 0.060	0.483 ± 0.081
		1.00	1.25	0.043 ± 0.007	0.312 ± 0.042	0.544 ± 0.072
		1.25	1.50	0.046 ± 0.006	0.317 ± 0.041	0.503 ± 0.061
		1.50	1.75	0.041 ± 0.006	0.357 ± 0.052	0.508 ± 0.059
		1.75	2.00	0.053 ± 0.007	0.378 ± 0.042	0.518 ± 0.060
		2.00	2.25	0.053 ± 0.006	0.381 ± 0.041	0.554 ± 0.063
		2.25	2.50	0.051 ± 0.005	0.370 ± 0.042	0.550 ± 0.056
		2.50	2.75	0.047 ± 0.005	0.348 ± 0.035	0.532 ± 0.053
		2.75	3.00	0.041 ± 0.005	0.316 ± 0.037	0.438 ± 0.048
		3.00	3.25	0.033 ± 0.004	0.218 ± 0.029	0.328 ± 0.036
		3.25	4.00	0.027 ± 0.003	0.207 ± 0.018	0.267 ± 0.022
		4.00	5.00	0.018 ± 0.002	0.127 ± 0.012	0.171 ± 0.015
		5.00	6.50	0.007 ± 0.002	0.043 ± 0.007	0.061 ± 0.009
60	90	0.75	1.00	0.039 ± 0.006	0.366 ± 0.051	0.536 ± 0.075
		1.00	1.25	0.040 ± 0.005	0.340 ± 0.041	0.479 ± 0.060
		1.25	1.50	0.045 ± 0.005	0.351 ± 0.040	0.537 ± 0.065
		1.50	1.75	0.051 ± 0.006	0.384 ± 0.042	0.555 ± 0.056
		1.75	2.00	0.048 ± 0.004	0.386 ± 0.037	0.554 ± 0.052
		2.00	2.25	0.045 ± 0.005	0.363 ± 0.032	0.559 ± 0.051
		2.25	2.50	0.046 ± 0.004	0.341 ± 0.030	0.526 ± 0.044
		2.50	2.75	0.037 ± 0.004	0.285 ± 0.027	0.428 ± 0.039
		2.75	3.00	0.031 ± 0.003	0.238 ± 0.026	0.350 ± 0.034
		3.00	3.25	0.024 ± 0.002	0.174 ± 0.018	0.253 ± 0.028
		3.25	4.00	0.019 ± 0.002	0.137 ± 0.012	0.206 ± 0.017
		4.00	5.00	0.011 ± 0.001	0.072 ± 0.006	0.116 ± 0.011
		5.00	6.50	0.005 ± 0.001	0.022 ± 0.004	0.033 ± 0.005

				Be5	MB50	MB100
θ_{min} (mrad)	θ_{max} (mrad)	p_{min} (GeV/c)	p_{max} (GeV/c)	$d^2N^{\pi^+}/(dpd\Omega)$ 1/(GeV/c sr)	$d^2N^{\pi^+}/(dpd\Omega)$ 1/(GeV/c sr)	$d^2N^{\pi^+}/(dpd\Omega)$ 1/(GeV/c sr)
90	120	0.75	1.00	0.047 ± 0.006	0.352 ± 0.048	0.658 ± 0.085
		1.00	1.25	0.051 ± 0.006	0.331 ± 0.040	0.561 ± 0.063
		1.25	1.50	0.050 ± 0.005	0.378 ± 0.042	0.484 ± 0.053
		1.50	1.75	0.045 ± 0.005	0.329 ± 0.031	0.499 ± 0.053
		1.75	2.00	0.042 ± 0.004	0.306 ± 0.032	0.476 ± 0.044
		2.00	2.25	0.038 ± 0.004	0.249 ± 0.025	0.431 ± 0.040
		2.25	2.50	0.034 ± 0.003	0.210 ± 0.021	0.391 ± 0.035
		2.50	2.75	0.028 ± 0.002	0.190 ± 0.020	0.330 ± 0.034
		2.75	3.00	0.023 ± 0.002	0.171 ± 0.018	0.276 ± 0.033
		3.00	3.25	0.017 ± 0.002	0.124 ± 0.014	0.182 ± 0.021
		3.25	4.00	0.012 ± 0.001	0.089 ± 0.009	0.134 ± 0.012
		4.00	5.00	0.006 ± 0.001	0.044 ± 0.005	0.068 ± 0.007
		5.00	6.50	0.0022 ± 0.0004	0.011 ± 0.002	0.018 ± 0.004
120	150	0.75	1.00	0.047 ± 0.007	0.404 ± 0.063	0.647 ± 0.098
		1.00	1.25	0.047 ± 0.005	0.373 ± 0.046	0.540 ± 0.065
		1.25	1.50	0.042 ± 0.005	0.321 ± 0.038	0.474 ± 0.055
		1.50	1.75	0.038 ± 0.004	0.303 ± 0.032	0.448 ± 0.049
		1.75	2.00	0.037 ± 0.003	0.259 ± 0.028	0.351 ± 0.037
		2.00	2.25	0.032 ± 0.003	0.192 ± 0.021	0.291 ± 0.032
		2.25	2.50	0.025 ± 0.002	0.154 ± 0.017	0.260 ± 0.028
		2.50	2.75	0.019 ± 0.002	0.119 ± 0.016	0.220 ± 0.024
		2.75	3.00	0.016 ± 0.002	0.103 ± 0.013	0.198 ± 0.025
		3.00	3.25	0.012 ± 0.002	0.083 ± 0.011	0.135 ± 0.018
		3.25	4.00	0.008 ± 0.001	0.059 ± 0.008	0.092 ± 0.010
		4.00	5.00	0.004 ± 0.001	0.024 ± 0.003	0.049 ± 0.006
		5.00	6.50	0.0013 ± 0.0001	0.005 ± 0.002	0.011 ± 0.003

				Be5	MB50	MB100
θ_{min} (mrad)	θ_{max} (mrad)	p_{min} (GeV/c)	p_{max} (GeV/c)	$d^2N^{\pi^+}/(dpd\Omega)$ 1/(GeV/c sr)	$d^2N^{\pi^+}/(dpd\Omega)$ 1/(GeV/c sr)	$d^2N^{\pi^+}/(dpd\Omega)$ 1/(GeV/c sr)
150	180	0.75	1.00	0.047 ± 0.007	0.416 ± 0.062	0.657 ± 0.117
		1.00	1.25	0.046 ± 0.006	0.355 ± 0.045	0.482 ± 0.063
		1.25	1.50	0.046 ± 0.005	0.319 ± 0.038	0.428 ± 0.051
		1.50	1.75	0.043 ± 0.005	0.244 ± 0.030	0.399 ± 0.046
		1.75	2.00	0.031 ± 0.003	0.233 ± 0.039	0.324 ± 0.040
		2.00	2.25	0.021 ± 0.002	0.182 ± 0.024	0.245 ± 0.029
		2.25	2.50	0.019 ± 0.002	0.147 ± 0.020	0.197 ± 0.023
		2.50	2.75	0.015 ± 0.002	0.094 ± 0.016	0.143 ± 0.020
		2.75	3.00	0.011 ± 0.002	0.063 ± 0.012	0.105 ± 0.017
		3.00	3.25	0.007 ± 0.001	0.040 ± 0.008	0.071 ± 0.012
		3.25	4.00	0.005 ± 0.001	0.032 ± 0.005	0.044 ± 0.007
		4.00	5.00	0.0020 ± 0.0003	0.013 ± 0.002	0.016 ± 0.004
		5.00	6.50	0.0007 ± 0.0001	0.003 ± 0.001	0.003 ± 0.001
180	210	0.75	1.00	0.046 ± 0.008	0.406 ± 0.069	0.594 ± 0.101
		1.00	1.25	0.045 ± 0.006	0.294 ± 0.047	0.459 ± 0.065
		1.25	1.50	0.031 ± 0.005	0.212 ± 0.029	0.387 ± 0.058
		1.50	1.75	0.023 ± 0.003	0.176 ± 0.027	0.315 ± 0.044
		1.75	2.00	0.020 ± 0.003	0.134 ± 0.021	0.232 ± 0.034
		2.00	2.25	0.015 ± 0.002	0.080 ± 0.013	0.189 ± 0.028
		2.25	2.50	0.010 ± 0.001	0.058 ± 0.013	0.126 ± 0.019
		2.50	2.75	0.007 ± 0.001	0.042 ± 0.010	0.079 ± 0.013
		2.75	3.00	0.005 ± 0.001	0.026 ± 0.007	0.065 ± 0.013
		3.00	3.25	0.003 ± 0.001	0.020 ± 0.005	0.053 ± 0.012
		3.25	4.00	0.002 ± 0.001	0.014 ± 0.003	0.023 ± 0.006
		4.00	5.00	0.0013 ± 0.0002	0.005 ± 0.001	0.009 ± 0.003
		5.00	6.50	0.0003 ± 0.0001	0.001 ± 0.001	0.003 ± 0.001

Appendix C

Harp Targets π^- Yield Data

The measured double-differential yield of π^- production from the 8.9 GeV/c proton-beryllium interactions of HARP data are tabulated in this appendix. The productions of π^- from the three Be targets of 2 cm, 20 cm and 40 cm are presented in the table. The table contains measurements and their estimated diagonal errors of the full covariance matrix. Measurements are tabulated in the momentum bins of 0.75 GeV/c - 6.5 GeV/c and the polar angular bins of 30 mrad - 210 mrad.

Table C.1: π^- production yield , $d^2N/(dpd\Omega)$, as a function of momentum p for MB100, MB50 and Be5 targets data.

				Be5	MB50	MB100
θ_{min} (mrad)	θ_{max} (mrad)	p_{min} (GeV/c)	p_{max} (GeV/c)	$d^2N^{\pi^-}/(dpd\Omega)$ 1/(GeV/c sr)	$d^2N^{\pi^-}/(dpd\Omega)$ 1/(GeV/c sr)	$d^2N^{\pi^-}/(dpd\Omega)$ 1/(GeV/c sr)
30	60	0.75	1.00	0.033 ± 0.006	0.232 ± 0.045	0.320 ± 0.061
		1.00	1.25	0.042 ± 0.007	0.246 ± 0.043	0.367 ± 0.062
		1.25	1.50	0.036 ± 0.005	0.295 ± 0.046	0.322 ± 0.052
		1.50	1.75	0.027 ± 0.005	0.258 ± 0.038	0.294 ± 0.044
		1.75	2.00	0.025 ± 0.004	0.236 ± 0.032	0.267 ± 0.039
		2.00	2.25	0.026 ± 0.004	0.191 ± 0.025	0.263 ± 0.035
		2.25	2.50	0.023 ± 0.003	0.137 ± 0.020	0.240 ± 0.030
		2.50	2.75	0.020 ± 0.003	0.106 ± 0.015	0.188 ± 0.027
		2.75	3.00	0.017 ± 0.003	0.095 ± 0.014	0.134 ± 0.021
		3.00	3.25	0.011 ± 0.002	0.072 ± 0.013	0.098 ± 0.017
		3.25	4.00	0.010 ± 0.001	0.065 ± 0.008	0.088 ± 0.011
		4.00	5.00	0.006 ± 0.001	0.035 ± 0.005	0.057 ± 0.007
		5.00	6.50	0.0014 ± 0.0004	0.008 ± 0.002	0.015 ± 0.004
60	90	0.75	1.00	0.029 ± 0.005	0.225 ± 0.042	0.357 ± 0.065
		1.00	1.25	0.031 ± 0.005	0.246 ± 0.037	0.371 ± 0.056
		1.25	1.50	0.030 ± 0.004	0.228 ± 0.032	0.306 ± 0.042
		1.50	1.75	0.034 ± 0.004	0.211 ± 0.026	0.301 ± 0.037
		1.75	2.00	0.031 ± 0.003	0.218 ± 0.027	0.300 ± 0.035
		2.00	2.25	0.025 ± 0.003	0.178 ± 0.020	0.238 ± 0.027
		2.25	2.50	0.020 ± 0.002	0.132 ± 0.016	0.199 ± 0.024
		2.50	2.75	0.013 ± 0.002	0.107 ± 0.014	0.158 ± 0.020
		2.75	3.00	0.011 ± 0.002	0.092 ± 0.014	0.117 ± 0.015
		3.00	3.25	0.009 ± 0.001	0.056 ± 0.012	0.090 ± 0.013
		3.25	4.00	0.007 ± 0.001	0.045 ± 0.006	0.076 ± 0.009
		4.00	5.00	0.003 ± 0.001	0.023 ± 0.003	0.036 ± 0.005
		5.00	6.50	0.0006 ± 0.0003	0.006 ± 0.002	0.009 ± 0.003

				Be5	MB50	MB100
θ_{min}	θ_{max}	p_{min}	p_{max}	$d^2N^{\pi^-}/(dpd\Omega)$	$d^2N^{\pi^-}/(dpd\Omega)$	$d^2N^{\pi^-}/(dpd\Omega)$
(mrad)	(mrad)	(GeV/c)	(GeV/c)	1/(GeV/c sr)	1/(GeV/c sr)	1/(GeV/c sr)
90	120	0.75	1.00	0.038 ± 0.007	0.253 ± 0.043	0.393 ± 0.066
		1.00	1.25	0.036 ± 0.005	0.252 ± 0.038	0.337 ± 0.048
		1.25	1.50	0.032 ± 0.004	0.237 ± 0.030	0.304 ± 0.038
		1.50	1.75	0.028 ± 0.003	0.198 ± 0.024	0.297 ± 0.037
		1.75	2.00	0.022 ± 0.003	0.166 ± 0.019	0.257 ± 0.029
		2.00	2.25	0.018 ± 0.002	0.140 ± 0.017	0.211 ± 0.026
		2.25	2.50	0.015 ± 0.002	0.107 ± 0.014	0.139 ± 0.018
		2.50	2.75	0.011 ± 0.002	0.080 ± 0.011	0.114 ± 0.015
		2.75	3.00	0.009 ± 0.001	0.060 ± 0.010	0.101 ± 0.016
		3.00	3.25	0.007 ± 0.001	0.047 ± 0.014	0.083 ± 0.021
		3.25	4.00	0.005 ± 0.001	0.030 ± 0.005	0.054 ± 0.008
		4.00	5.00	0.0021 ± 0.0003	0.014 ± 0.003	0.025 ± 0.004
		5.00	6.50	0.0003 ± 0.0001	0.003 ± 0.001	0.003 ± 0.001
120	150	0.75	1.00	0.036 ± 0.006	0.278 ± 0.049	0.381 ± 0.064
		1.00	1.25	0.034 ± 0.005	0.219 ± 0.033	0.327 ± 0.047
		1.25	1.50	0.032 ± 0.004	0.218 ± 0.031	0.324 ± 0.045
		1.50	1.75	0.028 ± 0.003	0.168 ± 0.023	0.219 ± 0.027
		1.75	2.00	0.022 ± 0.003	0.159 ± 0.022	0.197 ± 0.029
		2.00	2.25	0.018 ± 0.002	0.130 ± 0.018	0.175 ± 0.022
		2.25	2.50	0.012 ± 0.002	0.089 ± 0.012	0.135 ± 0.018
		2.50	2.75	0.008 ± 0.001	0.078 ± 0.012	0.124 ± 0.020
		2.75	3.00	0.006 ± 0.001	0.057 ± 0.011	0.096 ± 0.022
		3.00	3.25	0.005 ± 0.001	0.037 ± 0.008	0.061 ± 0.015
		3.25	4.00	0.003 ± 0.000	0.023 ± 0.004	0.039 ± 0.006
		4.00	5.00	0.0011 ± 0.0002	0.008 ± 0.002	0.012 ± 0.003
		5.00	6.50	0.00010 ± 0.00004	0.001 ± 0.001	0.001 ± 0.001

				Be5	MB50	MB100
θ_{min} (mrad)	θ_{max} (mrad)	p_{min} (GeV/c)	p_{max} (GeV/c)	$d^2N^{\pi^-}/(dpd\Omega)$ 1/(GeV/c sr)	$d^2N^{\pi^-}/(dpd\Omega)$ 1/(GeV/c sr)	$d^2N^{\pi^-}/(dpd\Omega)$ 1/(GeV/c sr)
150	180	0.75	1.00	0.039 ± 0.007	0.305 ± 0.054	0.458 ± 0.086
		1.00	1.25	0.033 ± 0.005	0.295 ± 0.046	0.400 ± 0.059
		1.25	1.50	0.029 ± 0.004	0.210 ± 0.029	0.280 ± 0.040
		1.50	1.75	0.022 ± 0.003	0.154 ± 0.021	0.232 ± 0.031
		1.75	2.00	0.016 ± 0.002	0.111 ± 0.017	0.210 ± 0.034
		2.00	2.25	0.012 ± 0.002	0.094 ± 0.014	0.164 ± 0.023
		2.25	2.50	0.009 ± 0.002	0.065 ± 0.011	0.096 ± 0.016
		2.50	2.75	0.006 ± 0.001	0.044 ± 0.008	0.073 ± 0.013
		2.75	3.00	0.005 ± 0.001	0.035 ± 0.006	0.057 ± 0.011
		3.00	3.25	0.003 ± 0.001	0.022 ± 0.005	0.033 ± 0.007
		3.25	4.00	0.0019 ± 0.0004	0.013 ± 0.003	0.019 ± 0.004
		4.00	5.00	0.0004 ± 0.0001	0.003 ± 0.001	0.005 ± 0.002
		5.00	6.50	0.00003 ± 0.00001	0.000 ± 0.001	0.001 ± 0.001
180	210	0.75	1.00	0.037 ± 0.007	0.250 ± 0.046	0.351 ± 0.067
		1.00	1.25	0.031 ± 0.005	0.191 ± 0.029	0.309 ± 0.049
		1.25	1.50	0.022 ± 0.004	0.155 ± 0.025	0.253 ± 0.039
		1.50	1.75	0.018 ± 0.003	0.121 ± 0.019	0.189 ± 0.028
		1.75	2.00	0.014 ± 0.002	0.090 ± 0.016	0.136 ± 0.022
		2.00	2.25	0.011 ± 0.002	0.065 ± 0.011	0.087 ± 0.015
		2.25	2.50	0.007 ± 0.001	0.051 ± 0.010	0.075 ± 0.013
		2.50	2.75	0.005 ± 0.001	0.030 ± 0.006	0.054 ± 0.009
		2.75	3.00	0.003 ± 0.001	0.018 ± 0.004	0.033 ± 0.007
		3.00	3.25	0.0018 ± 0.0004	0.010 ± 0.003	0.016 ± 0.005
		3.25	4.00	0.0008 ± 0.0002	0.007 ± 0.002	0.008 ± 0.003
		4.00	5.00	0.00014 ± 0.00006	0.003 ± 0.001	0.003 ± 0.001
		5.00	6.50	0.00001 ± 0.00001	0.001 ± 0.001	0.000 ± 0.001

Appendix D

Proton-beryllium interaction length

In this appendix we describe the measurement of p-Be interaction length, λ_I , by reconstructing the interaction vertices in 40.0 cm long target data.
We use short target data vertex distribution to obtain interaction vertex resolution for our analysis. In the first step of this process, we fit the function in Eq. (D.1) to the Be5 short target vertex distribution as shown in Fig. D.1.

$$F_{Be5}(z) = p_0 + \frac{p_1}{(z - p_2)^2 + p_3}. \tag{D.1}$$

The theoretical vertex distribution for 40.0 cm long target is obtained by convolving Eq. (D.1) with a 40 cm long target as defined in equation (D.2). The convolution integral depends on starting position of the target and the interaction length of the material. The starting position of the target is varying from -200 mm to -150 mm with step size of 2 mm, and the interaction length parameter is varying from 300 mm to 600 mm with step size of 10.0 mm.

$$P(z) = \sum_{z_{tar}} F_{Be5}(z - z_{tar}) \cdot e^{-z_{tar}/\lambda_I} \cdot \delta z_{tar}, \tag{D.2}$$

where z_{tar} is the coordinate of the target position along z-axis and δz_{tar} is the bin width of that vertex coordinate. Next the convolution integral distribution is compared

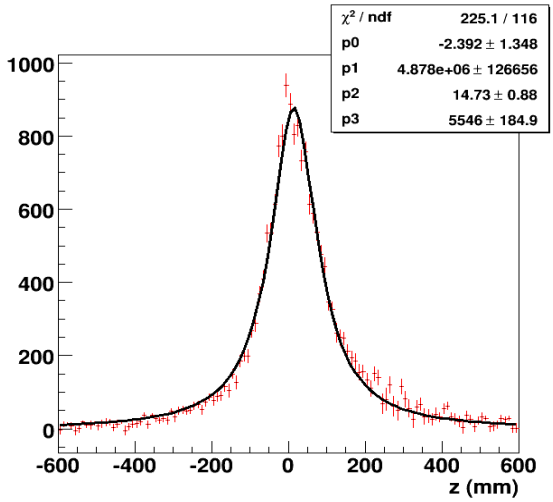

Figure D.1: The fitted curve (Solid-black) on the interaction vertex distribution of Be5 short target data.

with the reconstructed real interaction length distribution. The parameters z_in and λ_I are obtained by minimizing a 2D χ^2 distribution (D.3)

$$\chi^2(z_{in}, \lambda_I) = \sum_j \frac{(DATA(z_j) - P(z_j, \lambda_I, z_{in}))^2}{\sigma_j^2(\text{DATA})}. \tag{D.3}$$

We find the minimum by fitting the χ^2 distribution to a parabolic curve (D.4).

$$F(z_{in}, \lambda_I) = p_0 + p_1 \cdot (z_{in} - p_2)^2 + p_3 \cdot (\lambda_I - p_4)^2 + p_5 \cdot (z_{in} - p_2) \cdot (\lambda_I - p_4). \tag{D.4}$$

Where $p_0 - p_5$ are the fitting parameters. Figure D.2 (a) shows the contour plot of 2D χ^2 distribution which is nearly parabolic and the figure D.2 (b) shows the the parabolic function which fitted with the 2D χ^2 distribution to estimate the minimum point. The values of the best fitted parameters are presented in the Table.D.1. The estimated p-Be interaction length from the 40.0 cm beryllium target data is 454^{+14}_{-9} mm as compared to PDG value of 407 mm.

The best estimated initial position of the target is $-169.0^{+0.6}_{-1.0}$ mm. The convolution integral distribution for these λ_I and z_{in} is plotted in Fig. D.3 with the MB100 real data distribution. While the fitted value of λ_I is higher than what we expected,

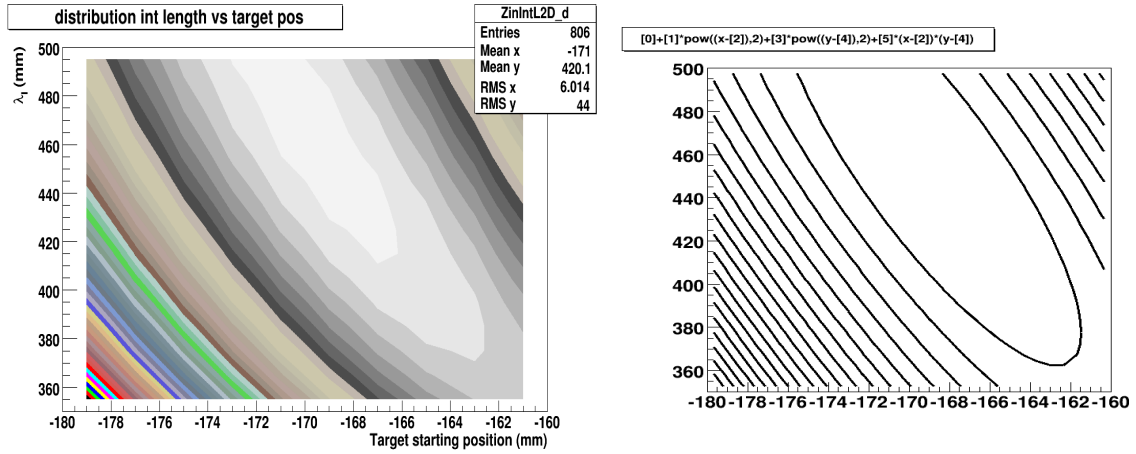

(a) (b)

Figure D.2: (a) χ^2 distribution of matching convolution plot with MB100 data distribution in the variable space of λ_I and z_{in}. (b) Best fitted parabolic function of χ^2 space.

theses parameters give a good fit to the data. Our analysis does not correct for tertiary interactions in the target and this may be the reason for the longer measured interaction length.

Parameter	value	parabolic error	MINOS error (-ve)	MINOS error (+ve)
p_0	$2.069e{+}02$	$2.228e{+}00$	$-2.238e{+}00$	$2.236e{+}00$
p_1	$1.397e{+}00$	$4.776e{-}02$	$-4.815e{-}02$	$4.815e{-}02$
p_2	$-1.690e{+}02$	$6.466e{-}01$	$-1.007e{+}00$	$6.326e{-}01$
p_3	$9.313e{-}03$	$7.031e{-}04$	$-8.217e{-}04$	$8.202e{-}04$
p_4	$4.544e{+}02$	$8.947e{+}00$	$-8.604e{+}00$	$1.419e{+}01$
p_5	$1.916e{-}01$	$5.771e{-}03$	$-5.893e{-}03$	$5.896e{-}03$

Table D.1: List of the best fitted parameter values of parabolic fitting function (D.4). Since the MINOS errors [75] are calculated by taking account the parameter correlations in the minimization process, we use MINOS errors to estimate the uncertainties of best fitted parameters.

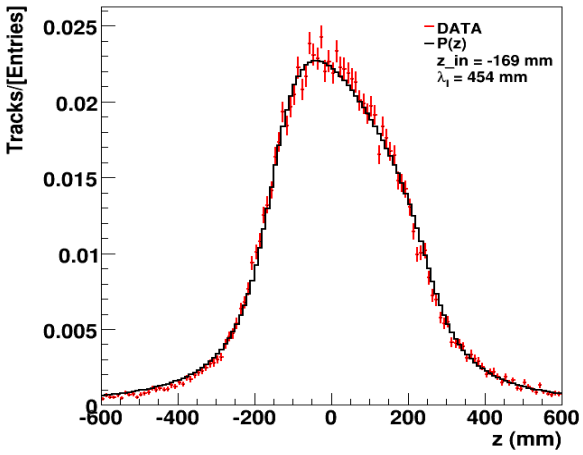

Figure D.3: The interaction vertex distribution (red-dotted) of MB100 data and the convolution integral plot (solid-black) for $\lambda_I = 454$ mm and $z_{in} = -169.0$ mm.

Bibliography

[1] W. Pauli. Dear radioactive ladies and gentlemen. *Phys.Today*, 31N9:27, 1978.

[2] H. Bethe and R. Peierls. The 'neutrino'. *Nature*, 133:532, 1934.

[3] S.H. Neddermeyer and C.D. Anderson. Note on the Nature of Cosmic Ray Particles. *Phys.Rev.*, 51:884–886, 1937.

[4] C.L. Cowan, F. Reines, F.B. Harrison, H.W. Kruse, and A.D. McGuire. Detection of the free neutrino: A Confirmation. *Science*, 124:103–104, 1956.

[5] B. Pontecorvo. *Sov. Phys. JETP*, 6:429, 1957. [Zh. Eksp. Teor. Fiz. 33, 549 (1957)].

[6] C. S. Wu, E. Ambler, R. W. Hayward, D. D. Hoppes, and R. P. Hudson. *Phys. Rev.*, 105:1413–1415, Feb 1957.

[7] G. Danby, J.M. Gaillard, Konstantin A. Goulianos, L.M. Lederman, Nari B. Mistry, et al. Observation of High-Energy Neutrino Reactions and the Existence of Two Kinds of Neutrinos. *Phys.Rev.Lett.*, 9:36–44, 1962.

[8] Z. Maki, M. Nakagawa, and S. Sakata. *Prog. Theor. Phys.*, 28:870, 1962.

[9] Jr. Davis, Raymond. Attempt to detect the antineutrinos from a nuclear reactor by the Cl37(anti-nu,e-) A37 reaction. *Phys.Rev.*, 97:766–769, 1955.

[10] John N. Bahcall. *Phys. Rev. Lett.*, 12:300–302, Mar 1964.

[11] Martin L. Perl. Evidence for, and Properties of, the New Charged Heavy Lepton. 1977.

[12] K. Kodama et al. Observation of tau neutrino interactions. *Phys.Lett.*, B504:218–224, 2001.

[13] L. Wolfenstein. Neutrino Oscillations in Matter. *Phys.Rev.*, D17:2369–2374, 1978.

[14] S.P. Mikheev and A. Yu. Smirnov. Resonance Amplification of Oscillations in Matter and Spectroscopy of Solar Neutrinos. *Sov.J.Nucl.Phys.*, 42:913–917, 1985.

[15] Simon Peter Rosen and James M. Gelb. Mikheev-Smirnov-Wolfenstein Enhancement of Oscillations as a Possible Solution to the Solar Neutrino Problem. *Phys.Rev.*, D34:969, 1986.

[16] Steven Weinberg. A Model of Leptons. *Phys.Rev.Lett.*, 19:1264–1266, 1967.

[17] S.L. Glashow. Partial Symmetries of Weak Interactions. *Nucl.Phys.*, 22:579–588, 1961.

[18] Abdus Salam. Weak and Electromagnetic Interactions. *Conf.Proc.*, C680519:367–377, 1968.

[19] Georges Aad et al. Observation of a new particle in the search for the Standard Model Higgs boson with the ATLAS detector at the LHC. *Phys.Lett.*, B716:1–29, 2012.

[20] Serguei Chatrchyan et al. Measurement of the properties of a Higgs boson in the four-lepton final state. *Phys.Rev.*, D89(9):092007, 2014.

[21] S. Chatrchyan et al. The CMS experiment at the CERN LHC. *JINST*, 3:S08004, 2008.

[22] Michael Andrew Parker. The ATLAS detector for the LHC. *AIP Conf.Proc.*, 272:1837–1841, 1992.

[23] R.P. Feynman and Murray Gell-Mann. Theory of Fermi interaction. *Phys.Rev.*, 109:193–198, 1958.

[24] E.C.G. Sudarshan and R.e. Marshak. Chirality invariance and the universal Fermi interaction. *Phys.Rev.*, 109:1860–1860, 1958.

[25] J.J. Sakurai. MASS REVERSAL AND WEAK INTERACTIONS. *Nuovo Cim.*, 7:649–660, 1958.

[26] Nicola Cabibbo. Unitary symmetry and leptonic decays. *Phys. Rev. Lett.*, 10:531–533, Jun 1963.

[27] K.S. Hirata et al. Experimental Study of the Atmospheric Neutrino Flux. *Phys.Lett.*, B205:416, 1988.

[28] Y. Totsuka. *Conf.Proc.*, C860416:118, 1986.

[29] J.N. Abdurashitov et al. Solar neutrino flux measurements by the Soviet-American Gallium Experiment (SAGE) for half the 22 year solar cycle. *J.Exp.Theor.Phys.*, 95:181–193, 2002.

[30] J.N. Abdurashitov et al. Measurement of the solar neutrino capture rate with gallium metal. III: Results for the 2002–2007 data-taking period. *Phys.Rev.*, C80:015807, 2009.

[31] W. Hampel et al. GALLEX solar neutrino observations: Results for GALLEX IV. *Phys.Lett.*, B447:127–133, 1999.

[32] T.A. Kirsten. GALLEX solar neutrino results and status of GNO. *Nucl.Phys.Proc.Suppl.*, 77:26–34, 1999.

[33] J. Boger et al. The Sudbury neutrino observatory. *Nucl.Instrum.Meth.*, A449:172–207, 2000.

[34] Y. Fukuda et al. *Phys.Rev.Lett.*, 81:1562–1567, 1998.

[35] K. Abe et al. Evidence for the Appearance of Atmospheric Tau Neutrinos in Super-Kamiokande. *Phys.Rev.Lett.*, 110(18):181802, 2013.

[36] J. Breault, D. Kielczewska, M. Goldhaber, S.T. Dye, C.B. Bratton, et al. THE IRVINE-MICHIGAN-BROOKHAVEN EXPERIMENT.

[37] P. Adamson et al. Combined analysis of ν_μ disappearance and $\nu_\mu \to \nu_e$ appearance in MINOS using accelerator and atmospheric neutrinos. *Phys.Rev.Lett.*, 112:191801, 2014.

[38] Marat Khabibullin. Latest oscillation results from T2K. 2011.

[39] Alexander Izmaylov. New Oscillation Results from the T2K experiment. pages 154–158, 2013.

[40] M.H. Ahn et al. Measurement of Neutrino Oscillation by the K2K Experiment. *Phys.Rev.*, D74:072003, 2006.

[41] F. Capozzi, L. Fogli, G. E. Lisi, A. Marrone, D. Montanino, and A. Palazzo. Status of three-neutrino oscillation parameters, circa 2013. *Phys. Rev. D*, 89:093018, May 2014.

[42] M.C. Gonzalez-Garcia, Michele Maltoni, Jordi Salvado, and Thomas Schwetz. Global fit to three neutrino mixing: critical look at present precision. *JHEP*, 1212:123, 2012.

[43] F.P. An et al. Spectral measurement of electron antineutrino oscillation amplitude and frequency at Daya Bay. *Phys.Rev.Lett.*, 112:061801, 2014.

[44] Seon-Hee Seo. New Results from RENO. *PoS*, Neutel2013:018, 2014.

[45] P. Adamson et al. Measurement of Neutrino and Antineutrino Oscillations Using Beam and Atmospheric Data in MINOS. *Phys.Rev.Lett.*, 110(25):251801, 2013.

[46] P. Adamson et al. Electron neutrino and antineutrino appearance in the full MINOS data sample. *Phys.Rev.Lett.*, 110(17):171801, 2013.

[47] K. Abe et al. Observation of Electron Neutrino Appearance in a Muon Neutrino Beam. *Phys.Rev.Lett.*, 112:061802, 2014.

[48] K. Abe et al. Measurement of Neutrino Oscillation Parameters from Muon Neutrino Disappearance with an Off-axis Beam. *Phys.Rev.Lett.*, 111(21):211803, 2013.

[49] A Aguilar, LB Auerbach, RL Burman, DO Caldwell, ED Church, AK Cochran, JB Donahue, A Fazely, GT Garvey, RM Gunasingha, et al. Evidence for neutrino oscillations from the observation of ν^- e appearance in a ν^- μ beam. *Physical Review D*, 64(11):112007, 2001.

[50] A.A. Aguilar-Arevalo et al. The Neutrino Flux prediction at MiniBooNE. *Phys.Rev.*, D79:072002, 2009.

[51] Michel Sorel. *Search for Sterile Neutrinos Using the MiniBooNE Beam.* PhD thesis, 2005.

[52] A.A. Aguilar-Arevalo et al. The MiniBooNE Detector. *Nucl.Instrum.Meth.*, A599:28–46, 2009.

[53] S. Agostinelli et al. GEANT4: A Simulation toolkit. *Nucl.Instrum.Meth.*, A506:250–303, 2003.

[54] Status report of the HARP experiment July 2004. 2004.

[55] I. Chemakin et al. Pion production by protons on a thin beryllium target at 6.4-Ge, 12.3-GeV/c, and 17.5-GeV/c incident proton momenta. *Phys.Rev.*, C77:015209, 2008.

[56] F. Abe, K. Hara, S. Kim, K. Kondo, S. Miyashita, et al. Production of Neutral Strange Particles K^0_S and Λ^0 by 12 GeV Protons on Nuclear Targets. *Phys.Rev.*, D36:1302–1319, 1987.

[57] Nikolai V. Mokhov. The MARS code system user's guide version 13(95). 1995.

[58] N.V. Mokhov and S.I. Striganov. MARS15 overview. *AIP Conf.Proc.*, 896:50–60, 2007.

[59] David W. Schmitz. *"A measurement of hadron production cross sections for the simulation of accelerator neutrino beams and a search for ν_μ to ν_e oscillations in the δm^2 about equals $1eV^2$ region"*. PhD thesis, 2008.

[60] Ryan Benton Patterson. A search for muon neutrino to electron neutrino oscillations at $\delta(m^2) > 0.1$ eV^2. 2007.

[61] M.G. Catanesi, M.T. Muciaccia, E. Radicioni, P. Righini, S. Simone, et al. "Proposal to study hadron production for the neutrino factory and for the atmospheric neutrino flux". 1999.

[62] E. Aliu et al. "Evidence for muon neutrino oscillation in an accelerator-based experiment". *Phys.Rev.Lett.*, 94:081802, 2005.

[63] A.A. Aguilar-Arevalo et al. "Bringing the SciBar detector to the booster neutrino beam". 2006.

[64] A.A. Aguilar-Arevalo et al. "A Search for electron neutrino appearance at the $\Delta m^2 \sim 1$eV^2 scale". *Phys.Rev.Lett.*, 98:231801, 2007.

[65] A. Bagulya, A. Blondel, S. Borghi, G. Catanesi, P. Chimenti, et al. Dynamic Distortions in the HARP TPC: Observations, measurements, modelling and corrections. *JINST*, 4:P11014, 2009.

[66] M. Anfreville, P. Astier, M. Authier, A. Baldisseri, M. Banner, et al. The Drift chambers of the NOMAD experiment. *Nucl.Instrum.Meth.*, A481:339–364, 2002.

[67] M.G. Catanesi et al. The HARP detector at the CERN PS. *Nucl.Instrum.Meth.*, A571:527–561, 2007.

[68] J. J. Gomez-Cadenas A. Cervera-Villanueva and J. A. Hernando. "RecPack, a general reconstruction toolkit". *Nucl. Instrum. Meth*, A 534, 2004.

[69] P. Billoir. "Track Fitting With Multiple Scattering: A New Method". *Nucl. Instrum. Meth*, A 225(352), 1984.

[70] M. Baldo-Ceolin, G. Barichello, F. Bobisut, M. Bonesini, A. De Min, et al. The time-of-flight TOFW detector of the HARP experiment: Construction and performance. *Nucl.Instrum.Meth.*, A532:548–561, 2004.

[71] M.G. Catanesi, E. Radicioni, R. Edgecock, Malcolm Ellis, S. Robbins, et al. "Particle identification algorithms for the HARP forward spectrometer". *Nucl.Instrum.Meth.*, A572:899–921, 2007.

[72] M.G. Catanesi et al. "Measurement of the production cross-section of positive pions in p-Al collisions at 12.9-GeV/c". *Nucl.Phys.*, B732:1–45, 2006.

[73] M. G. Catanesi et al. "Measurement of the production cross-section of positive pions in the collision of 8.9 GeV/c protons on beryllium". *Eur.Phys.J.C*, C52:29–53, 2007.

[74] MiniBooNE Collaboration. First measurement of the muon neutrino charged current quasielastic double differential cross section. *Phys.Rev.D81:092005,2010*, 2010.

[75] Fred James and Matthias Winkler. MINUIT User's Guide. 2004.